Shear-induced segregation in dense granular mixtures

A DISSERTATION
SUBMITTED TO THE FACULTY OF THE GRADUATE SCHOOL
OF THE UNIVERSITY OF MINNESOTA
BY

Yi Fan

IN PARTIAL FULFILLMENT OF THE REQUIREMENTS
FOR THE DEGREE OF
Doctor Of Philosophy

June, 2011

Acknowledgements

First and foremost, I am deeply indebted to my advisor Professor Kimberly Hill. She brought me into the field of granular materials, and taught me both the knowledge itself and the philosophy of how to conduct scientific research professionally and precisely. I appreciate all her contributions of time, ideas, and funding to make my Ph.D. experience productive and stimulating. Each time when I struggled in my research, her creative, constructive and invaluable guidance and ideas always encouraged and inspired me so much. All of these not only were critical for finishing my thesis and degree, but also are magnificently beneficial for my professional career as a researcher. Further, I would like to show my appreciation for Prof. Hill's invaluable support in all aspects of my life in Minnesota. I still remember and appreciate for her precious help as a kind friend, when I first came and settled down in Minnesota as a foreigner.

I am also grateful to my committee members: Prof. Lev Khazanovich, Prof. Vaughan Voller and Prof. James Kakalios for their time, interest, and helpful comments, which were very valuable for the completeness of my thesis. I would also like to thank the other member of my preliminary oral defense committee, Prof. Fernando Porte-Agel, for his time and insightful questions.

I would also like to thank the former and current fellow students in Prof. Hill's research group: Jiafeng Zhang, Bereket Tewoldebrhan, Kirby Templin, Greg Shaffer, John Gaffney, Leslie DellAngelo, Meghan Flanagen, Jeho Yoo, for their helpful discussions and suggestions for my research. I also would like to thank all staff in the St. Anthony Falls Laboratory, who provided a supportive research environment and excellent technical support.

I gratefully acknowledge the sources that funded me and my research during my graduate study in Minnesota. I was funded by the Sommerfeld Fellowship of University of Minnesota for my first year and National Science Foundation grants for my last four years. Also, I am grateful for the Sommerfeld Funds, the Anderson Award and Shaw-Lundquist Fellowship for providing supportive funds for research-related travel, materials and books.

Lastly, I would like to thank my family for all their love and encouragement: For my parents who raised me and supported me in all my pursuits; for my wife Guini and son Joechen whose infinite love and persistent confidence in me sustained me in the final stages of this thesis, and gave me the determination to finish it.

Abstract

Granular mixtures such as sand and powders tend to segregate or unmix by particle property. The details are important for many natural and industrial applications. While kinetic theory provides a mechanistic framework for modeling segregation in energetically agitated granular mixtures, there is no analogous framework for dense sheared granular mixtures. A number of segregation mechanisms have been identified as important, including those associated with pressure gradients, gravity, gradients in shear rates, and gradients in granular temperature - the kinetic energy of velocity fluctuations. All likely contribute to segregation in densely sheared systems, though there is no constitutive relationship for mixtures, and the details are difficult to determine. Further, in typical experimental systems designed to study segregation in dense granular flow (such as chutes and rotated drums), gravity, velocity gradients, and porosity gradients coexist in the direction of segregation.

The research in this thesis uses physical and computational experiments to elucidate particular segregation mechanisms in dense granular flow and develop a theoretical model incorporating these segregation mechanisms. Experiments are conducted in a relatively new geometric configuration called split-bottom cell which can isolate shear rate and porosity gradients from gravity. Distinct Element Method (DEM) simulations of experiments in this geometry and in a chute flow provide details inaccessible experimentally including particle concentrations and velocities at every point in space and interparticle forces. These simulations reveal unique dynamics associated with shear-induced segregation in dense systems. Based on the results, a theoretical framework is developed to model segregation associated with shear gradients in dense sheared granular mixtures.

Contents

List of Tables

List of Figures

Chapter 1

Introduction

Granular materials – configurations of particles in sufficient quantities to behave in a continuum-like fashion – are ubiquitous in our daily life. As mentioned by de Gennes [1], if measured by weight, granular materials are the second-most-manipulated media by man, just behind water. As simple as they appear upon first consideration, they exhibit a complex behavior that is hard to predict. For example, mixtures of macroscopic particles tend to unmix by particle property. One of the most dramatically destructive examples of this occurs in debris flow: Boulders, rocks, and sand tumble down a hillside, and the largest rocks migrate toward the top and then the front of the flow where they do the most damage. This thesis is concerned with segregation in dense sheared systems such as bouldery debris flows. To provide the framework for the research presented, first, some general background on granular materials is discussed. Then, some background particular to segregation in granular materials is reviewed.

A better understanding of the physics of granular materials not only can help us to understand certain related natural phenomena including those that can be quite destructive. For example, mud flow, debris flow, and pyroclastic flow are granular-fluid flows which can damage houses, roads, and bridges, and are responsible for the deaths of thousands of people each year in the world. China has the largest numbers of deaths and economic loss due to landslides occurrence in the world, because of its large population, complex geological structure and low forest coverage. It was estimated that more than 1,300 people were killed or missing due to landslide caused debris flow or mud flow in

2010[1] . To reduce these numbers, a better understanding of the dynamics of granular materials related to natural disasters is sorely needed.

Granular materials are also important in many industrial applications. Examples include pharmaceutical and chemical industries that rely on the processing of powders or pills and agricultural industries where seeds, grains, and granular foodstuffs are transported and manipulated. However, due to our poor handling and processing of granular matter, it is estimated that we waste 40% of the capacity of many of our industrial plants (See Refs. [2] [3]).

Our understanding of granular materials is still far from perfect mainly due to their unique and complex characteristics. If one only considers the interaction between two particles, the physics of granular materials seems simple, but granular materials actually behave differently from any of the common forms of matter: solid, liquid, or gas. One of the most important aspects that make granular materials different from other matter is that the effect of ordinary temperature T on dynamics of granular materials is negligible. As pointed out by Jaeger et al. [4], the potential energy of a typical sand is at least 10^{12} times $k_B T$ at room temperature, thus thermal energy is insufficient to move particles. The energy scale $k_B T$ used to search phase space in classical thermodynamics to develop a framework for modeling conventional materials is not appropriate for granular materials. Granular systems exhibit multiple metastable steady states which are far from equilibrium. Without energy from external agitations such as shearing or vibrations, each metastable configuration will last indefinitely.

The dynamic behaviors of granular materials are strongly influenced by external excitations and boundary conditions and there is no single general model for all behaviors of granular materials. Instead, depending on the amount of energy input and constraints from the boundaries, the flow of granular materials is typically classified into one of three regimes and its behavior is modeled according to the regime. These are the 'solid-like' quasi static regime, 'liquid-like' dense regime and 'gas-like' sparse and energetic regime. The behaviors of granular flows are dramatically different in these three regimes. A detailed description of three phases of granular flow will be presented in next section.

---

[1] www.mapreport.com

1.1 Three phases of granular materials

When granular materials flow down an inclined plane, particles in different regions exhibit different behaviors. In the bottom layers, the particles do not move or creep very slightly; in a few layers at surface, the particles flow energetically and bounce in all directions like a gas; between these two regions, particles flow continuously and densely like a liquid. These three regions of flow represent three phases of granular materials: the solid-like quasi static regime, the gas-like sparse and energetic regime and the intermediate liquid-like dense flow regime. The microscopic and macroscopic properties of these three regimes are greatly different so that different theories have been developed in each regime.

1.1.1 Solid-like regime

In the 'solid-like' regime, granular materials are densely packed and particles interact mainly via enduring frictional contacts, so the granular materials in a static state can support large loads of buildings, pavement and roads. Inertial effects are typically negligible. Slow creeping motion typical of this state is modeled effectively by plasticity theory in soil mechanics based on Mohr-Coulomb yield criterion [5][6][7]. This is far from focus of this thesis and would not be discussed further here.

1.1.2 Gas-like regime

In the gas-like regime of granular materials where the flow is energetic and sparse, particles interact generally by binary and near-instantaneous collisions. Though in some ways these granular materials resemble a gas, there is a major difference between the conventional gas and granular gas. The collisions between granular particles are inelastic, while the collisions between molecules of gas are generally elastic so that energy will be dissipated during particle collisions in the granular gas. This nature of energy dissipation of granular gas causes a variety of distinct flow behaviors and patterns such as density waves and clustering. A density wave is where granular particles do not flow uniformly, but instead flow with regions of high density traveling with different velocity from that of the average velocity [8] [9] [10]. Clustering occurs as granular gas "cools", that is loses energy through collisions. Specifically, as particles in a granular gas slow to a stop, they do so non-uniformly in clusters [11].

The first efforts for modeling granular gases involved considerations of the granular behavior as a continuum. Bagnold [12] first proposed a simple heuristic model to relate the constitutive behavior to the microscopic properties. Considering momentum transfer associated with interparticle collisions, Bagnold found the normal stress is proportional to the product of the shear rate and the particle diameter squared. He also showed the shear stress should be proportional to normal stress. These results showed very good agreement with experimental results [12].

Later, additional efforts were made to develop more detailed constitutive relations based on more sophisticated statistical arguments regarding collisional frequencies and the particle interactions. These include the efforts of Savage and Jeffrey[13], Ackermann and Shen [14], Jenkins and Savage [15], Lun et al. [16] and others (More references can be found in the review article of Campbell [17]). Many of these efforts have focused on adapting the kinetic theory of dense gases to granular gases. The assumptions of kinetic theory of granular gas include: (1) Particles interact by instantaneous and binary collisions; (2) Molecular chaos applies, which means velocities of colliding particles are uncorrelated, and independent of their position; (3) Energy is dissipated by collisions. Typically, surface friction or any other particle interactions tangential to the point of contact are ignored [17]. Based on a general distribution function for all particles, the flow properties of the mean fields (e.g., average velocity, the local solids volume fraction, the velocity fluctuations correlations) can be defined statistically. The governing equations are established based on Maxwell transport equations, where the mass, linear momentum and angular momentum are conserved. In addition, instead of using thermal temperature related to the velocities of molecules, a granular temperature, defined as the kinetic energy of velocity fluctuations is used in the energy equations (See the review article of [17] and references therein). More recently, Jenkins and Mancini [18, 19] and others have further expanded kinetic theory to mixtures of different types of particles in a granular gas with a particular focus on their segregation characteristics. More details will be discussed in section 1.2.

1.1.3 Liquid-like regime

The intermediate regime between the gas-like and solid-like regime is the liquid-like regime, also called the dense flow regime, where interactions between particles are multiple and enduring. In this regime, inertial effects cannot be neglected, and collisonal forces are important so that plasticity theory for quasi-static regime is not applicable. On the other hand, in contrast with the dilute regime, collisions are highly correlated, and the collisions are neither binary nor instantaneous. All of these features do not satisfy some of the assumptions on which current formulations of kinetic theory for granular gas are developed. In lieu of this, because of the liquid-like features in the dense regime, there have been efforts to develop a hydrodynamic model [20]. As in the Navier-Stokes equation for fluids, the focus here is on a constitutive law between internal stresses and strain rate.

To build a rheological constitutive model based on macroscopic considerations, the visco-plastic features of the granular liquid need to be included. That is, there is a stress, below which the granular material does not flow, and once the particles start to flow, the stresses are shear-rate dependent. There are several constitutive laws based on these considerations that have been proposed. For example, Mohan et al. [21] developed a modified Cosserat approach based on plasticity theory by adding an additional degree of freedom through local rotation. Kamrin and Bazant [22] proposed another model inspired by Mohr-Coulomb plasticity by introducing a stochastic flow rule in a Coulomb material.

Other treatments include considerations of the multiphase nature of granular fluids. Aranson and Tsimring [23] introduced a model by treating granular media as a mixture of solid and liquid phases, whose relative fraction is controlled by a Landau equation. Modifications have included decomposition of the stress tensor into a collision term and a friction term [24]. Some efforts were also made to modify the kinetic theory by reformulating the constitutive relation or accounting for enduring interparticle contacts. Transport coefficients in kinetic theory have been modified by revising viscosity terms [25], dissipation terms [26], length scales [27] [28] , and collision frequency [29].

Recently, a new type of constitutive law was proposed which appears to reproduce a wide range of visco-plastic behaviors of the dense flow. In this model, a parameter called inertia number I, first proposed by da Cruz et al. [30], is defined by:

$$I = \frac{\dot{\gamma} d}{\sqrt{P/\rho_p}} \tag{1.1}$$

where, $\dot{\gamma}$ is shear rate, P is pressure, d is particle diameter and ρ_p is particle material density. The inertia number is the square root of Savage number and Coulomb number [30, 31, 32] and presents a ratio of macroscopic time scale $1/\dot{\gamma}$ and microscopic time scale $d/\sqrt{P/\rho_p}$. Small values of I correspond to the quasi-static regime in the sense that macroscopic deformation is slow compared to microscopic rearrangement, whereas large values of I correspond to rapid flows. The associate constitutive relationship in 2D is simply

$$\tau = P\mu(I) \quad \text{and} \quad f = f(I) \tag{1.2}$$

Here, τ is shear stress, μ is friction coefficient and f is solids fraction. Both μ and f are dependent on inertia number I. Different formulations of friction law $\mu(I)$ and dilatancy law $f(I)$ were proposed such as a linear relation by da Cruz et al. [30], a power law relation by Hatano [33], and a more complicated relation by Refs. [34] [35]:

$$\mu(I) = \mu_1 + (\mu_2 - \mu_1)/(I_0/I + 1) \quad \text{and} \quad f(I) = f_{\max} + (f_{\min} - f_{\max})I \tag{1.3}$$

Here, μ_1, μ_2, $f_{\max}$, $f_{\min}$ and I_0 are fitting parameters. These models generally can well predict the rheology in most of simple systems such simple shear flow and chute flow in a wide range of I and even in 3D [20] provided the coefficients μ_1, μ_2, $f_{\max}$, $f_{\min}$ and I_0 can be determined somehow. This is generally done empirically. Based on these models, the rheological models for mixtures with different size were also being developed such as [36, 37, 38], where they tried to replace the diameter d in Equation (1.1) by a local average $\overline{d}$ in the constitutive law. However, all of these constitutive models are not perfect. Most of these can predict the rheology of flow within certain systems and boundary conditions. Even for the models by Pouliquen and colleagues [34, 35, 20], which seem to be successfully applied in many systems, still have certain limitations in transition to the quasi-static [39] or rapid flow limits [40].

1.1.4 Transitions: from solid to liquid to gas

So far, there are still no simple order parameters for the boundaries between the liquid-solid or liquid-gas phases of granular materials. From the solid-like regime to liquid-like regime, the friction coefficient of granular materials can be used as a first-order parameter to describe the transition. However, there are some limitations for friction criterion. First, the initiation of the flow is sensitive to history of preparation of granular materials (e.g. Ref. [41]). Second, it cannot describe the hysteresis problem, which is due to different values of static friction coefficient and dynamic friction coefficient (e.g. Ref. [42]). Last, the system sizes also influence the flow threshold (e.g. Ref. [43]). From the liquid-like regime to gas-like regime, there is no such parameter as friction coefficient yet.

Instead, some researchers have used computational simulations to understand the transitions in the microscopic scales such as the duration of contact [44], or the correlation of force networks [45]. Another series of works attempted to determine transitions among all three different phases as a whole picture such as Babic et al. [46], Campbell [47], Ji and Shen [48], who used both macro parameters (such as relation of stresses and shear rate) and micro parameters (such as contact time duration, coordination numbers etc.) in 2D and 3D systems to determine the boundaries of the different phases. They found that the system solids fraction, the shear rate, and the particle stiffness can all influence the phase transitions.

To summarize, there exists a general theoretical model that can well predict the dynamics and kinematics of the flow in the quasi-static regime or sparse and energetic regime, but in the dense flow regime, although great progress has been made in recent years to build a constitutive law, a general theoretical framework is still lacking. Therefore, it is still impossible to accurately predict dynamic and kinematic properties in dense flow regime from the first principles, particularly for the mixtures. The focus of this research is on the dense flow regime, which is far from quasi-static regime or sparse and energetic regime, so that the transitions between these regimes are not of concern. Instead, this research is concerned with inherent segregation of granular mixtures in dense flow regime, which widely exists in the nature and industries. The goal is to elucidate particular segregation mechanisms in dense flow, which not only can help improve the understanding of segregation in dense flow, but also may facilitate the development of the constitutive law for mixtures in the dense flow. In the next section, segregation mechanisms will be reviewed.

1.2 Segregation mechanisms

Mixtures of granular materials with different size, density or other material properties tend to segregate or de-mix when agitated by external excitations such as vibrations or shearing. This gives rise to a number of interesting pattern formation problems in nature and challenges for many industries. In most cases, the segregation is unwanted and even destructive. For example, in nature, the segregation of large boulders and rocks to the front of debris flow increases damage [49, 50, 51]. In pharmaceutical industries, segregation of powders will inhibit mixing of different components of pharmaceutical powders and consequently cause inconsistent delivery of medication [52]. In this section, the mechanisms for different segregation patterns will be discussed for two different types of systems characterized by the way the granular materials are agitated: vibrated systems and sheared systems. While this thesis is primarily focused on segregation in densely sheared flows, there has been more progress in vibrated systems. Therefore, this is reviewed in detail here.

1.2.1 Segregation in vibrated granular flow

When one shakes a box of cereals or beans vertically for a certain period of time, the large cereals or beans typically accumulate on top of the container. This is usually called Brazil Nut Problem (BNP). In some situations, the large particles may also sink to the bottom of the container, which is called Reverse Brazil Nut Problem (RBNP). So far, great efforts have been made by researchers to study the mechanisms of BNP and RBNP experimentally and computationally in vibrated systems, and also a couple of theoretical approaches have been developed to model these mechanisms. In this section, different mechanisms to drive segregation in vertical vibrated system will be introduced. Interstitial fluids like air have been found to have strong effects on segregation, but this effect will be separately discussed and not be considered when discussing other mechanisms.

Void filling mechanism: The void filling mechanism for the BNP was identified by

Rosato et al. [53] using Monte Carlo simulations to simulate vertical shaken system without side walls (fulfilled by using periodic boundaries). They showed that important segregation events were associated with two phases of the shaking granular materials: expansion and condensation. During the upward motion of the container, the material is most compacted. During the downward drop of the motion, it is most diluted. They found during the expansion phases of shaking circle, all particles moved upward and many voids were generated, but during the compaction phases, the larger particles have a smaller probability to find a suitable void in the underlayers than small particles. This gives rise to an accumulation of small particles at the bottom of container, and large particles will move toward the surface relatively compared with small particles. When size ratio of large particle over small particles increases, the void filling mechanism will become stronger as shown in Vanel et al. [54] characterized by rise velocity of large particles. However, this void filling mechanism only works for a weak shaking, since the strong shaking will cause larger voids so that the probability to find a suitable void for large particles will be very close to that of small particles [55]. Besides, the strong excitations will cause a convection in the system, which will greatly effect the segregation mechanisms.

Convection mechanism: When the side walls with frictions exist and the shaking is strong enough, a convection roll can be induced in the vertically shaken granular materials. Though the convection was already mentioned in vibrated systems by other researchers such as Faraday back to 1831 [56], Knight et al. [57] experimentally showed the convection rolls alone can drive BNP. The mechanism for generating convection is that during the upward phase of shaking the mixture gets compacted and shear forces induced by the side walls extend through the whole sample. During the subsequent downward motion the mixture is more expanded and consequentially those particles adjacent to the walls experience stronger shear forces than those in the center of the container. Both phases combined give rise to a convection roll going downward at the sidewalls and upward in the center. When the convection rolls exist, during the expansion phase, both large and small particles move upward to surface, and then move outward to the side walls. However, those large particles, of which diameters are larger than the thickness of downward convection zones close to walls, are more likely trapped at surface, which eventually induces the size segregation. Further evidence for this mechanism was provided in the same research [57], where they made side walls outward slanting so that the convection roll reversed flow direction. In this case, they found that large particles were trapped in the middle close to the bottom plate, since these large particles cannot enter the thin upward flowing layers close to the side walls. However, it is worth noting that the convection does not always drive the segregation. Rosato et al. [58] showed that if the downward moving regions of convection rolls are big enough to accommodate large particles, these particles perform convective cycles, which can lead to mixing.

Inertia mechanism: During the discussion of previous two mechanisms, the effect of material density is not mentioned, which also can strongly influence the segregation behaviors. Shinbrot and Muzzio [59] found that heavy grains rise (BNP), but equally large, light grains sink in a granular bed (RBNP). They explained these phenomena by the inertia mechanism. That is the large intruder particle gains the inertia during the expansion phase, and during the compaction phase, heavier intruder particle with larger inertia can continue to lift off the bed to permit smaller particles in the bed infiltrate beneath. In contrast, the lighter intruder particle fluctuates wildly without enough inertia, preventing the infiltration [59]. Later, Molinari et al. [60] proposed a model based on energy considerations to explain the effect of inertia of the intruder particle on the BNP at strong excitations. However, in these research, only the motion of an intruder is investigated, and it is not clear whether it can be applied to a binary mixture.

Condensation mechanism: The condensation mechanism was proposed by Hong et al. [61], where they tried to evaluate how different combinations of size ratios and density ratios affect the segregation of binary mixtures in vibrated systems. They postulate the existence of a critical granular temperature T_C above which all particles are fluidized. For T smaller than T_C an increasing fraction of the particles should condense at the bottom of the container. This critical temperature T_C is proportional to mgd^3 based on energy conservation, where m is mass of individual particle, d is particle diameter. For binary mixture, the shaking will adjust system temperature to a value between critical temperature of two species, in which situation, one species will be fluidized and another will be condensed to bottom to cause segregation. However, the segregation due to condensation mechanism can only happen when the system temperature is between the critical values of two species. Otherwise, no segregation will happen due to condensation.

Thermal diffusion mechanism: The thermal diffusion mechanism is closely associated with kinetic theory of dilute granular flows. Jenkins and Mancini [18, 19] first expanded the kinetic theory to calculate the dynamic properties of granular mixtures in 2D system. After that, researchers developed this theoretical framework by using different single-particle velocity distribution (Non-Maxwellian, such as Huilin et al. [62] and Rahaman et al. [63]), different radial distribution function (revised Enskog theory, such as Arnarson and Willits [64], Willits and Arnarson [65], Hsiau and Hunt [66]) and also considering non-equipartition of granular temperature (such as Huilin et al. [62] and Rahaman et al.[63], Yoon and Jenkins [28] and Galvin et al. [67]).

Within the framework of kinetic theory for granular mixture, the segregation fluxes can be calculated by a diffusion equation, where diffusion forces include thermal diffusion forces, pressure diffusion forces and ordinary diffusion forces. All of these diffusion forces are dependent on the gradients of temperature and particle properties (See Refs. such as [28] [67],[68]). Refs. [69] and [70] investigated BNP and RBNP segregation using an intruder in a vibrated system and considering non-equipartition of granular temperature between different species. They found a control parameters ϕ which is the ratio of mean square velocities between intruder particle and matrix particles. For particles with same density, when ϕ is greater than 1, the BNP will be observed. ϕ will decrease when size ratio increases, which means if size ratio is large enough, the RBNP will occur.

Friction effect: The particle friction can directly or indirectly influence the segregation in the vibrated bed. Ciamarra et al.[71] used computational simulations to simulate segregation of mixtures with different coefficient of friction in a vertically vibrated bed and found that the particle with large friction coefficient will rise to surface. The friction of particles may also effect the segregation through influencing the flow dynamics, such as reported by Ulrich et al.[72].

Interstitial air effect: A direct study of the air effect on segregation was performed by Möbius et al. [73]. In their experiments a non-monotonic dependence of the rise time of a intruder was found as a function of the density ratio of the intruder to the surrounding particles with and without air : The rise time first increased as the density ratio was decreased; as density ratio was decreased further below 1, it was observed that the rise-time then decreased. However, both the magnitude and the location of the peak in the rise time were observed to decrease greatly without air in the container. In the reports of Yan et al.[74], a more detailed and complete examination of air effect was performed. They found that the intruder may rise up or sink, depending on the density ratio and size ratio of intruder to surrounding particles in the presence of interstitial air, but when air was evacuated, the intruder particle would always rise. They measured the pressure variation inside the container and found it decreased as a function of the depth inside the container, especially when the background particles were small. They concluded the RBNP was probably due to pressure gradient across the large intruder particle. In subsequent research of Möbius et al. [75], they more systematically studied the air effects on segregation in vibrated bed by varying size ratio, density ratio, intruder starting height, boundary conditions and air pressure. They observed both BNP and RBNP and developed a simple model that showed how the two regimes were connected by considering pressure gradients across the granular bed during a shaking cycle. Moreover, another research involving air effect was conducted by Burtally et al.[76]. They investigated segregation of mixtures differing density only in the vibrated system, where they found denser particles segregated to surface at lower shaking amplitudes, but denser particles segregated to middle region with less dense particle in the region of surface and bottom at higher shaking amplitudes. They proposed a model to examine air pressure gradient effect by analogizing the granular materials to the porous media and qualitatively explained the experimental observations. All in all, the interstitial air certainly has important effect on the segregation behaviors in the vibrated system.

Other possible mechanisms: The difference of coefficient of restitution of particles may also cause segregation as described by Serero et al.[70]. They predicted by kinetic theory that under a gradient of temperature, a mixture of particles only differing in restitution coefficient e will segregate, where particle with large e will segregate to cold region. Their simulation results agree well with this prediction. Shear-induced instability can also drive segregation in a horizontally vibrated system reported by Ciamarra et al. [77, 78]. They found a horizontal banding of different species in both experiments and simulations and they proposed that it is the shear-induced instability similar to the Kelvin-Helmholtz instability that gives rise to this horizontal segregation.

Until now, several mechanisms have been introduced for BNP and RBNP in the vibrated system, but in most cases, these mechanisms would not work independently.

For example, the void filling mechanism and the convection cell together can cause the BNP. The temperature gradient may also compete with the inertia effect. The kinetic theory is the most rigorous model to incorporate most of these effects from the first principle, but it generally only works in relatively dilute regime, and also the complicated transport equations make it very implicit to understand the direct relation between segregation behaviors and these driving mechanisms. A few researchers have attempted to create models which combine different mechanisms (e.g.[61][79][80]). However, they will not be discussed in detail here.

1.2.2 Segregation in sheared granular flow

In contrast with segregation associated with shaken systems, there has been much less work focused on segregation specific to sheared systems. Shear forces can be generated either by gravity or by moving boundaries. The former may include, for example, vertical chute flow, where the component of gravity parallel to the solid boundary shears the particles (such as [10, 81, 82]), or flow in the rotating drums (such as [83, 84]). A typical geometry for the sheared flow driven by mechanical energy is the annular shear cell, where the gravity is perpendicular to the shear direction in the experiments (such as [85, 86]). In computational simulations, an alternative is the plane shear cell, where two parallel side walls shear particles in opposite directions without the presence of gravity (such as [87, 88]).

As described in section 1.1, the flow characteristics and theoretical approach are greatly different in the dilute and dense regime, so there should also be different segregation behaviors and underlying mechanisms in these two regimes.

In the dilute regime, segregation in sheared flow is mostly studied by computational methods, since it is very difficult to generate a sheared flow at low solids fraction under gravity. Using a pseudo-2D system [87] or investigating the segregation phenomena near free surface in the physical experiments could be an option, but the boundary effect need to be evaluated. The most common geometry used to study the segregation of shear-driven flow is the plane shear cell. In this geometry, the moving side walls drive a gradient of granular temperature, which is higher close to the walls and lower in the center of the shear cell. During the simulations all particles migrate toward the center of cell, the region of lower temperature, and at the same time the heavier particles (larger if differing in size only or denser if differing density only) migrate faster to cause a species segregation pattern, where heavier particles have higher concentration in the lower temperature region. This segregation behavior is consistent for both binary mixture systems [67][87][89] and intruder particle systems [88].

Without gravity, gradients of granular temperature emerge as the primary driving factor based on calculations from kinetic theory [28][67][87][89]. As is the case for shaken systems, a diffusion equation is developed based on kinetic theory to predict the segregation velocity [28] [67][87]. There are three diffusion forces: thermal diffusion force, pressure diffusion force and ordinary diffusion force. The former two diffusion forces are driven by the gradients of temperature and differences in particle properties. The ordinary diffusion force depends on gradients of species' concentrations. An extra term in the diffusion equation could be added when there is an external force applied such as the gravity force. From the expressions for these diffusion forces, it is apparent that thermal diffusion forces will drive heavier particles to the regions of lower temperature, and ordinary diffusion forces will cause a remixing. The role of pressure diffusion forces is not explicit from the mathematical expression itself. From the simulation results of Refs. [67] [87], the pressure diffusion forces always acts in the direction to the thermal diffusion forces, which generally drive small particles to higher density regions [87].

All these diffusion forces compete with each other to determine segregation trends and segregation patterns in the final state. For example, in a sufficiently dilute regime, for density segregation (segregation associated with particles differing material density only), the thermal diffusion forces always dominate and denser particles segregate to regions of lower temperature; for size segregation (segregation associated with particles differing size only), the thermal diffusion forces also dominate and larger particles segregate to regions of lower temperature; for particles differing both size and density, it becomes more complicated, and segregation trends depend on both the density ratio and size ratio [87].

As the system solids fraction increases, the situation becomes more complicated as well. Conway et al. [87] found when their system solids fraction increases from 0.25 to 0.3, a reverse size segregation occurs, where large particles segregate to higher temperature regions. These phenomena motivate the following questions: Is there any size segregation in even denser systems driven by the gradients of granular temperature?

If so, is kinetic theory able to predict this trend?

Unfortunately some results showed that kinetic theory fails to predict segregation correctly in moderate dense regime (Such as Xu et al.[89], Montanero et al.[90]). This is likely because the assumptions and the methodologies in the kinetic theory approach do not match the intrinsic features of dense flow as described in section 1.1. In the dilute regime, the contacts between particles are dominated by collisions and particles also have enough space to fluctuate, so that granular temperature is fairly large and important. In the dense regime, frictional effects become more important.

Most research on segregation in dense flow has focused on the gravity effect (Such as Refs.[91][92][93][94][95]), and the effects of flow dynamics such as gradients of granular temperature or shear rate on segregation in dense regime are rarely explored. The most commonly used geometries to study gravity-induced segregation are rotating drums and chute flows in an inclined plane. In both systems, there is a flow layer near free surface with a thickness of around order of 10 particle diameters driven by gravity components along flow direction. Segregation primarily occurs in the direction perpendicular to flow direction. Generally speaking, for mixtures of particles differing in size only, small particles segregate along the direction of gravity components to sink at bottom of flowing layer and large particles rise to free surface. For mixtures of particles differing in material density only denser particles sink to the bottom of flowing layer and less dense particles rise to free surface. The segregation trends for the mixtures with different combinations of size and density ratios are more complicated, especially for the mixtures of larger but denser particles with smaller but less dense particles, which will be discussed at the end of this section.

The generally accepted mechanism for gravity-driven size segregation in densely sheared flow is, to some extent, similar to the void filling mechanism in the vibrated systems. Kinetic sieving (or percolation) [91, 92, 93, 96] is thought as the primary driving mechanism for size segregation. During shearing, particles with different size in one layer will have different probability of finding sufficient large voids in the layer beneath. The smaller particles have a high probability so that they can more easily move into these voids and subsequently sink under gravity. At the same time, the large particles will move opposite to gravity direction squeezed by small particles [91].

Savage and Lun [91] first proposed a model for kinetic sieving mechanism that involved a local distribution of voids. They incorporated this into a mass balance equation to predict segregation trends for particles flowing down an inclined plane. They obtained the following equations for segregation velocities:

$$q_{s,NET} = -D_l \frac{du}{dy} \phi_l (\tilde{q}_s - \tilde{q}_l) \tag{1.4a}$$

$$q_{l,NET} = D_l \frac{du}{dy} \phi_s (\tilde{q}_s - \tilde{q}_l) \tag{1.4b}$$

Where $q_{s,NET}$ and $q_{l,NET}$ is the relative velocities between certain species and the mean flow for small and large particles respectively. D_l is the diameter of the large particles. ϕ_l and ϕ_s are the expressions for the volume concentration of large and small particle respectively. $\tilde{q}_s$ and $\tilde{q}_l$ are the non-dimensional velocity of small and large particles respectively.

In Equations (1.4a) and (1.4b), one can see that the segregation trends only depend on the difference between non-dimensional velocities of small and large particles. In Savage and Lun [91], they derived very complicated formulations for $\tilde{q}_s$ and $\tilde{q}_l$, which only depend on six variables related to the geometric factors and particle properties. All those variables can be determined by empirical data, by which $\tilde{q}_s$ and $\tilde{q}_l$ can be calculated at different size ratio and bulk solids fraction. The theoretical calculations of Savage and Lun showed that $\tilde{q}_s$ was always larger than $\tilde{q}_l$ in a wide range of bulk solids fraction. This means the small particles sink to the bottom and large particles will rise.

Gray and Thornton [92] developed another theoretical model for the kinetic sieving mechanism. In their case, they explicitly consider flows down an inclined plane. They start from the equations of conservation of mass and momentum for mixture and each species and make two key assumptions to calculate segregation velocities. The first assumption they made includes an analogy with the percolation of fluids through porous solids and Darcy′s law to propose a formulation to calculate the inter-species force. This inter-species force includes a term resembling velocity-dependent drag force and a term related to partial pressure of one species. Another assumption is the partitioning of pressure between two species. They suggest the two species will not partition pressure only by local volume concentrations, but by a new scaling parameter which depends on both local concentrations and size ratio, where large particles support more pressure than small particles per unit volume. By incorporating these two formulations into the momentum equation of each species, they obtain an expression for segregation velocity of each species as follows,

$$q_{s,NET} = -(B/c)g\cos\theta\phi_l \tag{1.5a}$$

$$q_{l,NET} = (B/c)g\cos\theta\phi_s \tag{1.5b}$$

Here, B is a parameter that incorporates the non-trivial partitioning of pressure between species. c is the coefficient of inter-particle drag. g is the acceleration of gravity, and θ is the angle of the inclined plane to the horizontal. These formulations clearly show that large particles move upward to the free surface, while small particles sink under gravity.

If comparing the formulations for segregation velocity in Equation (1.4) and Equation (1.5), one can find that they generally have same structure as stated by [92]:

$$q_{s,NET} = -q^{sl}\phi_l \tag{1.6a}$$

$$q_{l,NET} = q^{sl}\phi_s \tag{1.6b}$$

where the mean segregation velocity $q^{sl} = D_l \frac{du}{dy}(\tilde{q}_s - \tilde{q}_l)$ in Savage and Lun model, and $q^{sl} = (B/c)g\cos\theta$ in Gray and Thornton model. Both these models have their advantages and disadvantages. In Savage and Lun model, all variables are given so that the segregation velocities can be easily calculated. In contrast, there are no formulations yet for the coefficient B and c in Gray and Thornton model so that these variables generally need to be fitted by experimental or simulation data. However, in Gray and Thornton model the gravity as the driving force for size segregation is explicitly shown in the formulation for segregation fluxes, while in Savage and Lun model gravity is not explicitly considered at all. Furthermore, note that in Savage and Lun the q^{sl} is also proportional to the local shear rate, which implies large segregation fluxes/velocites at higher shear rate. However, results in the experimental measurement of dependence of segregation velocities on shear rate by Stephens and Bridgwater [85] show that the linear relation may not be correct. In the Gray and Thornton model, shear rate dependence on segregation velocity is not initially considered. Recently, May et al. [86] added the linear shear rate relation on mean segregation velocity based on Gray and Thornton model to predict segregation in an annular Couette cell, but the theoretical predictions did not match experimental results quantitatively.

A primary mechanism proposed for density segregation is a 'buoyancy' argument proposed by Khakhar et al.[94], where they make an analogy to the separation of the conventional fluid mixtures. Segregation is driven by the competition between gravity force and an effective buoyancy force. The buoyancy force is calculated in terms of effective density, which is the volume averaged local densities of the mixtures. A qualitative description of 'buoyancy' mechanism states that a difference in density between one particle and its surroundings drives a less dense particle to the top because it experiences an upward force due to the density difference between itself and its environment. Khakhar et al. [94] proposed a quantitative expression for buoyancy-driven segregation in sheared granular flow. The segregation velocity of two species relative to the bulk is written as:

$$q_d = -C(\rho_d - \rho_l) g \cos\theta \phi_l \tag{1.7a}$$

$$q_l = C(\rho_d - \rho_l) g \cos\theta \phi_d \tag{1.7b}$$

Where, the subscripts d and l denote denser and less dense particles. Coefficient C is an unknown function that is inversely related to the resistance to local motion, ρ_d and ρ_l are material density for two species.

One may expect a mixing at certain combination of density and size ratio, since the two opposite trends of size and density segregation can cancel out. Drahun and Bridgwater [97] first attempted to address this issue in the experiments of chute flows by using small amount of tracer particles in the same sized bed. What they found is that at proper size and density ratio, an even distribution of tracer particles can be achieved. Later Alonso et al. [98] studied the free surface segregation in a 2-D rotating drum in the cascading regime. They theoretically developed a parameter S to compare the relative strength of density segregation (buoyancy driven) and size segregation (percolation driven) for 2-D system, where S is a function of density ratio, size ratio, system average porosity and species local solids fraction. The experimental results agreed with the theoretical prediction: (1) Density segregation dominates over size segregation when $S > 1$; (2) Size segregation dominates over density segregation when $S < 1$; (3) Density segregation balances size segregation when $S = 1$ to cause a perfect mixing. Metcalfe and Shattuck [99] first studied the segregation and mixing in avalanching regime in a 3-D rotation tube, where they found a mixing at certain combination of density and size ratio. Jain et al. [100, 101] systematically studied mixtures of glass and steel particles with size ratio from 0.25 to 20 in experiments in a pseudo 2-D rotating drum of different shape. They reported that for glass and steel particles they used, (1) when the size ratio $1 < d_r <$1.33, steel particles sink in the flowing layer. (2) For $1.5 < d_r < 2$, steel beads are located in between glass beads at the center and periphery of the drum. (3) As the size ratio $2 < d_r < 5$, steel beads are preferentially located near the periphery of the drum. (4) As the size ratio $d_r > 5$, steel beads and glass beads mix throughout the drum. Hill and Zhang [102, 103] performed computational simulations in a 2D rotating drum by varying the combination of particle size ratio and density ratio continuously. They obtained qualitatively similar results as Jain et al. [100, 101] that when size ratio is not big enough, there does not exist a combination of size and density ratio for mixing, but instead a 'band' pattern is observed. They argued that kinetic sieving-driven size segregation and buoyancy-driven density segregation may depend on the local porosity and shear rate of the mixture, while these effects have not been carefully considered in kinematic sieving and buoyancy models.

As mentioned, a gradient of shear rate and its associated gradient of granular temperature can drive species segregation of granular mixtures with different size and/or density in sparse and energetic regime (such as [28, 67, 87, 89, 88]). Within the framework of kinetic theory, several have derived explicit expressions for segregation in terms of external forces (e.g., gravity) and interactions between particles that depend explicitly only on the gradient of granular temperature, species concentrations, and particle properties (e.g., size and density). There have also been a number of reports of shear-induced segregation of particles in concentrated suspensions and slurries. Abbott and colleagues [104] showed that when concentrated particles suspensions were sheared in a circular Couette cell, large particles moved to the region of lower shear rate faster and, therefore, to segregate, similar to the case for sparse dry granular mixtures. Leighton, Acrivos, and colleagues [105, 106, 107] developed a diffusion model for this process based on consideration of a diffusion coefficient that depends both on local shear rate and particle size. Shauly et al.[108] developed an alternative diffusion model for this process that included shear rate gradient, curvature and viscosity gradient, which successfully predicted shear-induced segregation in dense suspension. Similar results were reported by Barentin and colleagues [109] in granular slurries..

While there have been relatively consistent reports for shear-induced segregation of different sized particles in dilute dry systems and in suspensions and slurries, the reports of analogous segregation in dry dense granular mixtures are somewhat more varied. Bridgwater and colleagues performed some of the earliest experiments used to study shear-induced size segregation in dry dense granular mixtures [85],[96],[110]. They found that in an annular shear cell where the shear is greatest in the middle of the cell [85], large particles move to the region of highest shear rate, directly opposite to the trend observed in dilute systems, in suspensions, and in slurries. They found similar results in a reciprocating simple shear cell with flexible walls [110]. Whether the shear gradient increased or decreased in the direction of gravity, they found that the large particles moved to the region of larger shear rate. Bridgwater attributed the shear-induced segregation to the gradient of solids fraction induced by the shear gradient.

Other observations of segregation in dense flows have been associated shear gradients and granular temperature gradients. Recently, Rietz and Stannarius [111] studied the kinematics of mixtures and their segregation properties in a long thin rectangular box rotated horizontally about its long axis. In these systems, the authors reported persistent convection rolls in the plane of the box and segregation patterns associated with these convection rolls. In this case, small particles accumulated on the outer edge of the convection rolls, associated with the largest shear gradients in the system, in contrast to the segregation observations reported by Bridgwater and colleagues [85],[110]. In another rotating system, this a long horizontal drum, Zuriguel *et al.* [112] studied the dynamics of relatively few large particles in a matrix of small particles when rotated in a long horizontal drum. In this case, the proximity of large particles altered the local velocity and granular temperature gradients, which themselves gave rise to segregation effects that varied with the rotation speed of the drum. At lower speeds, the proximity of two large particles resulted in a region of relatively low granular temperature between them. The large particles then migrated to this low temperature region, segregating from the small particle matrix. The dynamics reversed at higher speeds when the temperature gradients were small.

While many have observed rather consistent shear-induced segregation trends in sparse dry granular systems, suspensions and slurries, to this point, shear-induced segregation trends in denser dry systems appear somewhat inconsistent. Further, there is no clear physical or mathematical framework to explain how the gradient of shear rate may give rise to size segregation in dense flow, whether there is a single mechanism such as a gradient in granular temperature or pressure, or whether there are multiple mechanisms which dominate for different phases of granular flow. Part of the difficulty in developing an appropriate theory lies in the lack of an appropriate geometry for isolating shear gradients from other segregation effects. In typical experimental systems designed to study segregation in dense granular flow such as chutes and rotated drums, gravity, velocity gradients, and porosity gradients (and other effects) coexist in the direction of segregation. Therefore, in this research, systems are chosen based on their potential to isolate these factors from gravity and evaluate how these factors influence segregation in dense flow regime. Further, based on the experimental and computational results, a theoretical framework will be developed to model segregation mechanisms associated with gradients in shear rate in dense flow. In next section, the most widely used experimental techniques for studying the dynamics of granular materials will be introduced. Then, the goal and organization of this thesis will be presented in the subsequent section.

1.3 Experimental techniques

Due to the opacity of granular materials, it is difficult to access the bulk of granular flow quantitatively and often even qualitatively. Several experimental techniques are designed to provide insight of dynamic characteristics and validate computational model of granular flow. For example, nuclear magnetic resonance imaging (NMRI), positron emission tracking studies and X-rays tomograph have been used to measure granular flow in three dimensions, and particle tracking technique has been used to measure the structure and kinematics of granular flow in two dimension close to transparent boundaries.

NMRI is widely used to measure the flow structure and kinematics in the complex granular flow. NMRI has an advantage of non-invasiveness and no limit by opacity of granular materials. Many properties of flow can be measured by NMRI such as solids fraction, velocity and velocity fluctuations to reveal the development of microstructure of granular flow [113]. For example, NMRI was used to measure flowing parameters in the bulk flow such as solids fraction, velocity and velocity fluctuations in different systems like a rotating drum [114] and a split-bottom cell [115, 116]. Nakagawa et al. [114] found that in the rotating drum the velocity profile is asymmetric with a maximum near the center of the layer, and the concentration is low near the free surface but high near the bed. Cheng et al. [115] used NMRI to measure velocity profiles in the bulk of a split-bottom cell at different filling heights. They found in shallow flow below a critical value of filling height H_{cr}, an open shear band started from split line at bottom of cell to reach free surface and the width of shear band increased with increasing heights. However, in the deep flow, there is an onset of vertical shear band and the shear band are closed below free surface. Sakaie et al. [116] used NMRI to map the evolution of solids fraction in the bulk of split-bottom cell and found fairly strong dilatancy appeared and spread with rotations and the final degree of dilatancy was governed by the total amount of local strain experienced since the start of experiment.

NMRI was also performed to investigate the flowing pattern in the bulk flow of granular materials such as segregation. Metcalfe and Shattuck [99] used NMRI to study segregation in binary mixtures of particles with different size and density, and they found mixing for certain combination of particle size and density. Hill et al.[117] used NMRI to study the concentration variation of axial segregation in a long rotating drum. Ehrichs et al. [118] measured velocity fields in a vibrated granular bed and observed a granular convection cell, which can induce Brazil Nut Problem(BNP) revealed by Knight et al. [57]

Positron emission particle tracking (PEPT) is a technique for following the motion of a radioactively labeled tracer particle, so that non-invasive tracking is possible inside the bulk of granular flow. Broadbent et al. [119] Used PEPT to investigate geometric effect of a blend mixer on mixing efficiency by track tracer particles. Parker et al. [120]

performed PEPT technique in a rotating drum to investigate the position of flowing layer by measuring the velocity profiles and distributions.

X-ray tomography imaging technology is another promising technique that recently has been applied to granular flow studies. X-ray tomography provides a quick and nondestructive measurement with high resolution and high penetration. It could be used to reconstruct 3D micro-structures and efficiently measure microstructure evolution of granular materials. Mueth et al. [121] used both NMRI and X-ray tomography to study the internal velocity of granular materials in a Couette cell. McDonald et al. [122] used X-ray tomography technique to trace the movement of aluminium powder during transfer, brought about by the lowering of a punch into a cylindrical die containing an un-compacted aluminium/tin powder blend and measure velocity fields around punch.

Confocal microscopy in conjunction with index-matched particles and fluids has recently shown some promise [123]. However, due to the opacity of the granular materials, this technique can only be used if the particles are emersed in an index-matched fluid, so it is restricted to wet granular flows.

Recently, particle tracking from two-dimensional images taken using digital cameras have revealed much of the structure and kinematics of granular flow such as Refs. [124, 125, 126], who used this technique to study the kinematics of granular flow in rotating drums. Another application of this technique can be used to visualize and study the segregation kinematics of a granular mixture close to boundaries such as free surface, or transparent side walls by making different species visually different (e.g. Coloring), by which the evolution of concentration of species and segregation kinematics can be qualitatively and quantitatively measured.

Most of these techniques introduced above are restrictive in terms of system size, boundaries, particle type or their prohibitively expensive cost. For example, X-ray tomography can not be used on metals. NMRI can only use certain types of materials, which make it difficult to study the property effect on flow kinematics and patterns. The particle tracking method is less restrictive in terms of particle properties, but due to the opacity of granular materials, it cannot be used for three-dimensional studies. The behavior of granular systems has been shown to be influenced by their boundaries [127, 128], which restricts this technique to two- dimensional behavior and the behavior of three-dimensional flow near boundaries.

Therefore, in current research, photos are taken to qualitatively investigate the bulk behavior after excavating bulk particles with a home-made small shovel. To investigate the segregation at free surface, a digital camera is used to record segregation progress. Segregation kinematics such as segregation rate can be calculated by extracting gray-scale values from images taken from experiments. The details about measuring and processing methods are presented in section 2.2.

For the research described here, simultaneous bulk concentrations and forces are needed for model development and validation involving segregation in dense sheared flow. Therefore, more detailed and extensive simulations are conducted to extract simulation information about forces and local dynamics. A separate chapter (Chapter 3) is devoted to reviewing available simulation techniques and specific simulation techniques used in this thesis.

1.4 Goal and organization of current research

The goal of this research is to isolate specific segregation effects in dense granular materials with a particular focus on the effect of a shear rate gradient and its associated gradients of granular temperature and/or solids fraction. The rest of this thesis is organized as follows. In Chapter 2, physical experiments used to isolate and investigate effects of different driving mechanisms on segregation of dense granular mixtures in a split-bottom cell are described. Chapter 3 presents the computational techniques used for dense granular flows in this research. In Chapter 4, computational simulations in the split-bottom cell used to investigate the segregation in the bulk are presented. In Chapter 5, simulation results from a vertical chute cell will be presented where the effect of total solids fraction on the segregation behavior is elucidated. In Chapter 6, a hydrodynamic model is developed based on computational simulations in the vertical chute cell to model shear-induced segregation of dense granular mixtures. Chapter 7 presents conclusions with some brief additional discussions of potential future research directions.

Chapter 2

Experiments in a split-bottom cell

In most experimental modeling of segregation in dense sheared system, different segregation drivers such as gradients of shear rate and gravity are impossible to separate. In this Chapter, experiments in a split-bottom cell are presented in which some of these effects can be isolated.

2.1 Experimental apparatus and set-up

2.1.1 Experimental apparatus

The split-bottom cell was first proposed by Fenistein et al. [129, 130] [Fig. 2.1(a)]. In the system used here, the bottom of a cylindrical container of radius $R_o = 145$ mm is split at radius $r = R_s = 121$ mm, and the outer part of the disk is fixed to the curved vertical cylinder walls. The inner disk is rotated at angular velocity, $\Omega = \frac{1}{100}$ rps and the outer surface is fixed. The boundary friction is controlled using a layer of 2 mm glass particles glued to the base of the cell. The cell is filled with granular materials to a height $H \sim R_s/3$. As shown by Refs. [115, 129, 130, 131, 132], at these fill levels, a cylindrically symmetric – primarily vertical – shear band is produced in the bulk of the granular materials: near the bottom the band is narrow and centered at the split; with increasing distance from the bottom z, the band moves inward with an upward

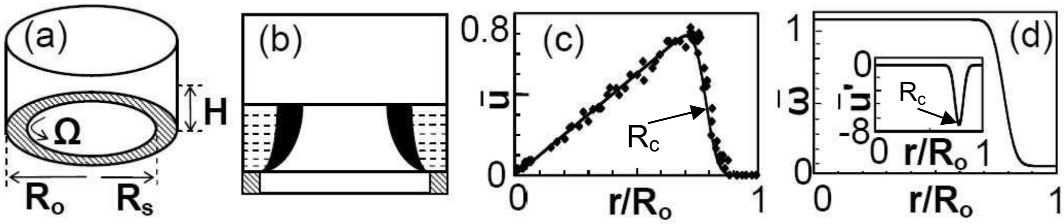

Figure 2.1: (a) Sketch of a split bottom cell. Ω is the rotation speed of the base. (b) Sketch of bulk shear band (black). (c) Measured surface velocity as a function of radial position (symbols) for 1 and 3 mm glass particle mixture filled to $H \approx R_s/3$ as described in text. Solid line is $\overline{u} = \overline{r} * \overline{\omega} = \overline{r} * [1/2 - 1/2 \text{ erf}((r - R_c)/W)]$, where $\overline{r} = r/R_o$; $\overline{\omega} = \omega/\Omega$, and ω is the local angular velocity. $R_c = 115.3$ mm and $W = 7.9$ mm for this mixture; (d) shows the radial dependence of $\overline{\omega}$ and $\overline{u}' = \overline{r}\frac{d\overline{\omega}}{d\overline{r}}$. Copyright (2008) by the American Physical Society.

curvature, and its width increases [See Fig. 2.1(b)]. As shown in [115, 130, 132], both at the surface and in the bulk, the angular velocity profiles may be fit using an error function as shown in equation (2.1),

$$\omega/\Omega = 1/2 - 1/2\text{erf}[(r - R_c)/W] \tag{2.1}$$

where ω is local angular velocity at radius r, R_c is center of shear band and W is width of shear band [See Fig. 2.1(c)]. The shear rate profile is Gaussian and shear rate is greatest near the middle of the shear band R_c [See Fig. 2.1(d)]. While both R_c and W have physical meaning, their fundamental form is unknown and hence they are essentially fitting parameters in equation (2.1). The center of shear band R_c is dependent on the filling height H, distance from the bottom z and R_s. The width of shear band W is dependent on filling height H, distance from the bottom z and particles diameter d as described in Refs. [130, 132]. In this system, in contrast to free surface gravity-driven flow such as flow in a rotating drum or a chute flow down an inclined plane, the gradient of shear rate is primarily perpendicular to gravity, though there is a small deviation from this particularly near the base. Close to the free surface, there is presumably a solids fraction gradient coincident to gravity.

When the filling height H exceeds 0.6 R_s, experimental, computational and theoretical results [115, 130, 132] show a different flow structure: An additional vertical shear

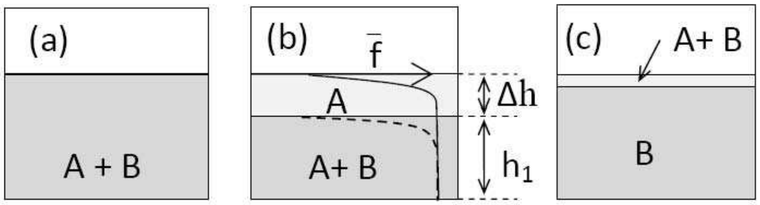

Figure 2.2: (a) Sketch of the set-up for experiment set I. (b) Sketch of the set-up for experiment set II. The dashed line is expected solid volume fraction for mixture of components A+B filled to height h_1 and solid line for the same, with overburden of A, described in the text. (c) Sketch of the set-up for experiment set III. Copyright (2008) by the American Physical Society.

band appears in axial direction. A vertical shear rate gradient will complicate the study of shear-driven segregation, so experimental filling height H is limited to less than 0.6 R_s.

2.1.2 Experimental setups

Three sets of experiments – i.e., initial conditions – are used to study the effects of three possible external segregation driving mechanisms: gravity, porosity, and shear gradient [See Fig. 2.2]. Experiment set I is the simplest: The cylinder is simply filled to height H with a well-mixed binary mixture [Fig. 2.2(a)]. In experiment set II, the container is filled with the mixture to height h_1 and covered by an overburden – a layer of thickness Δh of monosized particles [Fig. 2.2(b)]. In this way, any surficial solids fraction gradient are moved away from the top of the mixed phase. To prevent exchange of different types of particles at the interface between the mixture and the overburden, this top layer must consist of particles that "float" on the mixture. The choice does not appear to influence the results, and typically the less dense or larger particles in the mixtures are used (depending on whether the components in the mixtures differ only in density or size, respectively). In experiment set III, the effects of the shear gradient are isolated in the horizontal direction, with the use of a thin layer of a mixture on top of a supporting base of one type of particle [Fig. 2.2(c)]. To prevent exchange of different types of particles at the interface of the mixture and the supporting matrix, the particles in the base must consist of particles that would sink in the mixture; either the denser or smaller particles in the mixtures are used, depending on whether the components differ in density or size.

2.2 Measuring and processing methods

Preparation Procedures-Particles in a binary mixture are chosen from different sizes (diameter d = 0.5, 1, 2 and 3 mm) and different materials (steel, plastic and glass from Jaygo Inc. NJ, USA) to achieve different combinations of size or density ratios. To distinguish different species in the segregation experiments by eyes or camera, the particles are dyed with different colors (the plastic particles have been colored by the manufacturer). Before filling granular materials in the split-bottom cell, anti-static spray is used to minimize possible electrostatic effects between particle-particle and particle-walls. Then the granular materials are carefully and slowly filled in the cell to prevent potential segregation during pouring and then the surface is flatten gently using a circular disk with diameter slightly smaller than R_o minimizing any compression on the granular materials in the cell.

Measuring Procedures-In all three experimental setups introduced in Section 2.1.2, segregation could occur either at free surface or subsurface or both locations. To record and investigate the evolutions and patterns of segregation at free surface, a digital camera is focused on the top of the split-bottom cell. The camera begins to record slightly before the start of rotation and stops recording slightly after the cell stops so that the whole process of segregation can be recorded. The recording frequency is 1 frame per second. As mentioned in Section 1.3, current techniques to access bulk kinematics and dynamics for granular materials are greatly restricted. To determine the evolution of segregation in the bulk for these experiments, several consecutive experiments of increasing duration are performed. After each run of progressively longer duration, the layers of particles are removed incrementally and a digital camera is used to record the segregation state at each depth. Then the particles ar remixed and the experiment is restarted (from time t = 0). Each run is repeated at least three times to assure reproducibility of experimental results.

Processing Procedures- Since the particles have been colored in the experiments, in the photos taken by the digital camera, it is easy to distinguish two different species by the grayscale values. In order to study the spatial distribution of the segregating two species and segregation rates, a free software package Scion Image is used to extract gray scale values of each pixel in a selected area (mostly in the shear zone where segregation happens). Then these values are averaged in azimuth direction to obtain radial profiles of the grayscale values in every time step. At the beginning of experiments, because the two species are well-mixed, evenly distributed gray values is expected. As segregation proceeds, the two different species of particles represented by different grayscales in the photos begin to accumulate in different regions radially, so that the radial profiles of grayscale become uneven. After obtaining the profiles of grayscale values during the course of an experiment, all these profiles are combined together to plot a contour of evolution of segregation progress in grayscale. This provides a quantitative picture of the segregation.

Segregation rate is also investigated by measuring the width of segregating band at surface. When a certain species accumulates together in one region, the value of grayscale will be either very large (black:255) or very small (white:1). Considering this, a cutoff value is set to determine the borders of the segregating band at each time step and to determine a reproducible measure of the width of segregating band as a function of time.

Using these methods, it is nearly impossible to obtain quantitative results in the bulk comparable with those measured at free surface. Therefore, a qualitative analysis is performed to determine bulk segregation. The bulk segregation patterns (if any) are investigated by interpreting photos taken during excavation in experiments and also by measuring geometric structure of segregation patterns such as the location and width of segregated bands in the bulk.

2.3 Results and discussion

In this section, results of segregation with particles differing only in size and with particles differing only in material density will be presented. Then these results will be discussed.

2.3.1 Segregation for particles differing only in size

For mixtures of particles differing only in size, in experimental set I, a band of large beads quickly forms at the top surface, widens and reaches steady state in less than 10 rotations [See photos in Fig. 2.3(a)-(c)]. Fig. 2.3(d) shows the evolution of the segregated band visible from the top using a portion of each image taken at one frame per second as described in Section 2.2. There is no apparent depletion of the larger particles outside the band, indicating that dominant segregation process is occurring in the vertical direction at surface. To determine the evolution of segregation in the bulk for these experiments, several consecutive experiments of increasing duration are performed and materials are excavated, as described in Section 2.2. The results from the bulk excavations indicate that, within 2-3 rotations of the base, the segregated zone of large particles extends at least 1-2 layers beneath the free surface and that, further, there is a small segregated region of small particles region near the base of the cell. When experiments have run for approximately 10 rotations, the segregated band of large particles grows downward further, but the vertical growth is limited to a maximum depth $10\overline{d}$ ($\overline{d}$ is the average diameters of particles). A segregation zone of small particles forms at the base but the zone of small particles does not grow [Fig. 2.3 (e) and (f)], which leaves a region of mixed particles in the middle of split-bottom cell.

However, when the rotation continues for a longer time, on the order of hundreds of rotations or more, much slower horizontal segregation in the bulk is observed [Fig. 2.3 (g)]. The particles within the bulk begin to segregate in the radial direction, in other words, in the direction of the horizontal shear rate gradient. A cylindrical shell of small particles forms within the shear band at smaller radii, and a band of large particles occupies the outer part of the shear band. This horizontal segregation is a much slower process than vertical gravity-driven segregation and appears to reach a steady state after over one hundred revolutions.

In experimental set II, where an overburden of thickness Δh is placed on top of the mixture, similar phenomena are observed as experimental set I. Segregation in the bulk is either reduced or eliminated by the overburden when experiments run in less than 10 rotations. That is, for small enough values of Δh, a segregated region of large particles forms at the top and grows downward, but the final depth of the particles is reduced, approximately by Δh, and apparently eliminated for $\Delta h > 10\overline{d}$ [Sketched in

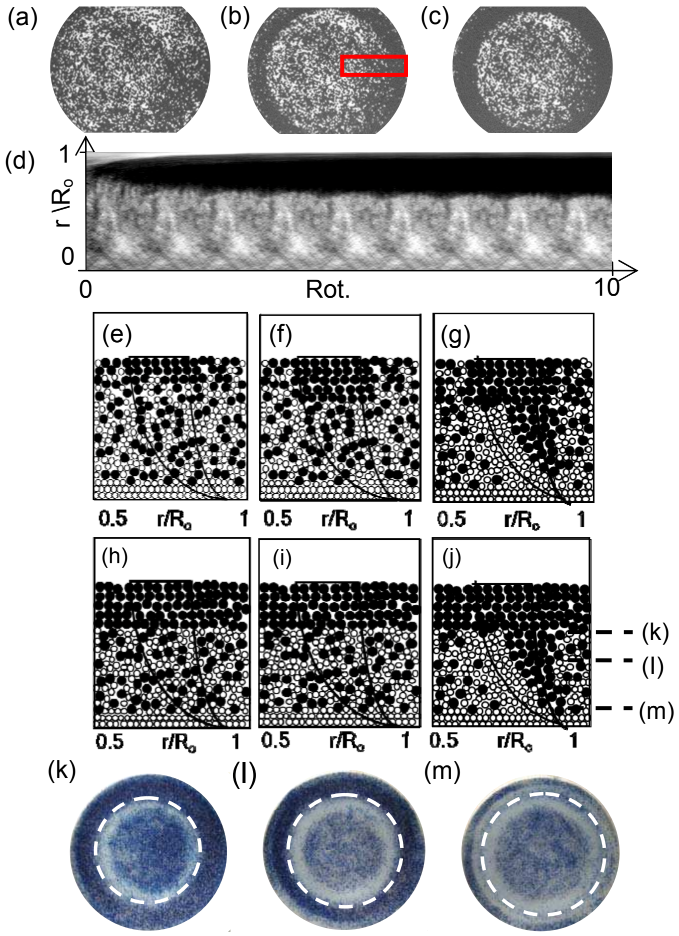

Figure 2.3: Measurements of segregation in binary mixtures differing only in *size* for experiments set I and II. (a)-(c) Photos taken from experiment set I at surface with 1mm (white) and 3mm (dark) glass particles at H=40mm at (a) 0 , (b) 5 and (c) 10 rotations. (d) A compilation of this information using average pixel values in the region indicated in (b) from each image taken throughout the experiment as described in text. (e)-(g) Sketches of bulk segregation for this experiment after (e) 2, (f) 10 and (g) >100 rotations. (h)-(j) Sketches of bulk segregation for experiments set II at $\Delta h > 10\overline{d}$ after (h) 2, (i) 10 and (j) > 100 rotations. (k)-(m) are photos taken from set II with 1mm (white) and 2mm (dark) glass particles with h_1=40mm and Δh=15mm at 300 rotations at different heights z : (k) 40mm, (l) 30mm and (m) 10mm. The dotted lines are predicted centers of shear zone by Equation (2.2). Copyright (2008) and (2010) by the American Physical Society.

Fig. 2.3 (h) and (i)]. These results appear independent of the choice of h_1 and indicate that either a solids fraction gradient or a velocity gradient must be present to assist gravity-driven size segregation. However, for a longer rotation time, bulk horizontal segregation patterns also have been observed similar to that of experimental set I [Fig. 2.3 (j)]. That is, a cylindrical shell of small particles forms within the shear band at smaller radii, and a band of large particles occupies the outer part of the shear band.

Figures. 2.3 (k)-(m) show photographs taken from one such experiment run such as that illustrated in Figs. 2.3 (h)-(j) during the bulk excavation process. Heights for each are specified in the figure caption. For the top two positions [Figs. 2.3 (k)-(i)], there are four cylindrical shells of different phases of the mixture: at smaller radii where the shear rate is negligible during the experiment, the system remains mixed. At intermediate radii, a lighter band of small particles is noticeable. At larger radii, a darker band of larger particles is visible in the region of the shear band, and at the largest radii, adjacent to the outer wall, the system is mixed. At the lowest position [Fig. 2.3 (m)] very few large particles are visible, presumably due to vertical segregation of the large particles away from the bottom. At this point, only small particles are visible throughout the shear band and only the mixed phase is visible in the inner and outer region.

Dashed lines shown in Figs. 2.3 (k)-(m), denote the centers of shear zone, the region of the highest shear, as calculated by Equation. 2.2 proposed by Ref. [132].

$$z = H - R_c[1 - R_s/R_c(1 - (H/R_s)^{2.5})]^{0.4} \tag{2.2}$$

It is interesting to note that rather than indicating that the small particles or large particles segregate to a higher or lower shear rate, these results indicate that the bands of small and large particles are separated approximately by R_c, the location of the highest shear rate. While the horizontal segregation patterns in the experiments indicate shear-induced segregation patterns, the results are markedly different from previous observations of shear-induced size segregation in dense flow. In other words, in the split-bottom cell, the highest shear rate marks the border between segregated small and large particles. Others have found either large [85, 110] or small [111] particles segregate to higher shear rate. The underlying reasons for these discrepancies will be presented and discussed later in Chapter 4 where more detailed information in the bulk such as the species concentrations, velocities, and granular temperatures is available through

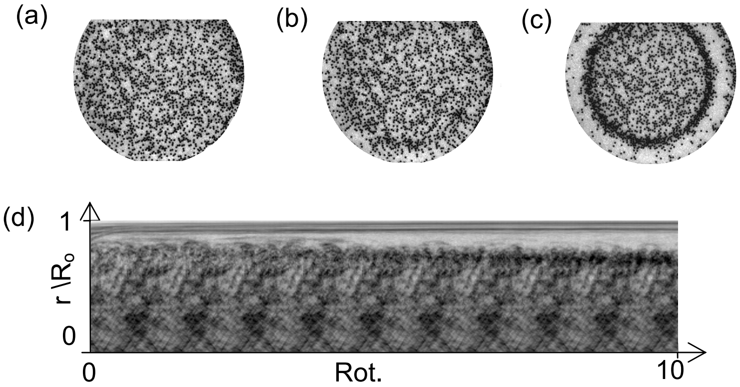

Figure 2.4: Measurements of segregation in binary mixtures differing only in *size* for experiments setup III. (a)-(c) photos taken from experiment setup III at surface with 1 mm (white) and 3 mm (dark) glass particles at H=40mm at different rotations: (a) 0 , (b) 1 and (c) 10. (d) Compilation of such surficial segregation using same methods as Fig. 2.3(d).

computational simulations.

When a mixture of different sized particles is placed on a substrate of smaller particles (Experiment set III), a different segregation pattern emerges: A quick initial outward migration of the larger particles is followed after some delay by a slower vacation of the rest of these particles inward [Fig. 2.4]. These two stages of segregation may be due to two separate phenomena. The initial quick movement of the larger particles outward appears similar to the curvature-induced migration of larger spheres in a bidisperse suspension reported by Krishnan, Beimfohr, and Leighton [107]. The slower more complete evacuation of the shear band is more likely due to dynamics associated with the velocity gradient in the shear band such as a temperature gradient in experiments reported by Zuriguel et al. [112].

The time dependence of the surficial segregation in experiments I and III is also investigated via the width of the surface band Δr in two mixtures of different sized particles [Fig. 2.5]. For both types of experiments, once the band starts to grow, the width of the band is well fit with an exponential equation $\Delta r(t)/R_0 \approx A_0(1 - e^{-t/t_0})$. However, the initial growth of the band for experiments of type III is delayed by some time t_d nearly equal to the typical growth time for experiment setup I.

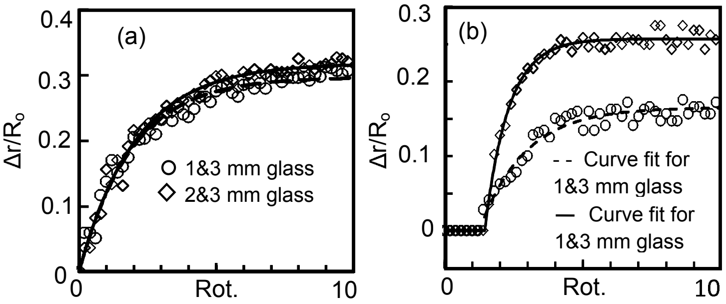

Figure 2.5: Segregation rate reprsented by the width of surface band Δr versus time for experiment set I and III, respectively, using mixtures of different sized particles: 1 and 3 mm glass and 2 and 3 mm glass, respectively. Here the width Δr is considered nonzero only for a region of the band purged of one type of particle. The lines are exponential fits $\Delta r(t)/R_0 \approx A_0(1 - e^{-t/t_0})$ to the experimental data for $t > t_d$. For experiment I, $(A_0; t_0; t_d)_{1\&3} = (0.32; 207s; 0s)$ and $(A_0; t_0; t_d)_{2\&3}$=(0.30; 192s; 0s). For experiment III, $(A_0; t_0; t_d)_{1\&3}$ =(0.17; 163s; 126s) and $(A_0; t_0; t_d)_{2\&3}$=(0.26; 85s; 146s). Copyright (2008) by the American Physical Society.

2.3.2 Segregation for particles differing only in material density

Many of the results obtained using particles differing only in density are similar to those obtained using particles differing only in size, though there are a few key differences. When mixtures of particles differing only in material density are sheared in the cell as in experiment set I, a segregated ring of the lighter component appears at the center of the shear zone similar to larger particles in the size segregation in section 2.3.1 [Figs. 2.6 (a) and (b)], visible within a single rotation of the base. As rotation continues, this segregation band widens until a maximum width is reached [Figs. 2.6 (c)]. Figs. 2.6 (d) shows the evolution of the segregated band visible from the top. There is also no apparent depletion of the less dense particles (or higher fraction of denser particles) outside the band, indicating that the dominant segregating process is occurring in the vertical direction.

The results from the bulk excavations [Figs. 2.6 (e)-(g)] indicate some differences of segregation with particles differing only in size. Essentially, the segregation is faster and more extensive in the mixtures of particles differing only in density. Within one rotation of the base, the segregated zone of less dense particles extends at least 1-2

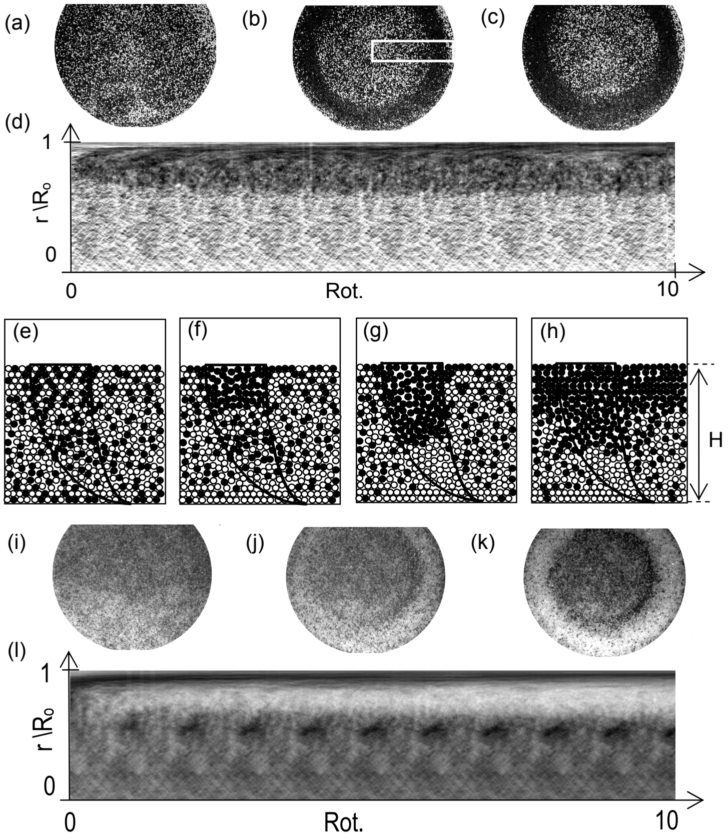

Figure 2.6: Measurements of segregation in binary mixtures differing only in *density* for experiments setup I, II and III. (a)-(c) Pictures of the surface for experiments set I after (a) 0, (b) 1, and (c) 10 rotations for a mixture of 2 mm steel (white) and glass (black) particles. (d) A compilation of surficial segregation using same method as that in Fig. 2.3 (d). (e)-(g) Sketches of bulk segregation from similar experiments at (e) 0, (f) 5, and (g) 10 rotations. (h) Sketch of segregation of the final segregation state for these mixtures from experiments of type II. (i)-(k) Pictures of the surface segregation for an experiment of type III using a mixture of 3 mm glass particles (dark), and plastic particles (white) after (i) 0, (j) 1, and (k) 10 rotations. (l) A compilation of the experiment set III similar to that shown in (d). Copyright (2008) by the American Physical Society.

layers beneath the free surface and, further, there is a small segregated region of denser particles region near the base of the cell. With further rotation, the two segregated zones actually grow toward each other until they meet in the middle. Based on comparisons with 3D measurements [115, 129, 130, 131], the segregation is primarily limited to the bulk shear zone.

In experiment set II, segregation of these mixtures progresses in the very same way that it does without the overburden. Segregation zones of lighter particles form at the top of the sheared region, and a segregation zone of denser particles forms at the bottom; they both grow and meet in the middle [final state illustrated in Fig. 2.6 (h)]. Experiments setup I and II show that mixtures of particles differing only in density behave as one might expect from an emulsion of immiscible fluids of different densities. That is, particles of different density than the surrounding sheared fluidlike mixture rise or fall according to their relative densities, and a solids fraction gradient has little or no effect, which is totally different from size segregation.

Experiment set III illustrates the effect of the isolated horizontal shear gradient on these mixtures: The particles that are less dense drift horizontally relative to the mixture to regions of lower shear rate as large particles perform in size segregation [Figs. 2.6 (i)-(k)]. A quick initial migration of a few lighter particles to the outer edge of the shear band is followed by a slower vacation of most of these particles to the inner edge of the shear band. Fig. 2.6 (l) shows the time dependence of the top segregated band similar to that shown in Fig. 2.6 (d) for experiment setup I.

2.3.3 Lessons learned from isolating segregation mechanisms in a split-bottom cell

To summarize, experiments are performed with granular mixtures of different size only and material density only in three different experiment setups to investigate effects of porosity variations, gradients of shear rate on the segregation. Both surface segregation and bulk segregation are observed in the experiments for mixtures of particles differing size only or material density only, but the underlying mechanisms seem to be different.

For different sized particles, vertical gravity-driven segregation is strong and fast at boundaries such as the free surface and the bottom of the cell. However, in the bulk where the solids volume fraction is very high, gravity alone does not drive segregation associated with particle size without a sufficiently large porosity or porosity gradient shown in experiment set I and II when the cell is rotated in a short time scale. However, instead, a much slower horizontal segregation pattern evolves in the bulk, where small particles accumulate in the region with small radii and large particles segregate to the outer radii and the two segregated shells of small and large particles are separated by the center of shear zone (also the largest shear rate and granular temperature). Although this horizontal segregation pattern seems to coincide with a horizontal gradient of shear rate, the segregation pattern differs from previous reported shear-induced segregation pattern in dense flow, where either large [85, 110] or small [111] particles tend to segregate to regions of higher shear rate.

In contrast to horizontal size segregation in the bulk, the horizontal size segregation at free surface in experiment set III behaves like shear-induced segregation in the energetic sparse flow where large particles segregate to the regions of lower shear rate and granular temperature, and small particles accumulate to the regions of higher shear rate and granular temperature. The curvature effect on segregation may also exist as described in Section 2.3.1.

Compared to size segregation, density segregation in the split-bottom cell is relatively simple. The vertical gravity-driven segregation shows same segregation trend as those in rotating drum or chute flow, in which dense particles sink along with the direction of gravity to the bottom of the cell and large particles rise to free surface. Different from size segregation, the effect of gravity on density segregation does not need a gradient of shear rate or porosity in the bulk. Therefore, the vertical density segregation occurs through the whole shear zone in the bulk, and these vertical gravity-driven segregation seems to suppress any possible horizontal segregation related to gradients of shear rate and temperature in the bulk. In experimental set III, mixtures of particles differing only in density behave similarly to those differing only in size at the free surface: The particles that are less dense drift horizontally relative to the mixture to regions of lower shear rate. Since the solids fraction is very low at the free surface, this segregation behavior could be modeled by the mechanisms for the segregation in sparse and energetic flow, which will not be discussed further in this research.

Because of the lack of evidence for shear-induced segregation in particle mixtures varying only in density, in the rest of this thesis only the bulk segregation of particles differing size only will be focused, where a horizontal segregation pattern is observed and coincides with gradients of shear rate. Because of the restriction of physical experiments, the rest of the work described in this thesis involves simulations. The technical details of these simulations are described in the next chapter.

Chapter 3

Computational techniques for dense granular flow

Numerical simulation currently is one of the most popular ways to study bulk flow of dense granular materials, particularly given the tremendous speeds of computer processor. The lack of continuum models for dense flows has motivated the development of discrete simulation methods. There are several different discrete simulation techniques used to simulate flows of granular materials. Monte Carlo Method and Discrete Element Method are two of the most widely used and will be briefly reviewed here.

3.1 Monte Carlo Method

The Monte Carlo Method is often used to model dilute granular materials. In Mote Carlo Method, the state of granular gas is described by a *one-particle distribution function*: $f(\vec{x}, \vec{v}, t)$. This quantifies the number of particles $f(\vec{x}, \vec{v}, t)d\vec{x}d\vec{v}$ that are located in an infinitesimal volume of $d\vec{x}$ at position $\vec{x}$ and whose velocity are in the infinitesimal interval $d\vec{v}$ around $\vec{v}$, at time t. From this, the kinematic properties of the mean flow such as the total number of particles in full phase space N, particle number density n, flow velocity $\vec{u}(\vec{x}, t)$ and granular temperature $\vec{T}(\vec{x}, t)$ can be calculated.

The distribution function $f(\vec{x}, \vec{v}, t)$ is time dependent and it follows Botlzmann transport equation during simulations

$$(\frac{\partial}{\partial t} + \vec{v}_1 \cdot \nabla) f(\vec{x}, \vec{v}_1, t) = I \tag{3.1}$$

Here I is the collision integral, which depends on collision mechanisms and relationships involving interparticle collisions. The expression and derivation of I can be found in Poschel and Schwager [133].

The Boltzmann Equation (3.1) is based in part on the assumption that each particle in the system moves independently, which is not true in real systems. Therefore two-particle distribution function $f_2(\vec{v}_1, \vec{v}_2, \vec{x}_1, \vec{x}_2, t)$ cannot be simply calculated by $f(\vec{v}_1, t) f(\vec{v}_2, t)$. A correction factor need to be added to represent correlations of collision. One of the simplest is the Enskog factor g_2, by which Boltzmann equation (3.1) becomes Boltzmann-Enskog equation:

$$(\frac{\partial}{\partial t} + \vec{v}_1 \cdot \nabla) f(\vec{x}, \vec{v}_1, t) = g_2 I \tag{3.2}$$

g_2 depends on the particle number density: $g_2 = (2-\eta)/2(1-\eta)^2$, where $\eta = \frac{4}{3}\pi n R^3$ and R is the radius of particles.

Since the collisions between particles are considered as binary and instantaneous, the Monte Carlo method can provide a good estimate for fast, energetic granular flows with relatively low computational intensity. Rosato et al. [53] used Monte Carlo simulations to study the segregation in mixtures of particles differing in size when vertically vibrated. They observed the phenomenon of larger particles aggregating to the top of small particles (BNP), and a percolation mechanism was proposed to explain this phenomenon. Monte Carlo simulations were also used to model segregation in an isothermal gravitational field [68], model granular relaxation of a pile [134] or model simple shear flow based on the theoretical framework of the kinetic theory of dense gas [135]. However, the Monte Carlo method cannot be used to the dense flow, as this method is based on the assumption of binary and instantaneous collisions between particles, while particles in dense flow interact with multiple and enduring contacts.

3.2 Discrete Element Method (DEM) models

The Discrete (Distinct) Element Method (DEM) incorporate more detailed interaction model that includes details between particle interactions. This method is more realistic than Monte Carlo method since it is based on approximate models of the interactions between particles, although it is very computationally intensive, and numerical parameters for particle interactions are needed. There are several different contacting models for different regimes of granular flows, which basically fall into two categories: (1) A hard sphere model for energetic and sparse flows, in which the collisions between particles are dominant. (2) A soft sphere model for very dense and slow granular flows where geometric effects between particles are dominant. In this section the hard sphere model is briefly reviewed

In hard sphere model, the interaction forces are considered to be impulsive and the particle collisions are assumed to be the binary and instantaneous. The collisions are the only means for exchanging momentum, and post-collision velocities are calculated based on momentum conservation, which means the instantaneous interaction forces between particles during collisions are actually not calculated. The energy in the system is dissipated only by collisions determined by the coefficient of restitution. During the simulation, particles are assumed to move undisturbed until a collision event happens, so this model is also called the event-driven simulation. Hard sphere models are very computationally efficient for sparse flows, where the frequency of collisions or events are relatively small.

Event-driven simulations have been widely applied to simulate sparse granular flows because of its relative low computational intensity and good matching with experimental observations and theoretical predictions. For example, Luding et al. [136] used both molecular dynamics simulations and event-driven simulations to simulate a two-dimensional vibrated bed and found a scaling law between the height of the center of mass and external vibration parameters. Alam and Luding [137] studied rheology of bidisperse granular mixtures via event-driven simulations and compared with predictions from kinetic theory. They systematically studies stresses dependence on size ratio, system solids fraction and fraction of each species. Event-driven simulations were also applied to simulate the rheology and velocity distributions in the vertical chute flow by

Alam and colleagues [82, 138] to compare with kinetic theory predictions.

In the dense flow, event-driven simulations become less efficient due to dramatically increased numbers of collisions and are also not capable of modeling multiple and enduring contacts. The soft sphere model, on the other hand, accounts for multiple and enduring contacts by tracking the dynamics of particle contacts. To understand this method, it is helpful to review the DEM method as it applies to the soft sphere model in a bit more detail.

3.3 DEM simulations for dense sheared granular materials using soft sphere models

3.3.1 Simulation scheme

The idea of DEM simulation is very straightforward. It tracks the motion of each individual particle in the simulation domain by Newton equations of motion shown in equation (3.3), which are used to update translational, angular velocities and coordinates of each individual particle.

$$\begin{aligned} \frac{\partial^2 \vec{x}_i}{\partial t^2} &= \frac{1}{m_i}\vec{F}_i(\vec{x}_j, \vec{v}_j, \vec{\phi}_j, \vec{\omega}_j) \\ \frac{\partial^2 \vec{\phi}_i}{\partial t^2} &= \frac{1}{\vec{J}_i}\vec{M}_i(\vec{x}_j, \vec{v}_j, \vec{\phi}_j, \vec{\omega}_j) \\ j &= (1, ..., N). \end{aligned} \tag{3.3}$$

The force $\vec{F}_i$, the torque $\vec{M}_i$, and the tensorial moment of inertia $\vec{J}_i$, acting on particle i of mass m_i, are functions of particle positions $\vec{x}_j$, the angular orientations $\vec{\phi}_j$, the corresponding translational velocities $\vec{v}_j$ and angular velocities $\vec{\omega}_j$. Specific force laws are used to calculate forces and torques of each pairwise contact between discrete particles. The details of force models used in this research will be introduced in detailed in next subsection.

The simulation process is illustrated in the Fig. 3.1. There are six steps in the simulations: (1) Initialize the simulation configuration, including reading simulation parameters and building up a neighbor list. (2) Calculate forces on each solid component; to meet requirements for accuracy of simulations, different time-integration scheme can be

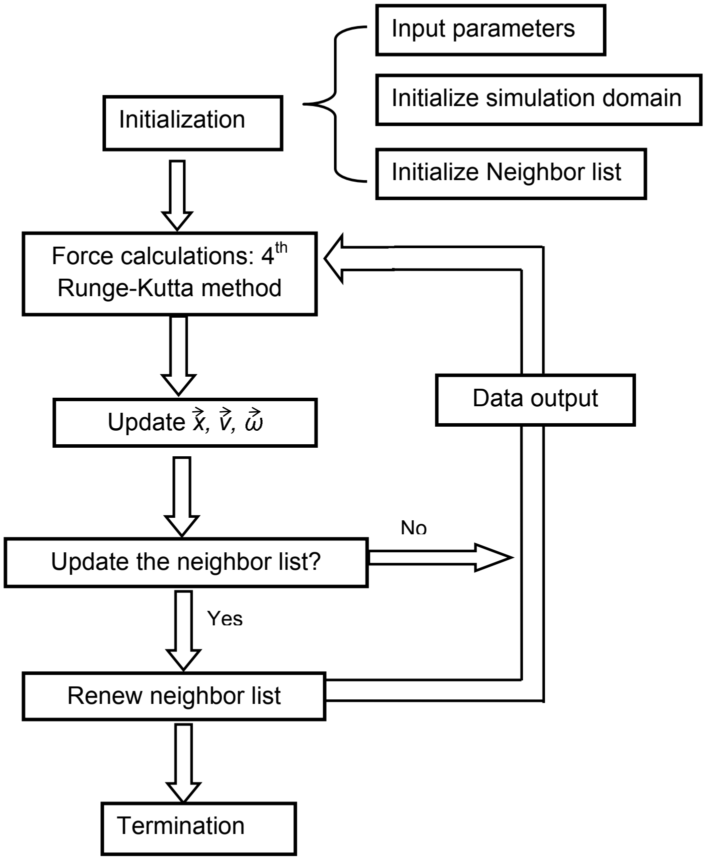

Figure 3.1: Flow chart of DEM simulation scheme.

chosen. In this research, fourth order Runge-kutta method is used. (3) Proceed in time by solving Newton laws in equation (3.3) and integrate it to get each solid component's velocity, position in next time step. (4) Update the neighbor list when it is necessary. (5) Output data if necessary. (6) Continue from step (2) or terminate the program.

There are several factors that make DEM simulation computationally expensive. One of these is the particle-contact search. If the simulation code tracks each pair of particles in the whole simulation domain to calculate forces between contacting particles, the efficiency is very low. To avoid unnecessary calculations, a neighbor list is built, in which particles that contact or may possibly be in contact in next the few time steps are stored. By using neighbor list technique, the computational time for contact search is decreased. Several algorithms for this have been developed such as the Verlet algorithm, the link cell algorithm and a lattice algorithm. In this research, the Verlet algorithm is used to build neighbor list and will be introduced briefly below. Details of other algorithms can be found in Ref. [133].

The Verlet method is based on a fact that the necessary neighbor list changes very slowly in dense flow so that two particles that are close to each other at a given time will stay as close neighbors in next few time steps. When the neighbor list is initialized, first the whole domain is divided into many meshes, of which size is slightly greater than the diameter of the largest particle. Then, the distances between two particles in the same mesh or neighboring meshes are calculated. Two particles will be defined as a close neighbor if the distance between these two particles $\mid \vec{x}_i - \vec{x}_j \mid - R_i - R_j$ is smaller than a predefined constant called 'Verlet distance'. For each particle there is a Verlet list that includes all close neighbors of this particle. The Verlet list is renewed when the travel distance of any particle in the domain exceeds the 'Verlet distance' from the time when last Verlet list was built. A proper value of 'Verlet distance' need to be determined to balance between making Verlet list too large and renewing Verlet list too frequently.

Another factor that can affect computational efficiency is the selection of time-integration schemes. Generally higher order of scheme can guarantee higher accuracy, but cause more computational time. In this research, fourth order Runge-kutta method is chosen to obtain a high degree of accuracy with reasonable computational time.

Finally, the time step is typically chosen based on numerical stability argument that states collision time t between two particles of '1' and '2' calculated by $t = 3.21(m_{eff}/k_n)^{2/5}(v_n)^{-1/5}$ [139], where v_n is pre-collisional relative velocity between the two particles, k_n is normal stiffness and $m_{eff} = m_1 m_2/(m_1 + m_2)$ is the effective mass. The maximum pre-collisional relative velocity will determine minimum collision time t_{min} and the numerical time step in this research will be chosen as $\delta t \leq t_{min}/30$. While increasing this time step is not recommended as it may change the nature of the simulations, one can use soft particles by decreasing k_n to increase δt.

3.3.2 Force model

The general framework for soft sphere force models is as follows: The deformation due to forces between particles is modeled as an effective overlap between the edges of two particles (or one particle and another object like a wall). Then the normal and tangential forces between two particles in contact are calculated using the force models. This force-based model is more capable of simulating intrinsic characteristics of dense flow, where contacts between particles are multiple and enduring.

There are several different force models developed by the pioneering work of Cundall and Strack [140], Walton and Braun [141], Gallas et al. [142] and others. Two common types of soft sphere models are reviewed here, the Walton and Braun model [141] and the general formulation first proposed by Cundall and Strack [140].

Walton and Braun model: The Walton and Braun model is more phenomenological, partly because their force model considers different stages of collisions for normal and tangential forces. Assuming the normal overlap between two particles is δ_n, the normal forces can be calculated by

$$F_N = \begin{cases} K_1\delta_n & \text{for loading} \\ K_2(\delta_n - \delta_{n0}) & \text{for unloading} \end{cases} \tag{3.4}$$

Where, K is the coefficient constant of normal stiffness, and different when particles approach and depart from each other. δ_{n0} is the value of δ_n, when unloading forces go to zero. The coefficient of restitution can be calculated by $e = (K_1/K_2)^{1/2}$.

The tangential forces are history-dependent. At certain time t_1, the tangential forces F_T at next time step is calculated by

$$F_T(t_1 + \Delta t) = F_T(t_1) + K_T \Delta s \tag{3.5}$$

Where Δs is relative surface displacement between two contacting particles at time interval Δt. K_T, the effective tangential stiffness, is not a constant, but depends on how the current state is prepared. When the two particles slide against each other, this sliding motion will increase tangential forces, but when they slide in the same direction, the sliding forces will decrease. All these sliding forces at the same time are limited by Coulomb law. The definition of K_T is

$$K_T = \begin{cases} K_{T0}(\frac{\mu F_N - F_T}{\mu F_N - F_T^*})^\gamma & \text{for slip in one direction} \\ -K_{T0}(\frac{\mu F_N + F_T}{\mu F_N + F_T^*})^\gamma & \text{for slip in the other direction} \end{cases} \tag{3.6}$$

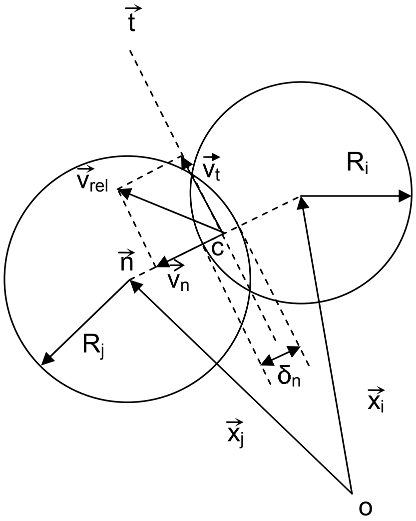

Figure 3.2: A cartoon of contact force model between two particles shows overlap δ_n and relative velocity $\vec{v}_n$ and $\vec{v}_t$ between two contacting particles.

K_{T0} is the initial tangential stiffness, μ is the coefficient of friction, γ is a fixed parameter usually set to 1/3 to agree with Mindlins theory, and F_T^*, which is initially zero, is subsequently set to the value of the total tangential force, F_T, whenever the relative tangential slip reverses directions.

The Walton and Braun model can be used in the dense flow, but there are no mechanistic rules for calculating contact forces that are actually important for modeling the segregation in the dense flows. Therefore, DEM simulation model developed by Cundall and Strack [140] with Hertzian/Mindlin contact theory is used in this research.

Hertzian and Mindlin Model: In the force model of Cundall and Strack, the complex description of the deformation of each pair of contacting particles is replaced with an overlap between the contacting particles in both normal and tangential direction [See Fig. 3.2]:

$$\vec{F}_n = (-k_n \delta_n^{\alpha} - \eta_n \delta_n^{\beta} \vec{v}_n \vec{n})\vec{n} \tag{3.7}$$

$$\vec{F}_t = \min(-k_t \delta_n^{\gamma} \vec{\delta}_t - \eta_t \delta_n^{\lambda} \vec{v}_t, \mu \times \vec{F}_n) \tag{3.8}$$

As shown in Equations (3.7) and (3.8), an elastic repulsive force and a damping force are used in both normal and tangential direction, which are dependent on the overlap and relative velocity between contacting particles. In order to satisfy the coulomb friction law, the tangential force cannot exceed the largest static friction force. $\vec{n}$ is the unit vector in the direction connecting centers of two contact particles. δ_n and $\vec{\delta_t}$ are the overlaps in normal and tangential directions [see Fig. 3.2], and $\vec{v_n}$ and $\vec{v_t}$ are the relative velocities in normal and tangential directions of the contact point (point c in Fig. 3.2). k_n, k_t, η_n and η_t are stiffness and damping coefficients in normal and tangential directions, which are different constants depending on the particle property only. μ is coefficient of friction obtained from experiments.

When the particle positions and velocities of two particles i and j are known, calculations of overlaps in normal direction δ_n and relative velocities in normal and tangential direction of the contact point $\vec{v_n}$ and $\vec{v_t}$ are straightforward as shown in equations (3.9), (3.10), (3.11).

$$\delta_n = R_i + R_j - \mid \vec{x_i} - \vec{x_j} \mid \tag{3.9}$$

$$\vec{v_n} = \vec{v}_{j,n} - \vec{v}_{i,n} \tag{3.10}$$

$$\vec{v_t} = \vec{v}_{j,t} - \vec{v}_{i,t} + \vec{\omega}_j \times \vec{R}_j - \vec{\omega}_i \times \vec{R}_i \tag{3.11}$$

However, to calculate the magnitude of the tangential overlap δ_t, a history of the tangential contact should be recorded from the beginning of a contact at t_0 until particles separate from each other. Then the magnitude of the tangential overlap at certain time t can be calculated by

$$\delta_t = \int_{t_0}^{t} v_t(t')dt' \tag{3.12}$$

The numerical parameters k_n, k_t, η_n and η_t in equations (3.7) and (3.8) must be calculated from physical properties of the materials based on contact theory. From Tsuji et al. [143], These parameters can be calculated by:

$$k_n = \frac{4}{3}\sqrt{R_{eff}}E_{eff} \tag{3.13a}$$

$$k_t = 8\sqrt{R_{eff}}G_{eff} \tag{3.13b}$$

$$\eta_n = 2\sqrt{m_{eff}k_n} \tag{3.13c}$$

$$\eta_t = 2\sqrt{m_{eff}k_t} \tag{3.13d}$$

where R, E, G, m are corresponding to particle radius, Young's modulus, shear modulus, and mass. $R_{eff}, E_{eff}, G_{eff}$ and m_{eff} are corresponding to the effective radius, effective Young's modulus, effective shear modulus, and effective mass of a pair of contacting particles, where $1/R_{eff} = 1/R_1 + 1/R_2$, $1/E_{eff} = (1-\nu_1^2)/E_1 + (1-\nu_2^2)/E_2$, $1/G_{eff} = 2(1+\nu_1)(2-\nu_1)/E_1 + 2(1+\nu_2)(2-\nu_2)/E_2$ and $1/m_{eff} = 1/m_1 + 1/m_2$. Subscript 1 and 2 denote two different particle types and ν is Poison ratio of materials. Radius, mass and shear modulus of the wall are assumed to be infinite for the contact between particle and the wall [143].

There are quite a few different force models based on the different choices of α, β, γ and λ. For example, if $\alpha = 1$ and β, γ and $\lambda = 0$, it is a linear force model. Hertzian theory implies $\alpha = 3/2$ and $\gamma = 1/2$, which were already proved experimentally by Falcon et al. [144]. For the damping forces 1/4, 1/2 and 3/2 were used for β and λ for different granular materials, but there is no general agreement on the choice of β and λ yet. Ji et al. [145] compared the linear force model and nonlinear force models, and they stated that the linear force model can describe nearly elastic collisions well and can be used to study the principle dynamics of granular materials, but the nonlinear force models can be used for the complex material contact or for a more accurate requirement. Detailed comparison of different soft sphere models can be found in Ref. [146] and in the paper by Schafer et al. [139]. In this thesis, nonlinear force model derived by Tsuji et al. [143] is used where $\alpha = 3/2$; $\gamma = 1/2$; $\beta = 1/4$; $\lambda = 1/4$:

$$\vec{F}_n = (-k_n\delta_n^{3/2} - \eta_n\delta_n^{1/4}\vec{v}_n\vec{n})\vec{n} \tag{3.14}$$

$$\vec{F}_t = \min(-k_t\delta_n^{1/2}\vec{\delta}_t - \eta_t\delta_n^{1/4}\vec{v}_t, \mu \times \vec{F}_n) \tag{3.15}$$

Table 3.1: Values of numerical parameters used in the DEM simulations for spherical glass particles for contacts between two particles of sizes as noted.

Parameters	2mm-2mm	3mm-3mm	2mm-3mm
k_n (N/m$^{3/2}$)	1.18×10^9	1.45×10^9	1.30×10^9
k_t (N/m$^{3/2}$)	1.56×10^9	1.91×10^9	1.71×10^9
η_n (N s/m$^{5/4}$)	7.83	15.93	10.19
η_t (N s/m$^{5/4}$)	8.99	18.27	11.68
μ	0.4	0.4	0.4

For all of the simulations described in this thesis, the particles are spheres of diameters (D) 2 and 3 mm. The parameters used to calculate the interparticle forces shown in Equations (3.14) and (3.15) are based on a material with similar properties to glass. The following properties are used: material density ρ_m =2520 kg/m^3; Young's modulus E=76 GPa; Poissons ratio=0.22; the coefficient of restitution e =0.9. The resulting parameters are shown in Table 3.1. To reduce the computational time for most of the systems presented, the materials are softened by reducing the normal stiffness k_n from O[10^9]$N/m^{3/2}$ to O[10^6]$N/m^{3/2}$ as in Refs. [115],[147]. This reduces the time step by a factor of 10. The resulting parameters are shown in Table 3.2. The kinematics were compared in a simple geometry with and without reducing k_n, and good agreement was found in the average kinematics and in the segregation patterns. Based on the method for determining time step δt described in section 3.3.1, the time step $\delta t = 1 \times 10^{-5}$ s for the softer particles and $\delta t = 1 \times 10^{-6}$ s for the harder particles.

To inhibit crystallization, the radii of each size of particle are slightly poly-disperse 10% of the average radii. As shown in equation (3.13), the simulation parameters k_n, k_t, η_n and η_t depend on mass and radii of particles, but these effects are ignored in this research because the mass and radii change very slightly.

3.4 Data processing methods

The output files of simulation at each time step include positions and translational and angular velocities of all particles. It also includes a regular, though typically less frequent, output of the forces. This information can be used to analyze the statistical

Table 3.2: Values of numerical parameters used in the DEM simulations for the softened particles for contacts between two particles of sizes as noted.

Parameters	2mm-2mm	3mm-3mm	2mm-3mm
k_n (N/m$^{3/2}$)	1.57×10^6	1.92×10^6	1.72×10^6
k_t (N/m$^{3/2}$)	2.06×10^6	2.52×10^6	2.26×10^6
η_n (N s/m$^{5/4}$)	2.85×10^{-1}	5.79×10^{-1}	3.70×10^{-1}
η_t (N s/m$^{5/4}$)	3.26×10^{-1}	6.64×10^{-1}	4.24×10^{-1}
μ	0.4	0.4	0.4

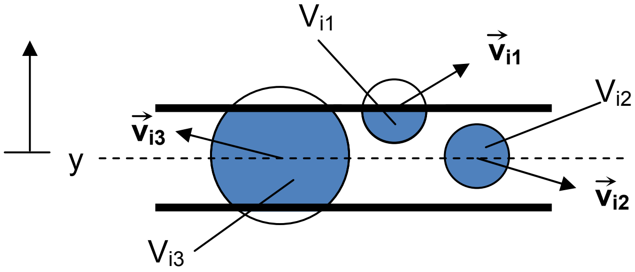

Figure 3.3: A cartoon of a bin to calculate solids volume fraction and average velocity.

properties of particles such as solids volume fraction, average velocity and average velocity fluctuations at different locations of the simulation domains. Sample calculations of these terms are presented assuming uniformity in the x and z directions. In this case, the domain is divided into equal sized bins perpendicular to the y-direction. The calculation of a mass averaged value within a bin centered y includes every particle that is fully or partly in the bin of a chosen width. First, the volumes of the parts of these particles that are in the bin [the shadow areas in Fig. 3.3] are calculated. Then, the average solids volume fraction in this bin for N output files (or during a time interval $\Delta t = (N-1)\delta t$) can be calculated as

$$\overline{f}(y) = \frac{\Sigma_{i=1}^{N} \Sigma_j V_{ij}}{N V_{bin}} \tag{3.16}$$

Where, $\overline{f}(y)$ is time averaged solids volume fraction over Δt at y, the coordinate of the center of this bin. i is the index of output files and j is the index of particles that are partly or fully in this bin. V_{ij} is corresponding solids volume in the bin for particle

j of output file i. V_{bin} is the volume of the bin.

The instantaneous velocity in the output files of simulation can be expressed as $\vec{u}$=$u\vec{x}$+$v\vec{y}$+$w\vec{z}$. Then, the three components of average velocity of the particles in a bin centered at y can be calculated as

$$\overline{u}(y) = \frac{1}{N}\sum_{i=1}^{N}\frac{\Sigma_j u_{ij}V_{ij}}{\Sigma_j V_{ij}} \tag{3.17a}$$

$$\overline{v}(y) = \frac{1}{N}\sum_{i=1}^{N}\frac{\Sigma_j v_{ij}V_{ij}}{\Sigma_j V_{ij}} \tag{3.17b}$$

$$\overline{w}(y) = \frac{1}{N}\sum_{i=1}^{N}\frac{\Sigma_j w_{ij}V_{ij}}{\Sigma_j V_{ij}} \tag{3.17c}$$

where, $\overline{u}(y), \overline{v}(y), \overline{w}(y)$ are time-averaged velocity components over Δt at y and u_{ij}, v_{ij}, w_{ij} are the instantaneous velocity components of particle j of output file i.

The three components of velocity fluctuations are calculated according to $u' = u - \overline{u}, v' = v - \overline{v}, w' = w - \overline{w}$. Then velocity fluctuation correlations are calculated to obtain nine components of velocity fluctuation correlations: $\overline{u'u'}$,$\overline{u'v'}$,$\overline{u'w'}$, $\overline{v'u'}$,$\overline{v'v'}$, $\overline{v'w'}$,$\overline{w'u'}$,$\overline{w'v'}$,$\overline{w'w'}$, where $\overline{u'v'} = \overline{v'u'}$,$\overline{u'w'} = \overline{w'u'}$ and $\overline{v'w'} = \overline{w'v'}$.

$$\overline{u'u'}(y) = \frac{1}{N}\sum_{i=1}^{N}\frac{\Sigma_j (u_{ij} - \overline{u}_i(y))^2 V_{ij}}{\Sigma_j V_{ij}} \tag{3.18a}$$

$$\overline{v'v'}(y) = \frac{1}{N}\sum_{i=1}^{N}\frac{\Sigma_j (v_{ij} - \overline{v}_i(y))^2 V_{ij}}{\Sigma_j V_{ij}} \tag{3.18b}$$

$$\overline{w'w'}(y) = \frac{1}{N}\sum_{i=1}^{N}\frac{\Sigma_j (w_{ij} - \overline{w}_i(y))^2 V_{ij}}{\Sigma_j V_{ij}} \tag{3.18c}$$

$$\overline{u'v'}(y) = \frac{1}{N}\sum_{i=1}^{N}\frac{\Sigma_j (u_{ij} - \overline{u}_i(y))(v_{ij} - \overline{v}_i(y)) V_{ij}}{\Sigma_j V_{ij}} \tag{3.18d}$$

$$\overline{u'w'}(y) = \frac{1}{N}\sum_{i=1}^{N}\frac{\Sigma_j (u_{ij} - \overline{u}_i(y))(w_{ij} - \overline{w}_i(y)) V_{ij}}{\Sigma_j V_{ij}} \tag{3.18e}$$

$$\overline{v'w'}(y) = \frac{1}{N}\sum_{i=1}^{N}\frac{\Sigma_j(v_{ij}-\overline{v}_i(y))(w_{ij}-\overline{w}_i(y))V_{ij}}{\Sigma_j V_{ij}} \tag{3.18f}$$

Where, $\overline{u}_i(y), \overline{v}_i(y), \overline{w}_i(y)$ are averaged velocity components at y for the output files of i. The kinematic granular temperature then can be calculated:

$$T(y) = \frac{(\overline{u'u'}(y) + \overline{v'v'}(y) + \overline{w'w'}(y))}{3} \tag{3.19}$$

For binary mixtures of species 1 and 2, the volume fraction, velocity, and velocity fluctuation correlations and granular temperature of each component can be calculated according to the method above. Then these kinematic properties for the mixture are calculated according to:

$$\overline{f}_{mix}(y) = \overline{f}_1(y) + \overline{f}_2(y) \tag{3.20}$$

$$\overline{q}_{mix}(y) = \frac{\overline{q}_1(y)\overline{f}_1(y) + \overline{q}_2(y)\overline{f}_2(y)}{\overline{f}_{mix}(y)} \tag{3.21}$$

where, q refers to either the velocity components u, v, w, or velocity fluctuation correlations $u'u', u'v', u'w', v'v', v'w', w'w'$, or granular temperature T.

The average relative fluxes of each component i can be calculated as the following:

$$\overline{f}_i\Delta\overline{u}_i(y) = \overline{f}_i(\overline{u}_i(y) - \overline{u}_{mix}(y)) \tag{3.22a}$$

$$\overline{f}_i\Delta\overline{v}_i(y) = \overline{f}_i(\overline{v}_i(y) - \overline{v}_{mix}(y)) \tag{3.22b}$$

$$\overline{f}_i\Delta\overline{w}_i(y) = \overline{f}_i(\overline{w}_i(y) - \overline{w}_{mix}(y)) \tag{3.22c}$$

To understand and model the segregation in dense flow, the flow dynamics such as internal stresses, or ‘microscopic’ structures such as coordination numbers also need to be measured and analyzed. The details for obtaining these parameters will be reviewed in detail in the relevant chapters.

Chapter 4

Simulations in a split-bottom cell

In this chapter, the Discrete Element Method (DEM) is used with a soft sphere model to simulate the segregation of different sized particles in the split-bottom cell with and without curvature effects. The results are used to understand the driving mechanisms for the horizontal segregation in the bulk observed in the experiments in Chapter 2.

4.1 Simulation setup

For the simulations described in this chapter, computational experiments are performed in two geometries illustrated in Figs. 4.1 (a) and (b) . The first, a circular split-bottom cell [Fig. 4.1 (a)] is similar to the experiments described in Chapter 2, but with two differences. The first difference from the experimental cell is that for the simulation cell, only a sector of the circular split-bottom cell is simulated; the boundaries are periodic in the azimuthal direction, which means particles leaving one boundary in azimuthal direction will enter the other boundary in this direction with same velocities $\vec{u}=u_i\vec{\theta}+v_i\vec{r}+w_i\vec{z}$. The second difference from the experimental cell is that an inner cylindrical wall is used to reduce computational cost and to prevent a singularity problem in the center of cylinder. In the full 3D case, there is a solid-like region in the model, so if the radius of this inner wall is small enough, its presence should not effect the dynamics [see e.g. Fig. 2.1(c)]. Fenistein and van Hecke have tested this experimentally [129] and shown it to be the case. For the simulations reported here, the outer radius R_o and the radius of the split R_s are the same as those in the experiments: R_s=121 mm

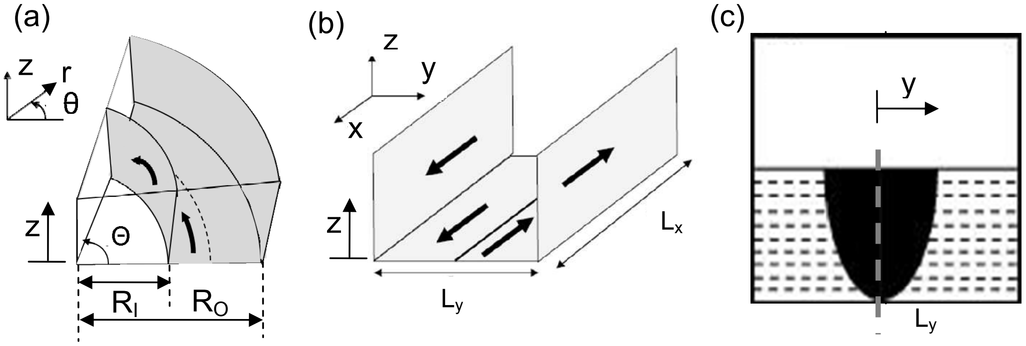

Figure 4.1: Sketches of the setup for the simulations. (a) Circular split-bottom cell. (b) Parallel split-bottom cell. (c) Sketch of a cross section of a typical computational experiment in the parallel cell. The shear zone is indicated by the darkened region. Copyright (2010) by the American Physical Society.

and R_o =145 mm. The selection of the boundary parameters of inner radius R_i will be described in section 4.2.1.

The second geometry simulated is a parallel split-bottom cell [Fig. 4.1 (b)], similar to that of Ries et al. [148]. In this setup, the bottom of an open rectangular box is split at the center. The side and bottom walls move in opposite directions, each at V_s=0.01 m/s along the split. Periodic boundaries are applied in the shear direction. While the shear band is in many ways similar to that in the circular split-bottom cell, the shear band in the parallel split-bottom cell is symmetric and the center of the shear band at all depths is located at the center plane of the cell as Fig. 4.1 (c). Using this in conjunction with the circular split-bottom cell allows us to investigate the effect of curvature on segregation. Several trial runs were performed where the width L_y and length L_x were varied to ensure that system size effects are eliminated. Based on the results from these trial runs and those described in Ref. [148], dimensions of $L_y = 50$ mm and $L_x = 21$ mm were used.

In both the circular and parallel split-bottom cells, a layer of small particles is glued to the bottom, as in the physical experiment, to control boundary friction. Both cells are filled to a height $H = 30$ mm. To save computational cost the shear rates are increased from that of the experiments. In the circular cell, two different angular velocities of inner walls Ω are used for two different boundaries described in section 4.2.1. In the parallel cell, the two halves of the cell move in opposite direction to one another at a relative speed of 0.02 m/s. Results from a few computational experiments performed at different shear velocities indicate that inertial effects are unimportant and therefore that the shear rates do not effect the results. The exception is the segregation rate, which increases equally for all systems. For the circular cell, the particles are softened according to the numerical parameters in Table 3.2 to increase time step $\delta t = 1 \times 10^{-5}$ s, while for the parallel cell, hard sphere particles are used similar to that of quartz [Table 3.1] and time step $\delta t = 1 \times 10^{-6}$ s. For the circular cell, the velocity components are denoted using $\vec{u}$=$u_i\vec{\theta}$+ $v_i\vec{r}$+$w_i\vec{z}$, and for the parallel cell, the velocity components are denoted using $\vec{u}$=$u_i\vec{x}$+$v_i\vec{y}$+$w_i\vec{z}$, both according to the directions noted in Fig. 4.1.

The initial conditions of each simulation are obtained by the following procedures: A well-mixed binary mixture is dropped into the split-bottom cell under gravity and when all particles settle down, the side walls start to shear the granular mixtures. The simulations are stopped after the segregation reach steady state determined when the local solids fraction of each species becomes stable. The profiles of kinematics are measured in vertical and horizontal slices at different time intervals as will be described. Before the results are described, some of the kinematics for two different circular cells are discussed as they apply to the determination of appropriate boundary conditions for these simulations.

4.2 Simulation results

4.2.1 Circular split-bottom cell

Kinematics and segregation patterns in two different circular cells

For this research, two sets of boundary conditions are chosen to investigate the system size effect: (1) a smaller cell, where $R_i = 95$ mm, with a rotation speed $\Omega = 0.15$ rad/s and a total number of 3180 particles, running for 400 s; (2) a larger cell, where $R_i = 60$ mm, with a rotation speed $\Omega = 0.5$ rad/s and a total number of 7544 particles, running for 250 s.

In Figure 4.2, profiles of the kinematics of mixtures at steady state in the radial direction are plotted for both cells at different heights z. These profiles include the stream-wise velocity $\overline{u}$, the local angular velocity $\overline{\omega}$, the local shear rate $|\overline{\dot{\gamma}}|$ and the

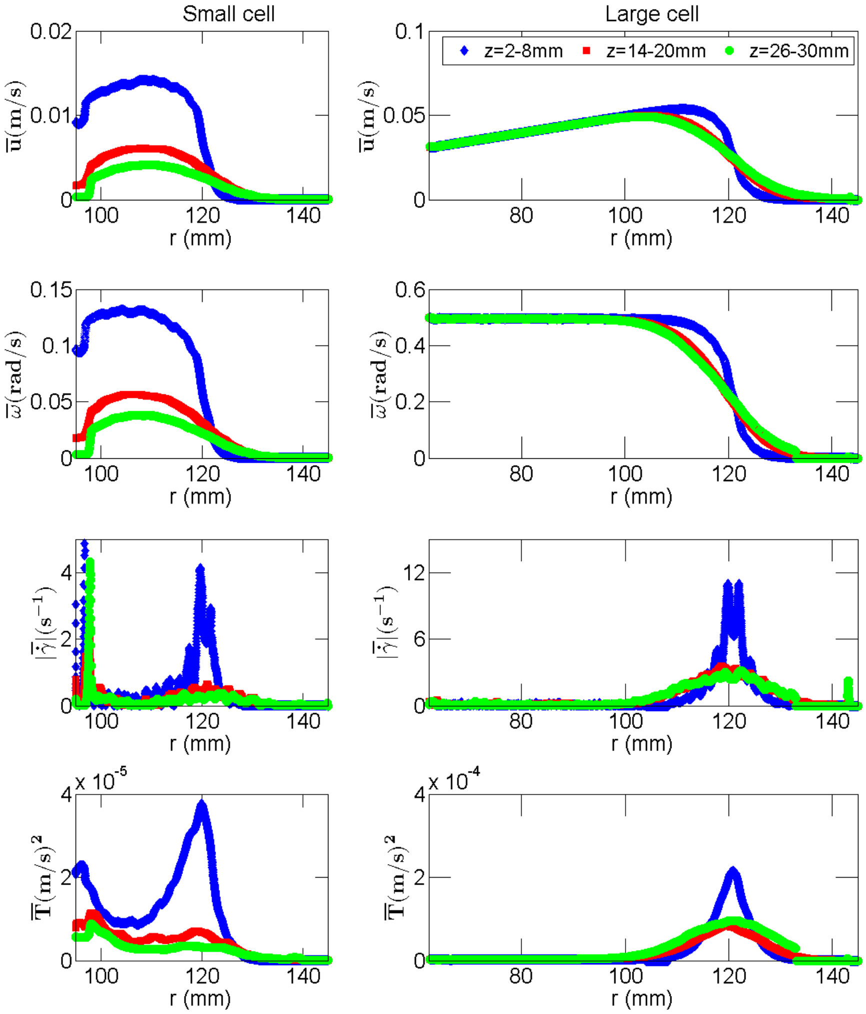

Figure 4.2: Profiles of kinematics of mixtures in r direction at three different height z for the smaller cell (first column) at $t = 390 - 400$ s and the larger cell (second column) at $t = 240 - 250$ s. From the first row to the fourth row, there are profiles of streamwise velocity $\overline{u}$, angular velocity $\overline{\varpi}$, absolute value of shear rate $|\overline{\dot{\gamma}}|$, and granular temperature $\overline{T}$.

granular temperature $\overline{T}$ (Here and henceforth, $\overline{q}_i$ represents a temporal and local spatial average of quantity q). From these plots, the influence of inner wall on the flow kinematics is apparent for the smaller cell. Although in this cell, the radial position of the inner wall is still located in the solid-like region, it is too close to the shear band so

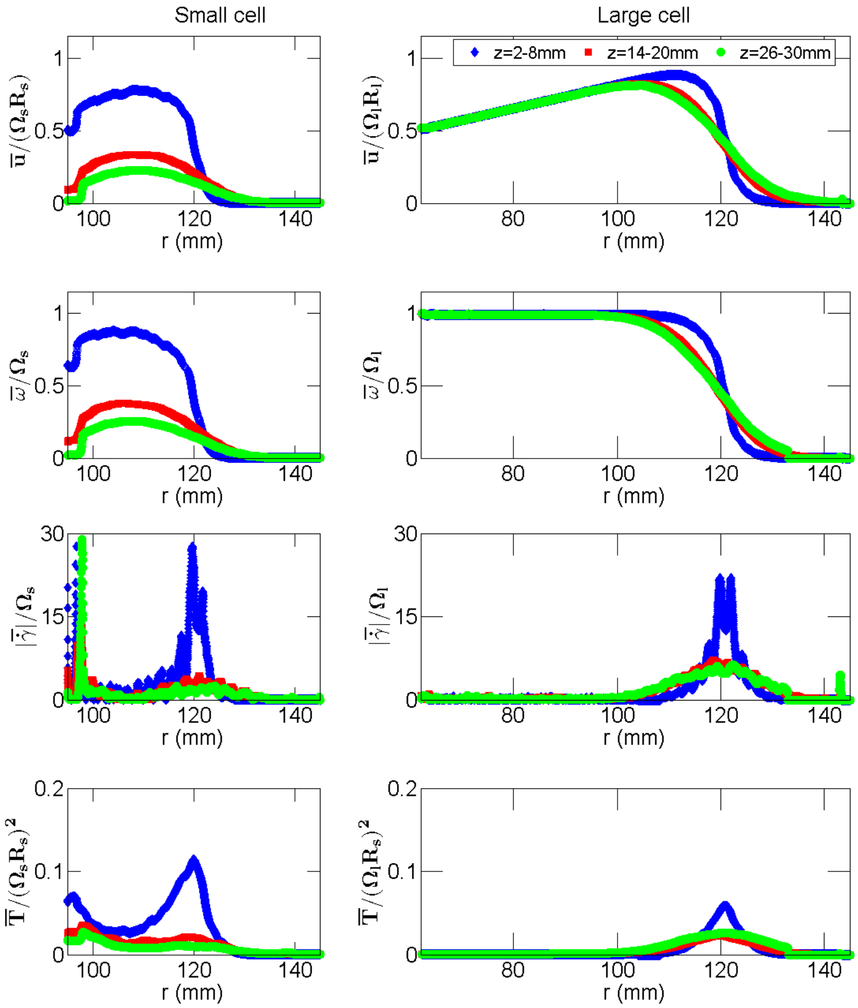

Figure 4.3: Profiles of *normalized* kinematics of mixtures in r direction at three different height z for the smaller cell (first column) at $t = 390 - 400$ s and the larger cell (second column) at $t = 240 - 250$ s. From the first row to the fourth row, there are profiles of streamwise velocity $\overline{u}/(\Omega R_s)$, angular velocity $\overline{\omega}/\Omega$, absolute value of shear rate $|\overline{\dot{\gamma}}/\Omega|$, and granular temperature $\overline{T}/(\Omega R_s)^2$. The rotation speed $\Omega = 0.15$ rad/s for the smaller cell and $\Omega = 0.50$ rad/s the larger cell

that the existence of inner wall cause a second peak of shear rate and granular temperature and a non-linear velocity profile out of shear zone. The slip near the inner wall is also very serious, especially for values of z not exactly adjacent to the bottom. In contrast, in the larger cell, the kinematics in the shear band are isolated from the inner

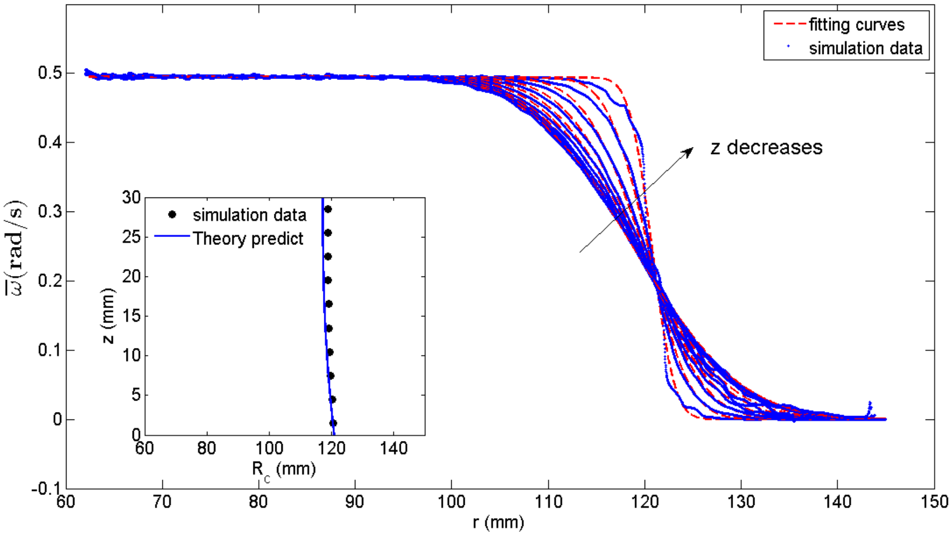

Figure 4.4: From the larger cell: Profiles of the angular velocity $\overline{\omega}$ in radial direction at different heights z from 1.5 mm to 28.5 mm at $t = 240 - 250$ s are fit by Equation (2.1): $\omega/\Omega = 1/2 - 1/2\mathrm{erf}[(r - R_c)/W]$ (dotted lines). Inset: Points present the fitting parameter R_c as function of z and the solid line is the fitting curve by Equation (2.2): $z = H - R_c[1 - R_s/R_c(1 - (H/R_s)^{2.5})]^{0.4}$.

wall, with the highest granular temperature and shear rate close to center of shear zone, and the profiles of velocities are close to those found experimentally in this thesis and those predicted from other references such as [115, 132]. Fig. 4.3 shows the normalized kinematic properties corresponding to Fig. 4.2. From these plots it is apparent that the changing of the rotation speed for the circular cells has very weak impact on the kinematics in the circular split-bottom cell. In Figure 4.4 the profiles of $\overline{\omega} = d\overline{u}/dr$ from the larger cell are plotted and fit by Equation (2.1) ($\omega/\Omega = 1/2 - 1/2\mathrm{erf}[(r - R_c)/W]$) at several heights z from 1.5 mm to 28.5 mm. The fitting parameters R_c, the center of shear band at z, as a function of z are plotted in the inset of Figure 4.4 to compare with theoretical prediction in Equation (2.2) ($z = H - R_c[1 - R_s/R_c(1 - (H/R_s)^{2.5})]^{0.4}$), which match very well. All of these indicate the inner radius of the larger cell is small enough to reproduce the kinematics of bulk flow.

Segregation patterns from the small and large cell are shown in Figure 4.5 and Figure 4.6, respectively. These figures show snapshots of segregation patterns at the

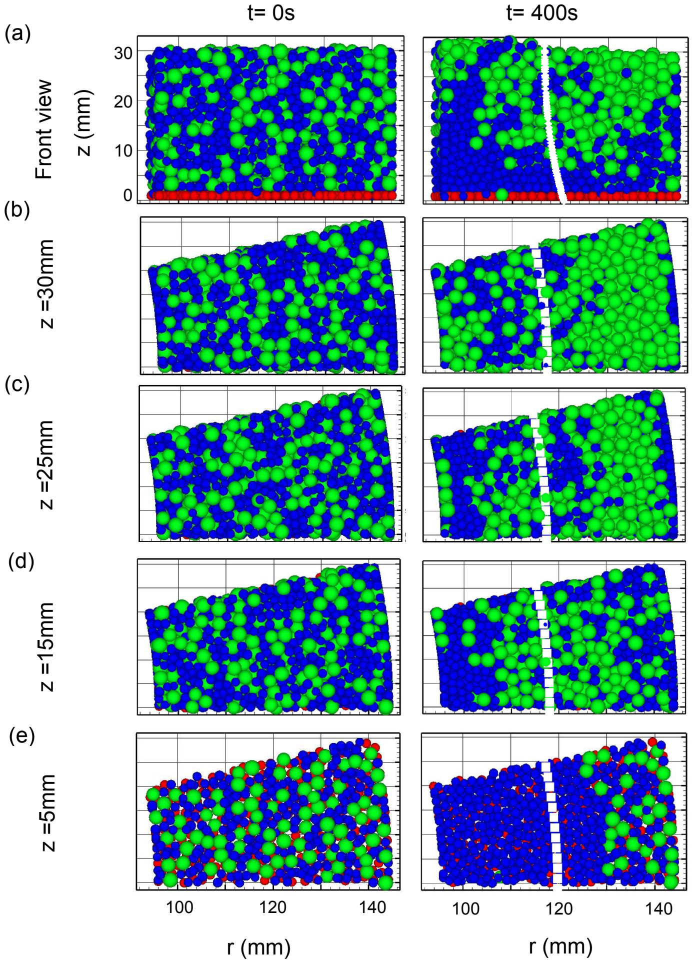

Figure 4.5: Vertical and horizontal cross sections from computational experiments using 2 mm (Blue) and 3 mm (Green) particles in the *small* cell. First column: the beginning of the computational experiment when the particles are well-mixed at $t = 0$ s. Second column: after $t = 400$ s of rotation of the base. (a) Vertical cross section at $\theta = 0$. (b)-(e) Horizontal cross sections at heights indicated. The dashed lines indicate the theoretical centers of shear zone, as calculated by Equation (2.2). The total filling height H is 30 mm with a glued layer of 2 mm glass particles (Red) at the bottom. Copyright (2010) by the American Physical Society.

beginning (first 10 seconds) and end (last 10 seconds) of the computational experiments. One vertical plane and several horizontal planes at different heights z are shown. One can see that segregation patterns similar to the experiments emerge in both small and

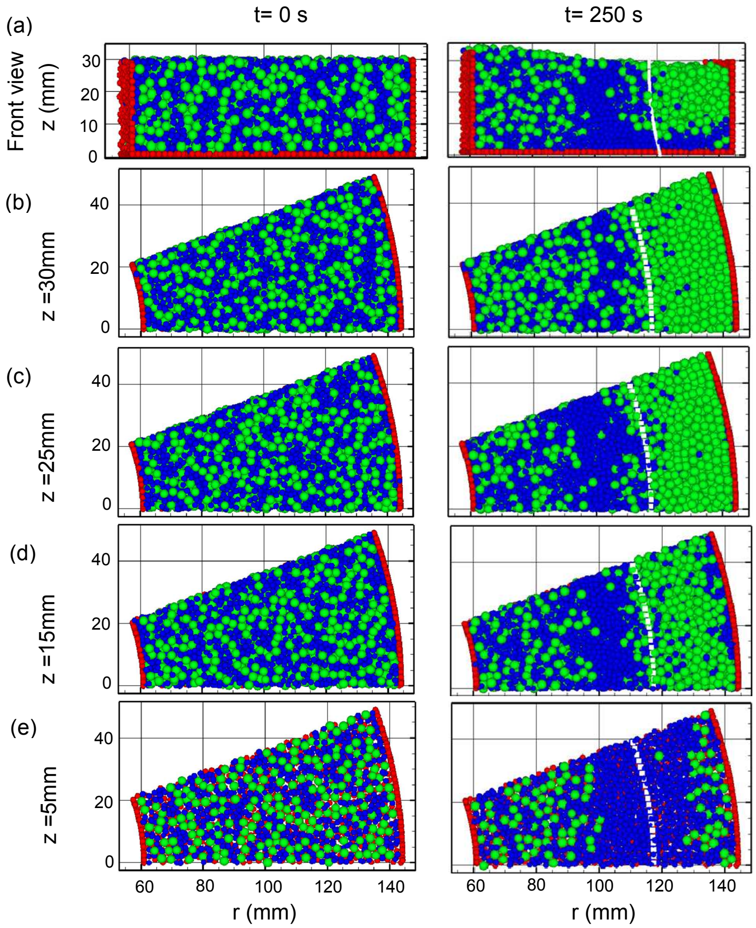

Figure 4.6: Vertical and horizontal cross sections from computational experiments using 2 mm (Blue) and 3 mm (Green) particles in the *large* cell. First column: the beginning of the computational experiment when the particles are well-mixed at $t = 0$ s. Second column: after $t = 250$ s of rotation of the base. (a) Vertical cross section at $\theta = 0$. (b)-(e) Horizontal cross sections at heights indicated. The dashed lines indicate the theoretical centers of shear zone, as calculated by Equation (2.2). The total filling height H is 30 mm with a glued layer of 2 mm glass particles (Red) at the bottom.

large cells, albeit over a significantly quicker time frame. Large particles segregate to the top and away from the bottom. Away from either surface, horizontal segregation patterns emerge, where small particles accumulate at smaller radii, and larger particles accumulate at larger radii. The dashed lines indicate the centers of shear zone calculated using Equation (2.2). Similar to the experimental results, the smaller particles become highly concentrated at smaller radii, the larger particles become concentrated at larger radii, and a mixed phase exists at the largest radii and smallest radii. For the smaller cell, unlike the experiments, the center of the shear zone R_c (dashed lines in the figure) does not separate the zones of high and low concentrations of large particles, though the larger particles seem most highly concentrated at $r = R_c$. In contrast, in the larger cell, the horizontal shells of large and small particles are well separated by the center of shear band, with a slight diffusive mixing at the interface. These results indicate that if R_i is too large, it disturbs the shear band and subsequently influence segregation patterns. On the other hand, the large cell with small inner boundary appears to reproduce the segregation pattern seen in the experiments well. The following sections will focus on the results from the large cell, since it more accurately simulates the kinematic details of the experimental split-bottom cell without inner boundaries.

Segregation kinematics

To study the kinematics that drive the horizontal segregation, particularly shown in Figs. 4.6 (c) and (d), a horizontal slice is used between $z = 14$ and 20 mm where the most striking horizontal segregation pattern emerges. In Fig. 4.7, some of the relevant kinematics for the species in that slice are plotted as a function of radial position r during the first 10 seconds (left column) and last 10 seconds (right column) of the simulation.

Figure 4.7(a) shows the profiles of solid volume fraction $\overline{f}_i$, where the subscript i represents the particle type or phase: small particles only ($i = s$), large particles only ($i = l$), and the mixed phase ($i = \text{mix}$). One can see from these plots that the concentrations apparent by eye in the snapshots in Fig. 4.6 are well-represented by these plots. At the beginning of simulation, $\overline{f}_i$ is constant across the cell indicating a good mixture. At the end of the simulation, $\overline{f}_s$ is high in the inner part of shear zone indicating there is a high concentration of small particles in this region, and $\overline{f}_l$ is high in the outer part of shear zone indicating there is a high concentration of large particles in the part of shear zone close to outer wall. There are mixed regions immediately adjacent to the inner and outer walls. After the system has been rotated for some time, there is a subtle dip in the average solids fraction $\overline{f}_{mix}$, similar to that associated with the dilatancy reported in Ref. [116]. Figure 4.7(b) shows the profiles of the stream-wise velocities $\overline{u}_i$ for each species, which shows that the stream-wise velocities $\overline{u}_i$ of all species are essentially same during the whole course of simulations.

Figures 4.7 (c) and (d) show the profiles of the relative fluxes in the radial and vertical directions: $\overline{f}_i\Delta\overline{v}_i = \overline{f}_i(\overline{v}_i - \overline{v}_{mix})$ and $\overline{f}_i\Delta\overline{w}_i = \overline{f}_i(\overline{w}_i - \overline{w}_{mix})$, respectively. The radial fluxes are notably small and noisy for both small and large particles at the beginning and end of the computational experiment. This indicates there is little or no segregation flux parallel to the shear gradient driving the horizontal segregation pattern. In contrast, the vertical segregation fluxes $\overline{f}_i\Delta\overline{w}_i$ are prominent and consistent. The flux of large particles is upward relative to the mixture and the flux of the small particles is downward. The flux within the shear band decreases but not as much by the end of the experiment, the reason of which will be explained later in this chapter. Figure 4.7(e) shows the averaged profile of the kinematic granular temperature $\overline{T}_i$, essentially the velocity variances of the system as defined in equation (3.19). For all positions, the kinematic temperature of the smaller particles is greater than that of the large, previously explained for dense granular systems in Ref. [84].

Temporal evolution of segregation

To investigate the temporal evolution of the solids fraction and fluxes for the whole simulation, these quantities throughout the entire experiment are calculated and averaged in the radial direction (as well as the z- and θ-directions) over five-second intervals. For quantity q these averages over intervals in time and all three spatial dimensions are denoted by $\langle\overline{q}\rangle$. For layers close to free surface ($z = 24-30$ mm) and bottom ($z = 2-8$ mm) where there appears to be no horizontal segregation structure, these quantities are averaged over the entire layer (from $r = R_i$ to R_o). To capture the horizontal segregation in the bulk, the middle layer ($z = 14-20$ mm) is divided into two parts according to the boundary between the two segregated shells of large and small particles, indicated in Fig. 4.7 (a) as $r = r^* \approx 110$ mm. Then two sets of averages are calculated in this layer, one from $r = R_i$ to r^*, and the other from $r = r^*$ to R_o. Fig. 4.8 shows the results of these calculations for $\langle\overline{f}_i\rangle$ (first column) , $\langle\overline{f}_s\Delta\overline{v}_s\rangle$ and $\langle\overline{f}_s\Delta\overline{w}_s\rangle$ (second column).

The first row shows the data averaged over the top 6 mm of the particles. Figure 4.8 (a) shows that, as expected from observations, the concentration of large particles at the top increases over the course of the experiment, and the concentration of small

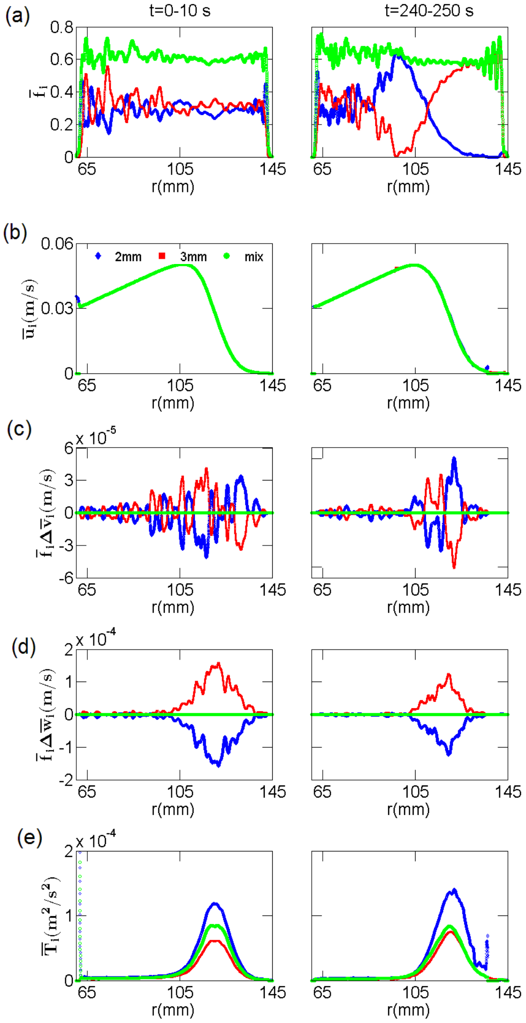

Figure 4.7: Kinematics from the computational experiments in the larger cell with $R_i = 60$ mm pictured in Fig. 4.6. Results are shown are from a horizontal slice of the material between $z = 14$ mm to 20 mm (approximately halfway between the bottom and the top of the mixture). The kinematics shown are averaged over the first and last ten seconds of the computational experiment: $t = 0 - 10$ s (first column), $t = 240 - 250$ s (second column). The data are averaged in the θ- and z- directions for each value of r. (a) Solid volume fraction $\overline{f}_i$ (b) Streamwise velocity $\overline{u}_i$. (c) Relative flux of particles in the radial direction $\overline{f}_i \Delta \overline{v}_i$. (d) Relative flux of particles in the vertical direction $\overline{f}_i \Delta \overline{w}_i$. (e) Kinematic granular temperature $\overline{T}_i$.

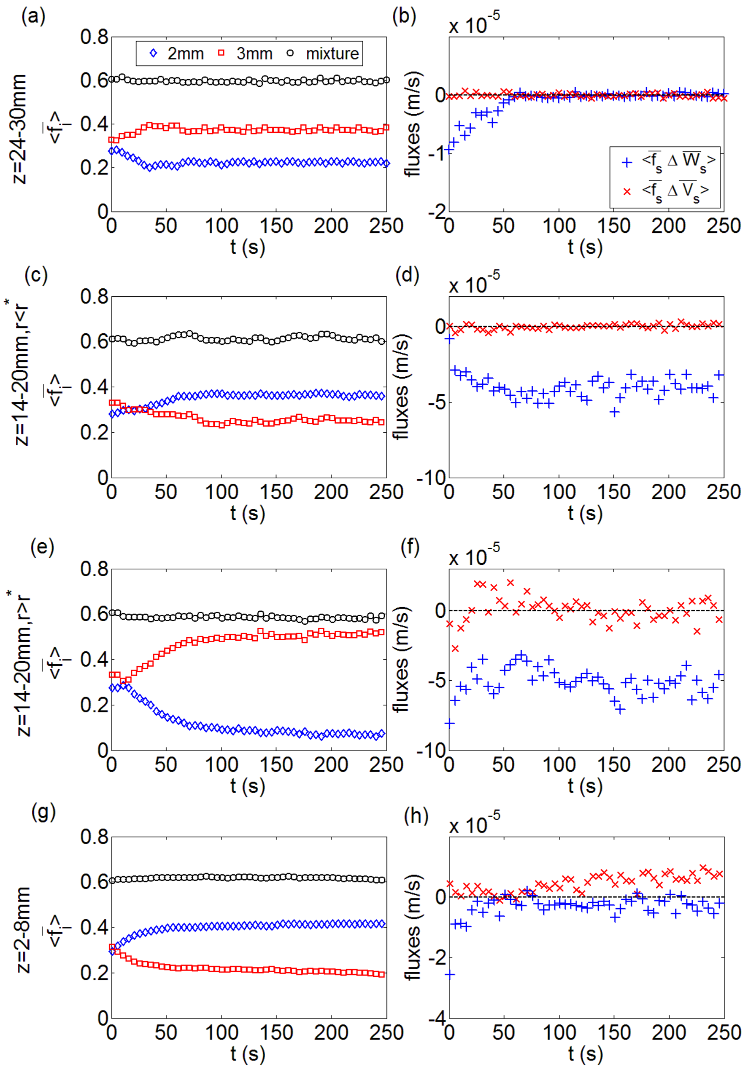

Figure 4.8: Temporal evolution of the averaged solids fraction and the segregation fluxes at different heights z for larger cell with $R_i = 60$ mm. The first column shows the averaged solid fraction $\langle \overline{f}_i \rangle$. The second column shows averaged vertical $\langle \overline{f}_s \Delta \overline{w}_s \rangle$ and radial $\langle \overline{f}_s \Delta \overline{v}_s \rangle$ segregation fluxes for the 2 mm particles. For the top and bottom 6 mm (shown in the first and last row, respectively), the results are averaged over the entire layer. For the middle layer, the results are averaged over the smaller radii (r_1, r_2) =(R_i, r^*) in (c) and (d) and the results are averaged over the larger radii (r_1, r_2)=(r^*, R_o) in (e) and (f). r^*= 110 mm.

particles decreases. The plots of the fluxes of the small particles in Fig. 4.8(b) show the small particles are moving down relative to the mixture and there is no net relative horizontal flux in this layer.

The second row contains data from the inner part ($R_i < r \leq r^*$) of the horizontal slice in the middle of the cell ($z = 14{-}20$ mm), where the concentration of small particles becomes relatively high [Fig. 4.7(a)]. The concentration of small particles in this region grows and saturates, and that of the large particles decreases and saturates [Fig. 4.8(c)]. Somewhat surprisingly in light of the existence of a horizontal concentration gradient, the horizontal flux remains essentially zero during the entire simulation [Fig. 4.8(d)]. The third row contains the data for the outer part ($r^* \leq r < R_o$) of the horizontal slice in the middle of the cell ($z = 14 - 20$ mm), where the concentration of small particles is relatively low [Fig. 4.8(e)]. In this region, too, the horizontal flux remains essentially zero. Compared with average horizontal fluxes, the vertical flux is nonzero in both regions and remains roughly even, though the segregation concentrations seem to stabilize [Fig. 4.8(f)].

The last row shows the data averaged over the bottom 6 mm of the cell. The plots of $\langle \overline{f}_i \rangle$ show that, as expected from observations, the concentration of small particles increases and saturates over the course of the experiment, and the concentration of large particles decreases [Fig. 4.8(g)]. The plots of $\langle \overline{f}_s \Delta \overline{v}_s \rangle$ and $\langle \overline{f}_s \Delta \overline{w}_s \rangle$ show the small particles are moving down slightly relative to the mixture, but only at the very beginning of the experiment, and that there is a slightly positive horizontal flux in this layer [Fig. 4.8(h)].

To summarize these results, both vertical and horizontal segregation patterns are observed in the concentration profiles and in the evolution of the concentration over time. There is a clear vertical (downward) flux of the smaller particles relative to the large until the particles are segregated associated with the vertical segregation pattern. The vertical segregation fluxes persists within the middle layers over the entire course of the experiment [Fig. 4.8 (d) and (f)]. In contrast, there is no clear radial flux of one species relative to the other corresponding to the horizontal concentration segregation pattern in the middle layers.

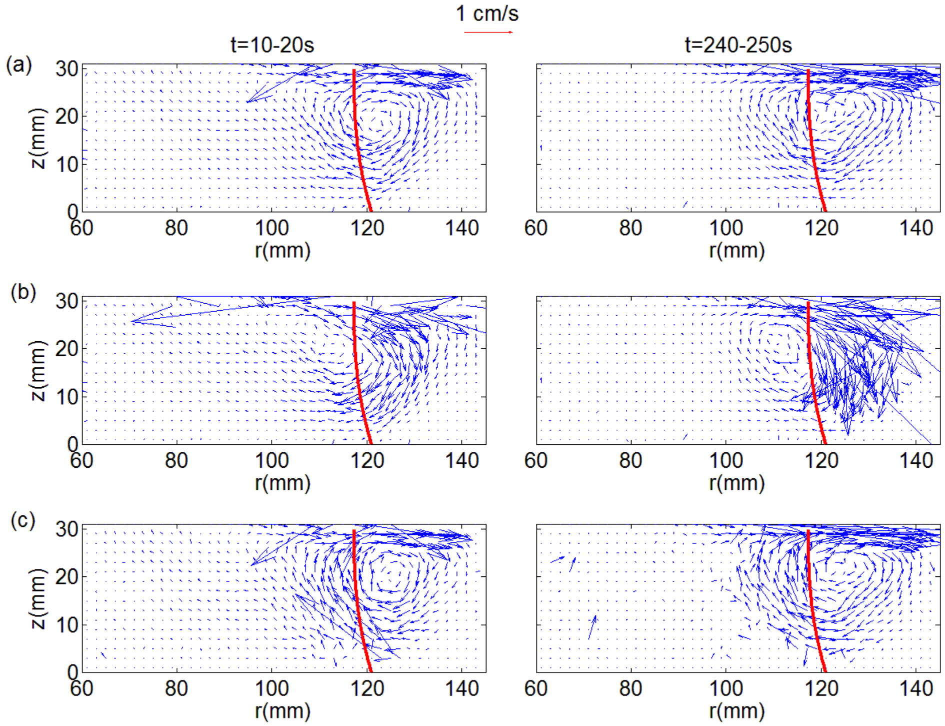

Figure 4.9: Velocity vectors in a vertical plane perpendicular to the stream-wise direction, averaged in the stream-wise direction for the larger circular cell with $R_i = 60$ mm between two different time intervals: $t = 10 - 20$ s and $t = 240 - 250$ s. Different rows for different species (a) Results for the mixture. (b) Results for the 2 mm particles. (c) Results for the 3 mm particles. The red lines indicate the theoretical centers of shear zone, as calculated by Equation (2.2).

Velocity fields

In lieu of a noticeable horizontal flux driving the horizontal segregation pattern in the circular cell, a second possible 'driving force' for the horizontal segregation patterns becomes clear in plots of the velocity vectors in a vertical plane as in Fig. 4.9. In these plots, one can see a stable vertical convection roll exists in the system. This convective roll persists during the entire duration of the simulation. The convective roll carries all particles upward at the inner part of the shear band, outward at the top surface, downward at the outer part of the shear band, and inward at the bottom of the cell. The lines superposed on the figures show that R_c (calculated using Equation (2.2)) cuts

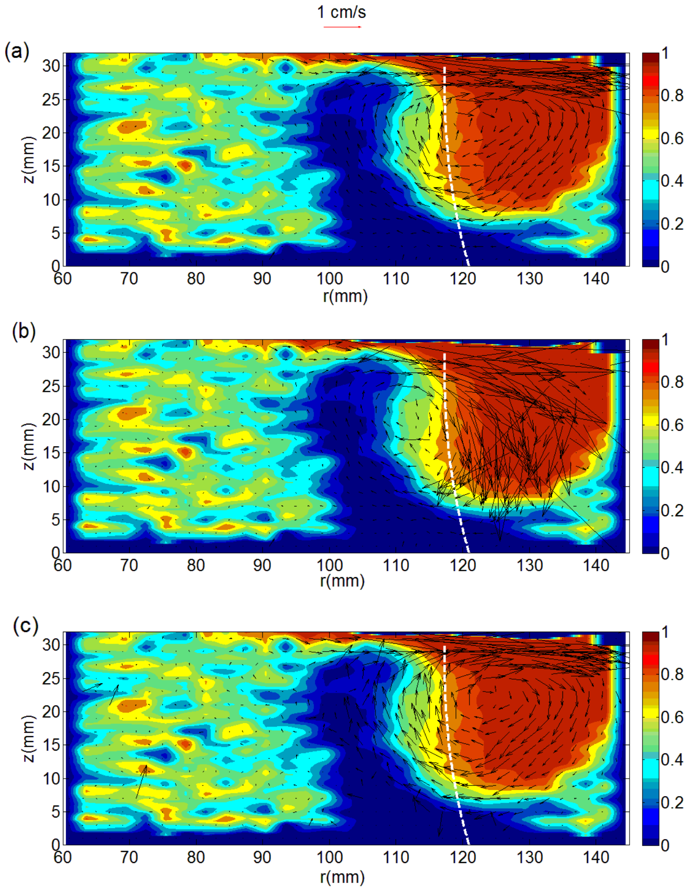

Figure 4.10: Velocity vector superposed on the concentration map of large particles at $t = 240 - 250$ s for the larger circular cell. (a) Results for the mixture. (b) Results for the 2 mm particles. (c) Results for the 3 mm particles. The white dotted lines indicate the theoretical predictions for centers of shear zone, as calculated by Equation (2.2).

nearly through the middle of the convection roll. This convection roll superposed with the relative vertical flux of the particles appears to be responsible for the horizontal segregation pattern.

The process that leads to the horizontal segregation pattern appears to be as follows. Wherever large and small particles coexist in the bulk, the large particles rise and the small particles sink. The net rotation of the system causes the large particles segregated at the top to be advected downward along the outside edge of the cell and the small particles segregated at the bottom to be advected upward along the inside edge of the cell. In this way, the large and small particle appear horizontally segregated in the bulk. Particles in these neighboring disparate regions then mix horizontally due to ordinary diffusion in the shear band. In Figure 4.10, it clearly shows the contours of concentration of large particles match the velocity vector fields at end of simulations well, where small particles accumulate the upward region of convection roll at smaller radii in the bulk, while large particles accumulate the downward region of convection roll at larger radii in the bulk. A mixed region in the middle leads to a vertical segregation flux in the shear zone that persists over the duration of the experiment (as in Fig. 4.7 (d) or Fig. 4.8(d) and (f)).

The convection roll appears to be driven by the circular motion of the particles in the circular cell. This is supported by the results from the parallel cell, as discussed in the next section.

4.2.2 Parallel split-bottom cell

Kinematics and velocity fields

Much of the kinematics in the parallel split-bottom cell at steady state ($t = 190 - 200$ s) as shown in Fig. 4.11 is similar to these in the circular split-bottom cell. In particular, the velocity exhibits 'S' shape profiles [Fig. 4.11(a)], similar to those in Ref. [148]. The shear rate and granular temperature are highest at same locations, the middle plane of the parallel cell in y direction. Different from the circular cell, the shear zone of parallel cell is symmetric to the middle plane in y direction.

The velocity vectors for the parallel split-bottom cell are plotted in Fig. 4.12. In contrast to the results from the computational experiments in the circular split-bottom cell, there is no apparent vertical global convection roll in the parallel cell. This is independent of the time over which the results are averaged (for the results shown in Fig. 4.12, the results were averaged over 10 s at two different time stages $t = 20 - 30$ s and $t = 190 - 200$ s). While some local convection is apparent over short periods as also observed in mono-sized systems by Ries et al. [148], there do not appear to be any long-lasting velocity or vorticity trends in this system. This supports the conjecture that the convection roll observed in the circular split cell is due to the curvature and rotation effects. Without the convection roll it is easier to investigate the effects of the

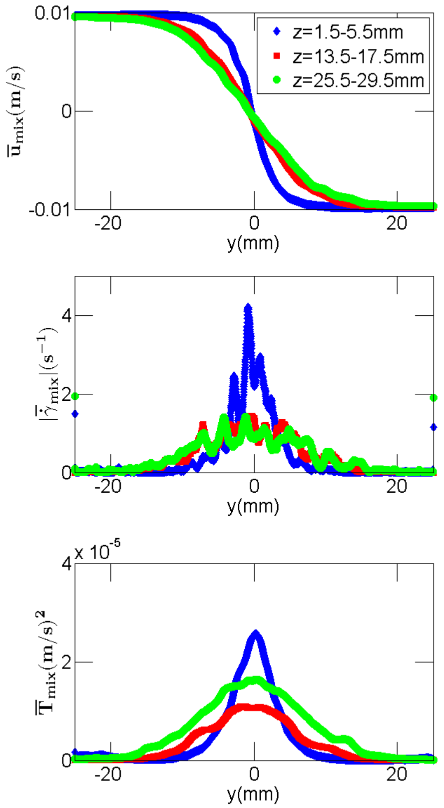

Figure 4.11: Profiles of kinematic parameters of mixtures including velocity $\overline{u}$, absolute value of shear rate $|\bar{\dot{\gamma}}| = |d\overline{u}/dy|$ and granular temperature $\overline{T}$ averaged at $t = 190 - 200$ s at three different heights z as indicated in the plots.

shear gradient.

Segregation kinematics

Figure 4.13 contains snapshots of segregation patterns at the beginning ($t = 0$ s), middle ($t = 60$ s), and end ($t = 200$ s) of the computational experiment in the parallel cell. Results from a vertical plane and several horizontal planes at different heights z are shown at each of these time steps. As in the cylindrical cell, vertical segregation occurs quickly, where large particles accumulate close to the free surface and small particles accumulate close to the bottom. Additionally, a slow horizontal segregation pattern can be also observed in the bulk. At $t = 60$ s, at approximately $2/3H$ large particles begin

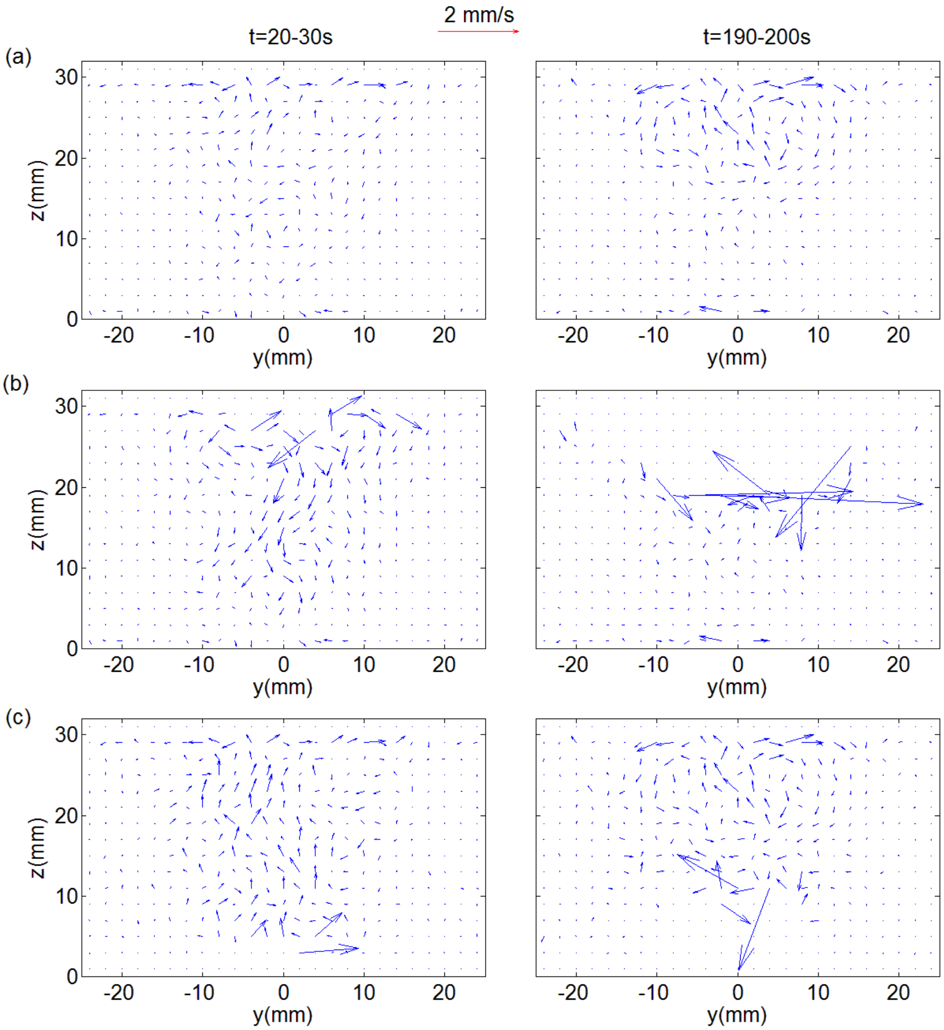

Figure 4.12: Velocity vectors in a vertical plane perpendicular to the stream-wise direction, averaged in the stream-wise direction for parallel cell between two different time intervals: $t = 20 - 30$ s and $t = 190 - 200$ s. Different rows for different species (a) Results for the mixture. (b) Results for the 2 mm particles. (c) Results for the 3 mm particles.

to accumulate in the center of shear zone, while small particles accumulate at edges of shear zone. The horizontal segregation patterns become more clear by $t = 200$ s.

In order to investigate this horizontal segregation pattern more quantitatively, data

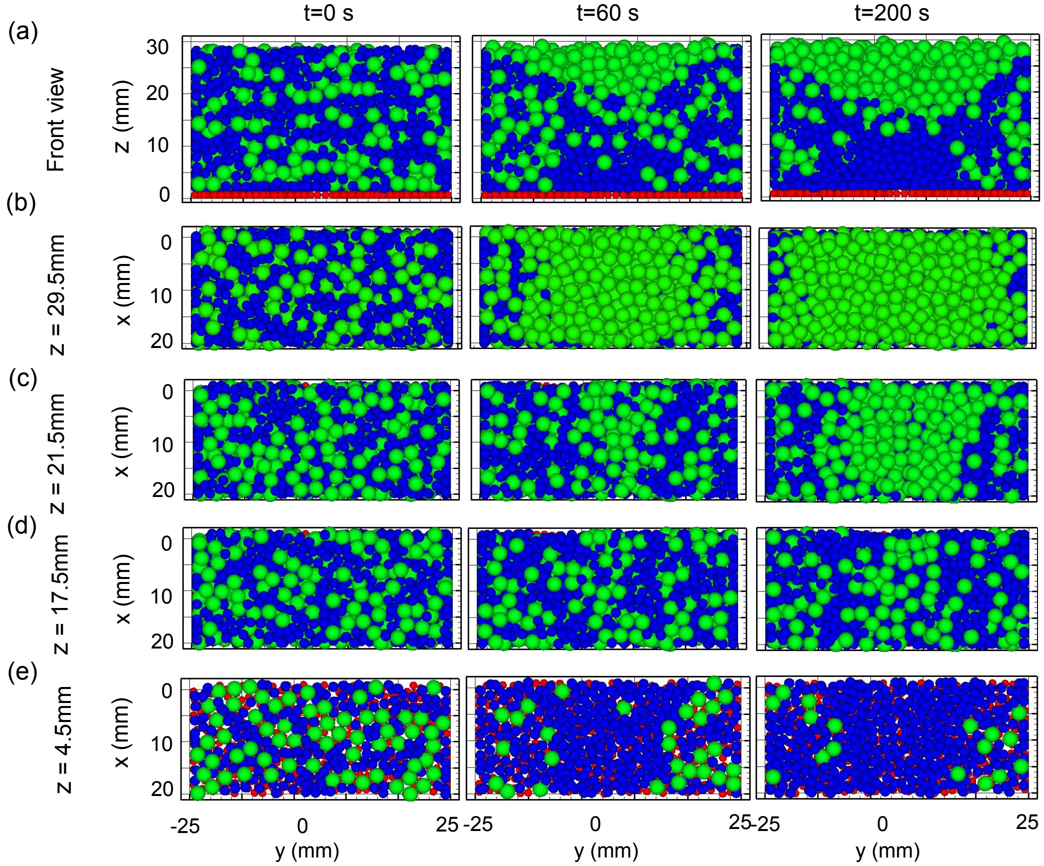

Figure 4.13: Front and top views from computational experiments in the parallel cell with 2 mm (Blue) and 3 mm (Green) particles at the beginning of the computational experiment when the particles are well-mixed at $t = 0$ s (first column) after $t = 60$ s (second column) and after $t = 200$ s (third column). (a) Vertical cross section at $x = 0$. (b)-(e) Horizontal cross sections at heights indicated. The total filling height H is 30 mm, with a glued layer of 1.5 mm glass particles (Red) at the bottom. Copyright (2010) by the American Physical Society.

is processed within three different horizontal slices: the bottom layers at $z = 1.5 - 5.5$ mm, the middle layers at $z = 13.5 - 17.5$ mm and the surface layers at $z = 25.5 - 29.5$ mm. In Figs. 4.14-4.16 the profiles of $\overline{f}_i$, $\overline{u}_i$, absolute value of shear rate of mixture $|\bar{\dot{\gamma}}_{mix}|$, $\overline{f}_i\Delta\overline{v}_i$, $\overline{f}_i\Delta\overline{w}_i$ and kinematic temperature $\overline{T}_i$ are plotted as a function of y for these different slices using same method as described for the circular cell.

The plots for $\overline{f}_i$ in Fig. 4.14(a), Fig. 4.15(a) and 4.16 (a) show that the well-mixed

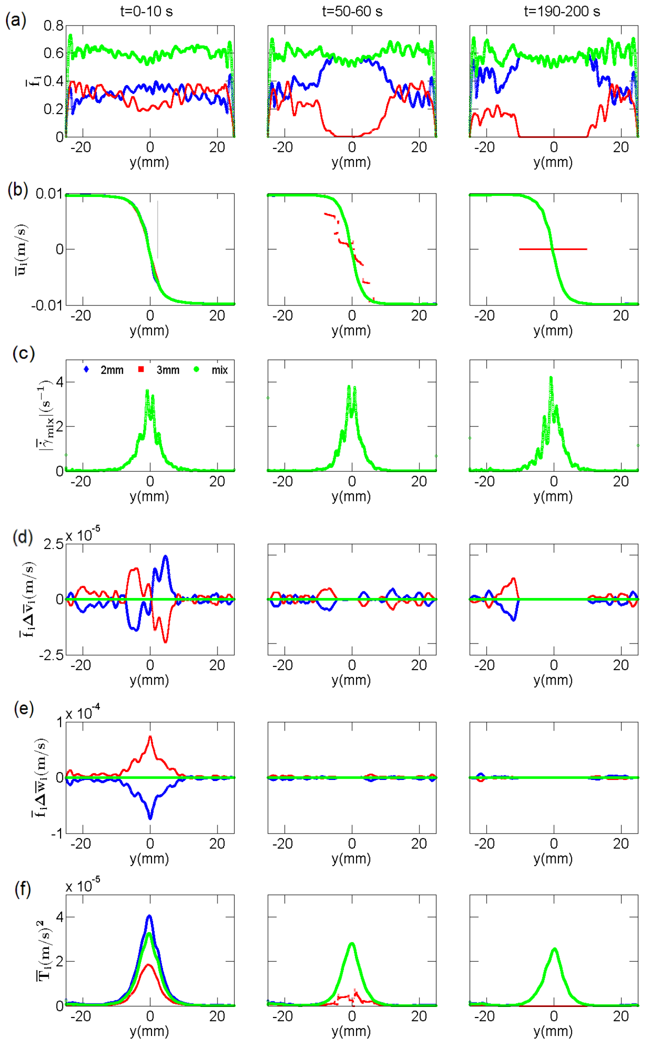

Figure 4.14: Kinematics from the computational experiments in the parallel cell pictured in Fig. 4.13. Results shown are for a horizontal slice of the material between $z = 1.5$ mm to 5.5 mm (layers close to the very bottom) and averaged in the x- and z- directions for each value of y. The kinematics are averaged over ten seconds at three different times during the simulation: $t = 0 - 10$ s (first column), $t = 50 - 60$ s (second column) $t = 190 - 200$ s (third column). (a) Solid volume fraction $\overline{f}_i$. (b) Streamwise velocity $\overline{u}_i$. (c) Absolute value of shear rate of mixture $|\bar{\dot{\gamma}}_{mix}| = |d\overline{u}_{mix}/dy|$. (d) Relative flux of particles in the y-direction $\overline{f}_i\Delta\overline{v}_i$. (e) Relative flux of particles in the vertical direction $\overline{f}_i\Delta\overline{w}_i$. (f) Kinematic granular temperature $\overline{T}_i$.

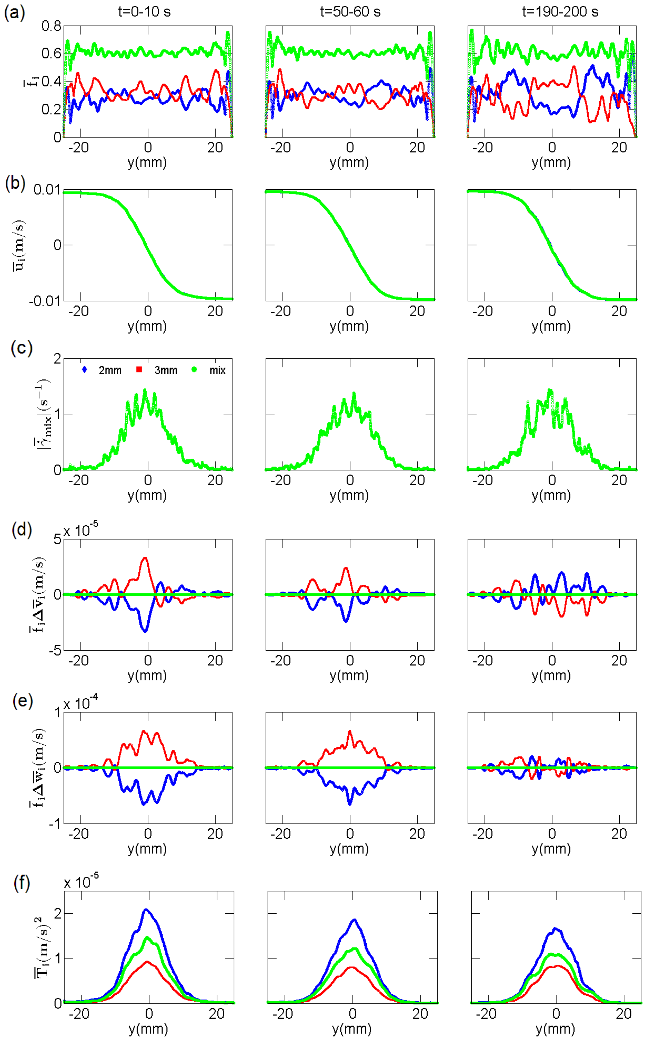

Figure 4.15: Similar plots as Fig. 4.14 for a horizontal slice of the material between $z = 13.5$ mm to 17.5 mm (approximately halfway between the bottom and the top of the system) and averaged in the x- and z- directions for each value of y. Copyright (2010) by the American Physical Society.

system of particles at $t = 0$ s evolves to quite segregated in the horizontal direction in the middle layers [Fig. 4.15(a)] and in the vertical direction in the bottom and surface layers [Fig. 4.14(a) and Fig. 4.16(a)] by $t = 200$ s. That is, in the middle layers, the region of high concentration of large particles is centered on the point of highest shear rate, while small particles are concentrated at the outer edges of the shear zone. In the

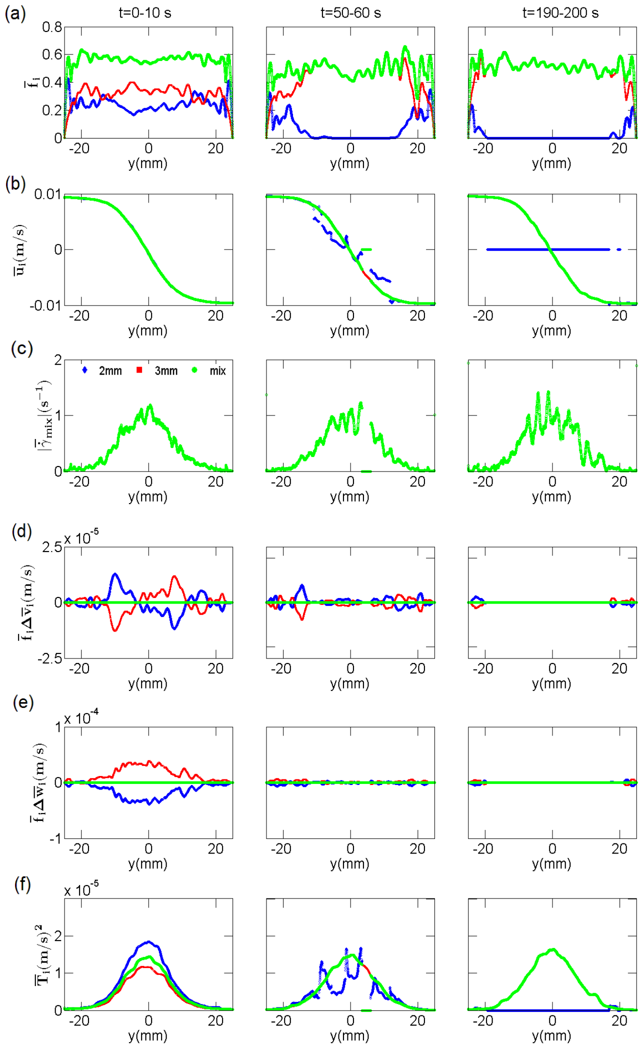

Figure 4.16: Similar plots as Fig. 4.14 for a horizontal slice of the material between $z = 25.5$ mm to 29.5 mm (layers close to the free surface) and averaged in the x- and z- directions for each value of y.

bottom and surface layers, small particles sink to the bottom and large particles rise to the surface.

The plots for the stream-wise velocities $\overline{u}_i$ [Figs. 4.14 - 4.16 (b)] again show the characteristic error function seen in these systems, essentially the same for all particles and at all times. In this case, the highest shear rate is in the center of the cell as in Figs. 4.14-4.16 (c). In contrast with those for the circular shear cell, the plots for $\overline{f}_i \Delta \overline{v}_i$ [Fig. 4.14-4.15 (d)] show a subtle trend of horizontal flux of the large particles into the shear zone at the beginning of the experiment which decays by $t = 200$ s at the bottom and middle layers. An opposite flux of small particles into the shear zone at surface layers [Fig. 4.16(d)] can be observed, probably due to the lower solids fraction close to free surface, a hypothesis that is investigated in section 4.3. The plots for $\overline{f}_i \Delta \overline{w}_i$ [Figs. 4.14-4.16 (e)] show a more dramatic segregation effect in the vertical direction, approximately twice the flux in the horizontal direction. This, too, dies down significantly after 200s. $\overline{T}_i$ is biggest where the shear rate is the greatest and small particles always have higher kinematic temperature than that of the large particles as in the circular cell [Figs. 4.14-4.16(f)].

Time evolution of segregation

To investigate the evolution of the segregation kinematics over time, as for the circular cell, the averaged solid fraction and relative fluxes are plotted as a function of time for the parallel cell as was done for the circular cell. For the horizontal flux the symmetry in the problem is used and the difference between the flux on the left of the cell and that on the right side of the cell is calculated: $\langle \overline{f}_s \Delta \overline{v}_s \rangle = \langle \overline{f}_s \Delta \overline{v}_s \rangle_{y<0} - \langle \overline{f}_s \Delta \overline{v}_s \rangle_{y>0}$. By this definition, a positive value of $\langle \overline{f}_s \Delta \overline{v}_s \rangle$ indicates the small particles are moving to the region of highest shear rate in the center of shear zone. These quantities are calculated for the central 40 mm of the cell and plotted in Fig. 4.17. The first row shows the data averaged over the top 4 mm of the system of particles; the second row shows the data averaged over the middle 4 mm, and the third row shows the data averaged measured the bottom 4 mm, just above the particles fixed to the base.

The plots of $\langle \overline{f}_i \rangle$ show that, as expected from observations, the concentration of large particles increase near the top of the cell over the course of the experiment, and the concentration of small particles increase near the bottom [Figs. 4.17(a) and (e)]. The plots of the vertical fluxes of the small particles $\langle \overline{f}_s \Delta \overline{w}_s \rangle$ show the small particles are moving down relative to the mixture throughout the system. This trend is short-lived at the top (which quickly becomes depleted of small particles) and at the bottom (which quickly becomes depleted of large particles) [Figs. 4.17(b) and (f)]. The trend is longer lasting in the middle until the remainder of the small particles move from

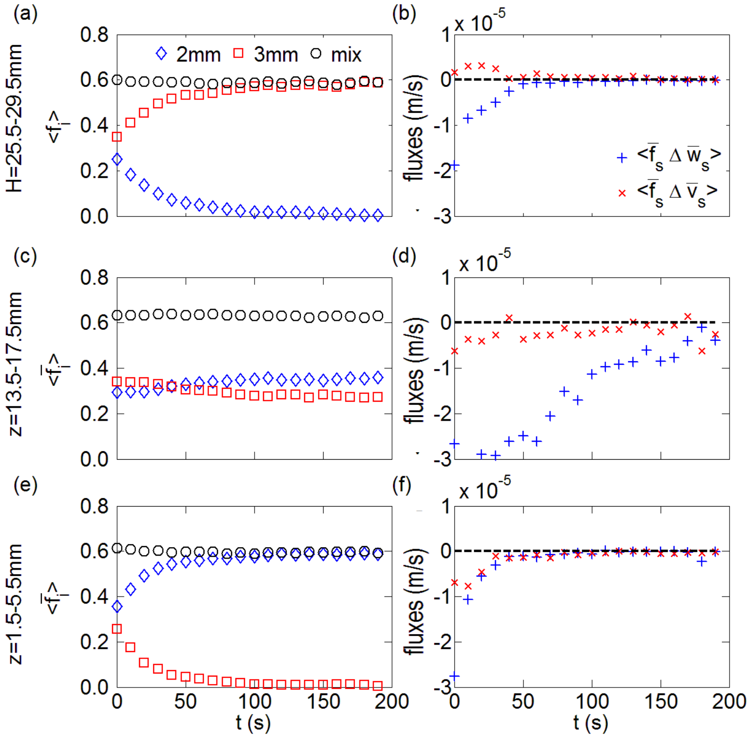

Figure 4.17: Temporal evolution of the averaged solids fraction and the segregation fluxes at different heights z. The first column shows the averaged solid fraction $\langle \overline{f}_i \rangle$. The second column shows averaged vertical $\langle \overline{f}_s \Delta \overline{w}_s \rangle$ and transverse $\langle \overline{f}_s \Delta \overline{v}_s \rangle$ segregation fluxes for the 2 mm particles. $\langle \overline{f}_i \rangle$ and $\langle \overline{f}_s \Delta \overline{w}_s \rangle$ are averaged over the entire layer. $\langle \overline{f}_s \Delta \overline{v}_s \rangle = \langle \overline{f}_s \Delta \overline{v}_s \rangle_{y<0} - \langle \overline{f}_s \Delta \overline{v}_s \rangle_{y>0}$. Copyright (2010) by the American Physical Society.

top to bottom, and the remainder of the large particle move from bottom to top [Fig. 4.17(d)]. The horizontal fluxes $\langle \overline{f}_s \Delta \overline{v}_s \rangle$ are an order of magnitude smaller than the vertical fluxes, yet there is a consistent trend. Throughout the bulk, until segregation is complete, $\langle \overline{f}_s \Delta \overline{v}_s \rangle < 0$, indicating the flux of the small particles is on average away from the region of high shear [Figs. 4.17(d) and (f)]. At the very top surface the trend appears to be slightly reversed, possibly due to the lower solids fraction in this region [Fig. 4.17(b)].

While there is no component of gravity in this horizontal direction, there are a number of other possible driving forces that could give rise to this segregation flux including gradients in the shear rate, the granular temperature, and the solids fractions, and associated pressure gradients. Kinetic theory has the capacity to account the effects of all of these. Predictions from the adaptations of kinetic theory closest to those of the system reported here (e.g., particles are allowed to be dissipative), are not consistent with the measurements of small amounts of segregation flux reported here. Still, kinetic theory and the form give insight to driving forces in granular mixtures so this analysis is included in the subsequent section.

4.3 Kinetic theory prediction and discussion

In this section, kinetic theory is considered for its ability to predict the segregation velocity between two species in the parallel cell where horizontal segregation fluxes are observed in simulations. First, the derivation of segregation velocities in terms of materials properties and flow properties will be presented. Then theoretical prediction will be compared with simulation results.

4.3.1 Derivation of segregation velocity according to kinetic theory

To compare the computational results with those predicted by kinetic theory, the model derived from kinetic theory described in Ref. [79] is used which allows the particles to be slightly dissipative and allows for the non-equipartition of temperature between the species. The effects of non-equipartition of temperature (e.g., Refs. [67], [149], and [150]) according to expressions in [79] are included (similar to those in Ref. [67]).

The granular temperature used here is what might be considered a *dynamic* granular temperature compared with the temperature plotted in Figs.4.14-4.16 (f):

$$T_{Di} = m_i T_i = \frac{m_i(\overline{u'u'} + \overline{v'v'} + \overline{w'w'})_i}{3}. \tag{4.1}$$

The *kinetic pressure* for each species P_i, which is distinct from the hydrostatic pressure and is derived from considerations within the framework of kinetic theory and continuity of momentum for the two species as shown by Refs. [67, 79] accounting for the non-equipartition of granular temperature is calculated by

$$P_i = n_i(T_{Di} + \Delta T_{Di}) + \sum_{k=1}^{2} K_{ik}[T_{Di} + \frac{m_i \Delta T_{Dk} + m_k \Delta T_{Di}}{m_i + m_k}] \tag{4.2}$$

where $n_i = f_i/(4\pi r_i^3/3)$ is the local number density of species i, which is the ratio of solid volume fraction f_i divided by volume of individual particle. m_i and r_i is the mass and radius of species i, and ΔT_{Di} is the difference between the local dynamic temperature of species i and that of the mixture $\Delta T_{Di} = T_{Di} - T_{Dmix}$. K_{ik} is a coefficient concerning the local frequency of interaction between species i and k defined by

$$K_{ik} = \frac{\pi}{3} g_{ik} r_{ik}^3 n_i n_k (1+e), \tag{4.3}$$

where e is the coefficient of restitution, which is 0.9 as in the simulations reported here and g_{ik} is the radial distribution function between contacting pairs

$$g_{ik} = 1/(1-f) + 6 r_i r_k / r_{ik} \times \xi/(1-f)^2 + 8 r_i r_k / r_{ik}^2 \times \xi^2/(1-f)^3 \tag{4.4}$$

Here $r_{ik} = r_i + r_k$, and $\xi = 2\pi(n_1 r_1^2 + n_2 r_2^2)/3$, where '1' and '2' denote two different species.

A similar method is used to derive the diffusion velocity between two species as described in Ref. [79] by starting from conservation of momentum of each species with ignoring inertia,

$$\nabla P_i = -n_i m_i g + \phi_i \tag{4.5}$$

Here, ϕ_i is the momentum source resulting from collisions between unlike particles first developed by Jenkins and Mancini [18] by considering binary collisions and conservation of momentum during the collision of two unlike particles, expressed as:

$$\phi_i = K_{ik} T_D [\frac{m_k - m_i}{m_k + m_i} \nabla \ln T_D + \nabla \frac{n_i}{n_k} + \frac{4}{r_i + r_k} (\frac{2 m_i m_k}{\pi (m_i + m_k) T_D})^{1/2} (v_k - v_i)] \tag{4.6}$$

where $i \neq k$ and v_i an v_k are velocities of species i and k in segregation direction. By definition, $\phi_i = -\phi_k$. Then upon dividing the momentum balance of each species by bulk density $\rho_i = m_i n_i$ and subtracting one from the other, the weighted difference of momentum balances are obtained:

$$0 = -\nabla(P_i) \frac{\rho_k}{\rho_i + \rho_k} + \nabla(P_k) \frac{\rho_i}{\rho_i + \rho_k} + \phi_i \tag{4.7}$$

With a new variable $R_P = \frac{p_i n_k}{p_k n_i}$ and with expression of $\nabla(P_i)$ from equation (4.5), the following equation can be obtained:

$$\nabla P_k = P_k \nabla(\ln \frac{n_k}{n_i}) - \frac{m_i n_k g}{R_P} + \frac{n_k}{n_i}\frac{\phi_i}{R_P} - P_k \nabla(\ln R_P) \tag{4.8}$$

By substituting ∇P_i from equation (4.5) and equation (4.8) into equation (4.7), the equation for diffusion velocity between i and k can be obtained:

$$\begin{aligned} \frac{R_P^{-1} n_k + n_i}{n_i} K_{ik} T_D [\frac{m_k - m_i}{m_k + m_i} \nabla(\ln T_D) + \nabla(\ln \frac{n_i}{n_k}) + \\ \frac{4}{r_i + r_k}(\frac{2 m_i m_k}{\pi(m_i + m_k) T_D})^{1/2}(v_k - v_i)] = P_k \nabla(\ln \frac{P_i}{P_k}) + (m_i - R_P m_k)\frac{n_k g}{R_P} \end{aligned} \tag{4.9}$$

To make this equation more explicit, an arrangement is made as the following:

$$\begin{aligned} \frac{4K_{ik}}{r_i + r_k}(\frac{2 m_i m_k}{\pi(m_i + m_k) T_D})^{1/2}(v_k - v_i) = \\ \frac{P_k \nabla(\ln \frac{P_i}{P_k}) + (m_i - R_P m_k)\frac{n_k g}{R_P}}{(R_P^{-1} n_k + n_i) T_D / n_i} - K_{ik} \frac{m_k - m_i}{m_k + m_i} \nabla(\ln T_D) + K_{ik} \nabla(\ln \frac{n_i}{n_k}) \end{aligned} \tag{4.10}$$

Upon substituting definition of R_P and with some manipulations of the equation on right hand side, the following expression for diffusion velocity $v_i - v_k$ between species i and k is obtained:

$$v_i - v_k = -\frac{(n_i + n_k)^2}{n_i n_k} D_{ik} d_i \tag{4.11}$$

Here, D_{ik} is local coefficient of diffusion defined as:

$$D_{ik} = \frac{n_i n_k}{n_i + n_k} \frac{r_i + r_k}{K_{ik}} \left(\frac{\pi(m_i + m_k) T_D}{32 m_i m_k} \right)^{1/2} \tag{4.12}$$

Finally, d_i (sometimes called a “diffusion force” [19]) represents competing segregation and mixing factors leading to the the difference in diffusion velocities between the two types of particles: $v_i - v_k$. Similar to Ref. [67] d_i is expressed in terms of three components:

$$d_i = d_P + d_T + d_n \tag{4.13}$$

where the segregation and mixing factors related to granular pressure, temperature, and ordinary diffusion are represented by d_P, d_T, and d_n, respectively. Specifically:

$$d_P = \frac{\frac{P_k}{P_i}\nabla P_i - \nabla P_k}{nT_D\left(\frac{P_k}{P_i}+1\right)} \tag{4.14a}$$

$$d_T = -\frac{K_{ik}}{nT_D}\frac{m_k - m_i}{m_k + m_i}\nabla T_D \tag{4.14b}$$

$$d_n = -\frac{K_{ik}}{n}\left[\frac{\nabla n_i}{n_i} - \frac{\nabla n_k}{n_k}\right] \tag{4.14c}$$

In each case ∇q refers to the gradient of q, the physical quantity of interest (P,T and n). Positive values of each represent interactions leading to a net motion of the small particles in the negative y-direction based on equation (4.11) to (4.14). From those equations of diffusion velocity between two species, one can find the segregation velocity only depend on profiles of granular temperature T_D, the profiles of species' number densities n and particle properties such as particle radius r, mass m and coefficient of restitution e.

4.3.2 Comparison between kinetic theory and simulations

In this section, the kinetic theory prediction for segregation velocity between two species in parallel split-bottom cell in horizontal direction by using equation (4.11) to (4.14) will be used to compare with simulation results. To calculate $v_s - v_l$, the segregation velocity between small and large particles, profiles of granular temperature and number fraction are needed and can be measured directly from simulations as given parameters for theoretical prediction.

Profiles of T_{Di} and P_i are plotted for both species at three different heights z of the parallel cell in Fig. 4.18 at $t = 0 - 10$ s. From these figures, it is clear that the larger particles have a greater dynamic granular temperature than the smaller particles for all positions in the cell, and for both types of particles the granular temperature is largest in the middle of the cell, consistent with Ref. [84]. The pressure for each species is dependent on the locations. At the free surface pressure of large particles is higher than that of smaller particles [Fig. 4.18(b)], while pressure of large particles is lower

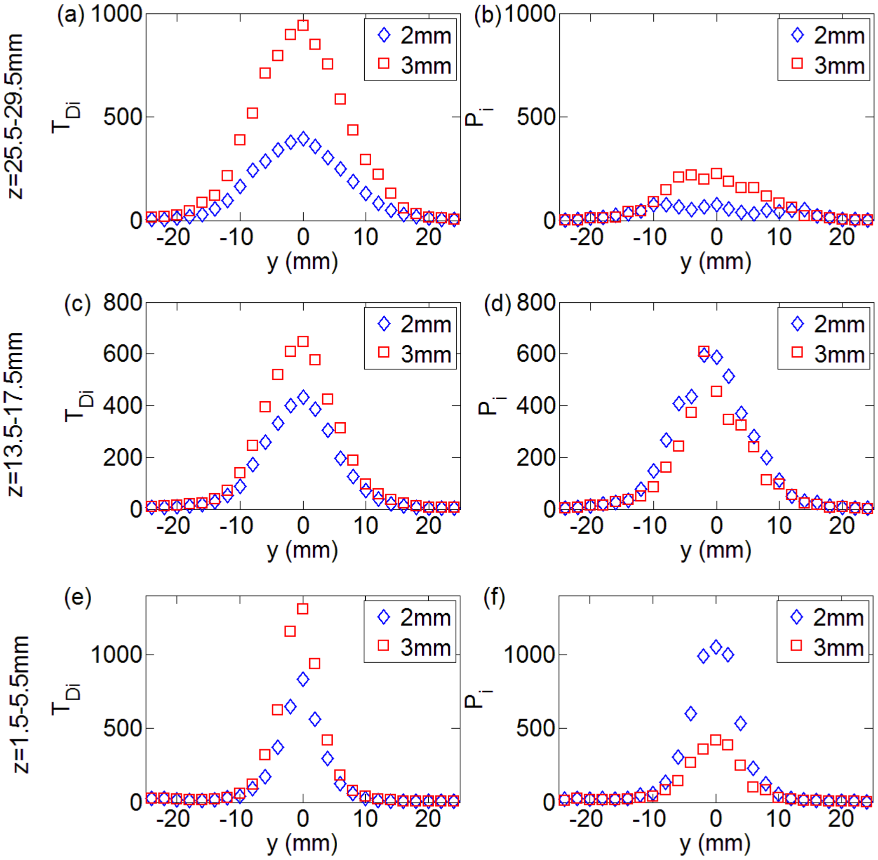

Figure 4.18: Profiles of dynamic temperature and pressure at three different heights z at $t = 0 - 10$ s. The first column shows the dynamic granular temperature for each component $T_{Di} = m_i T_i$, normalized by $\rho_m g R^4$. The second column shows the granular pressure for each component normalized by $\rho_m g R$, where $R = 1$ mm is the radius of small particles.

than that of smaller particles at the bottom [Fig. 4.18(f)]. In the middle layers, the pressure is quite similar for both species [Fig. 4.18(d)]. In all cases, like the granular temperature, pressure peaks at the center of the shear band.

Each of the segregation / mixing forces calculated by equation (4.14) is plotted in first column of Fig. 4.19. While d_P and d_n are somewhat noisy and do not exhibit a clear trend, d_T exhibits a clear trend, negative on the left side of the shear band, and positive on the right side of the shear band in all heights. The sum of these d_s is plotted

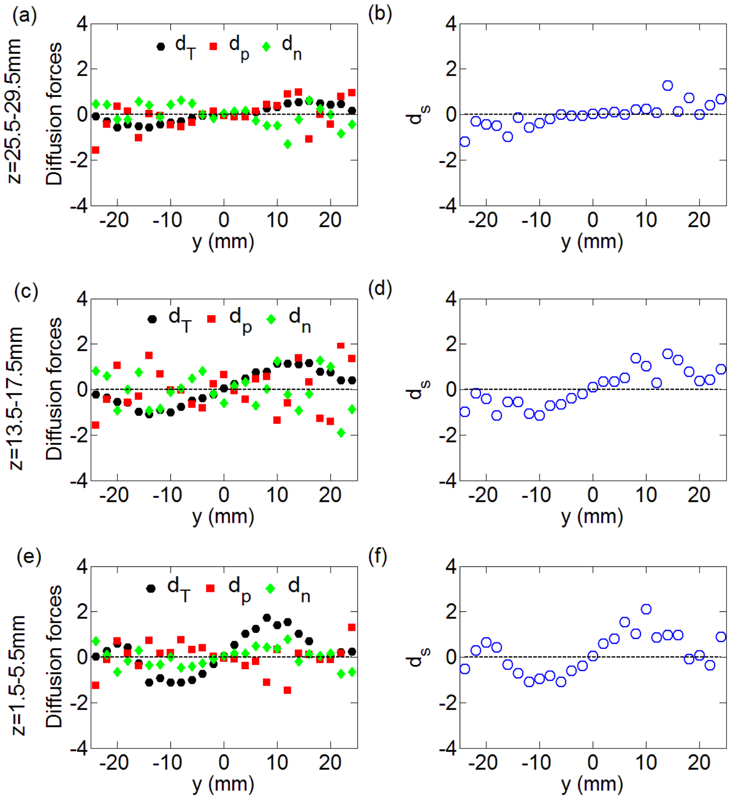

Figure 4.19: First column shows segregation and mixing "driving forces" associated with pressure (d_p), dynamic temperature (d_T), and ordinary diffusion (d_n) as defined in the text at three different heights z. The second column shows sum of the driving forces associated with segregation and mixing: $d_s = d_p + d_T + d_n$ at three different heights z. The "diffusion forces" are normalized by $1/R$, where $R = 1$ mm is the radius of small particles.

in second column of Fig. 4.19. Like d_T, for $y < 0$, d_s >0 and for $y > 0$, d_s <0 indicating that the small particles are forced into the center of the shear band.

The predicted diffusion velocities $v_s - v_l$ at three heights at $t = 0 - 10$ s calculated by kinetic theory are plotted in the first column of Fig. 4.20 to compare with simulation results at same time interval and heights in the second column of Fig. 4.20 . At all three heights, for $y < 0$, $v_s - v_l > 0$, and for $y > 0$, $v_s - v_l < 0$, which indicate that the small particles will move to center of shear zone relative to the large particles according to kinetic theory. However, at the bottom and middle of parallel cell, the actual difference

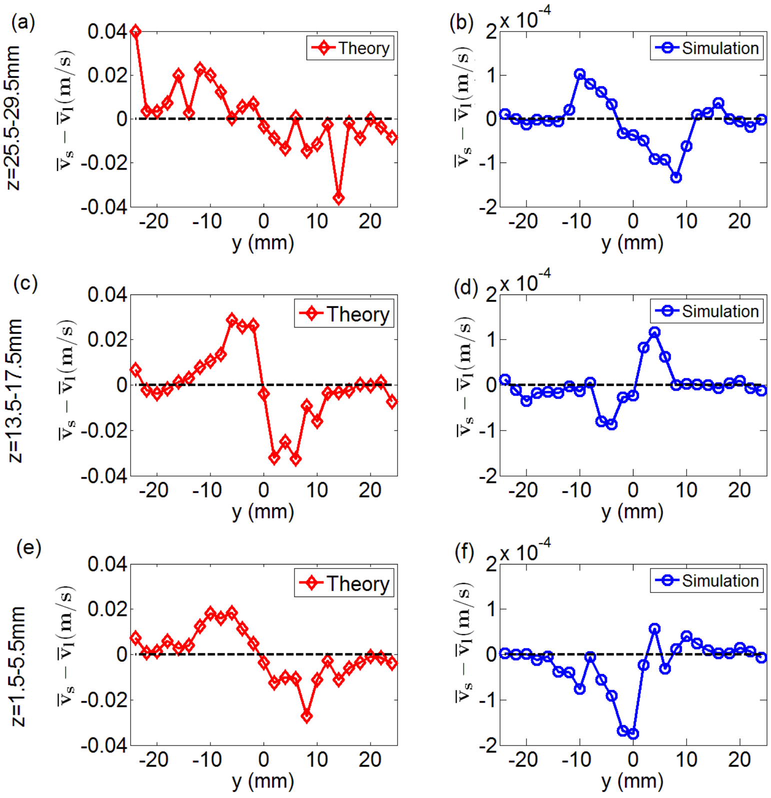

Figure 4.20: Comparisons between theoretical predictions and simulation measurements at three different heights. The first column shows predicted diffusion velocity between small and large particles calculated according to Equation (4.11). The second column shows actual diffusion velocity difference calculated from the DEM simulation results at $t = 0 - 10$ s.

in measured velocities [Fig. 4.20(d) and (f)] actually is smaller (by approximately two orders of magnitude) than that predicted by kinetic theory. Perhaps more importantly, the measured velocity indicates that the smaller particles are actually moving out of the shear zone, opposite to that predicted by Equation (4.11). In other words, in the form of kinetic theory taking into account particle inelasticity and non-equipartition of temperature, the theory predicts that large particles segregate to the region of lowest dynamic temperature and pressure. For the system reported here, in the bulk where the contacts with neighbors are multiple and enduring, large particles actually segregate to the region of higher dynamic temperature and pressure. In contrast, close to free surface,

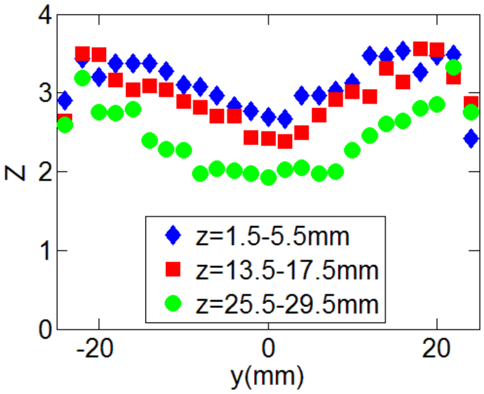

Figure 4.21: Coordination number Z as a function of y averaged at three different heights at t = 0-10 s.

although kinetic theory still over-predicts segregation fluxes in two orders of magnitude larger, the segregation trends are well predicted, where small particles move toward center of the cell, the region of higher dynamic temperature and pressure. This good prediction for segregation trend may attribute to a lower average solids fraction close to free surface so that the flow becomes more energetic and binary collision becomes more dominant.

To more clearly show the evidence of the change of microscopic characteristics and nature of particle contact at different heights, the average coordination number profiles in y direction $Z(y)$ at these three different heights are plotted in Figure 4.21. It apparently shows a decrease of Z as increasing heights. When close to the free surface, the average coordination numbers can be as low as 2 in center of shear band. Though this value of Z near free surface does not mean all collisions are binary, the nature of collisions is actually greatly different from that in the middle and bottom layers and has more characteristics of instantaneous and binary collisions. On the other hand, because the collisions in the surface layers are still not fully dominated by binary collisions, this is why the kinetic theory over-estimates segregation fluxes as also evidenced by Ref. [89] for slightly dense systems.

The conclusions from this are twofold. First, the differences between the predictions from kinetic theory and the computational results are indicative of the importance of the nature of the bulk dynamics in determining the form of segregation. The framework of kinetic theory most readily available is based on assumptions that the particle interactions are binary and near-instantaneous, whereas in the system reported here particle contacts are multiple and enduring. It is, therefore, not surprising that different segregation effects arise from these different system dynamics; these results point to the importance of the interactions in determining the segregation details. In other words, rather than indicate that there is some failing in kinetic theory, these results indicate that in fact there is a significance in what might be considered these different phases of sheared granular systems that affects the nature of the shear-driven segregation. The second set of conclusions from this analysis regards some assumptions within the framework of kinetic theory closest to dense sheared granular flow. One modification that may improve the predictions of kinetic theory for denser sheared systems like the split-bottom cells could involve the radial distribution function. Its current form is based on a system where binary collisions dominate the interparticle interactions. As discussed, this is not the case for the mixtures sheared in split-bottom cells where inertia effects appear negligible. Perhaps if the radial distribution functions were modified to account for effects associated with systems such as these, kinetic theory would better reproduce the segregation dynamics in denser flows such as those in the split-bottom cell.

4.4 Summary

In summary, a split-bottom cell is used to study segregation computationally, with an emphasis on determining the origin of horizontal segregation patterns in these systems. In the computational simulations both horizontal and vertical segregation patterns are observed in both the circular and parallel split-bottom simulated cells. In both cells, vertical fluxes of large particles upward and small particles downward lead to vertical segregation patterns at the top and bottom of the cells. However, it appears the underlying driving mechanism for the horizontal segregation pattern is different for the two types of cells. In the circular cell, while there may be the tendency for small horizontal segregation fluxes, the effects are suppressed by the more prominent dynamics associated with the convection roll causing all particles to rise in the middle at smaller radii and to sink on the outside at larger radii. These have the effect of rotating a vertical segregation pattern (that is likely driven by gravity) outward leading to a net horizontal segregation pattern. These observations suggest what appears to be some contradictory results for shear-induced segregation in dense flows may in fact be due to a combination of other segregation effects and particle advection. In the parallel split-bottom cell, no global convection roll is observed. In this case, a small horizontal flux is apparent of small particles away from the highest shear rate and highest granular temperature, and large particles tend to move inward.

Expressions derived within the framework of kinetic theory are used to determine whether or not the horizontal segregation velocities observed in the parallel cell are associated with pressure and temperature gradients derived from the measured kinematics. The theoretically predicted segregation velocities are found to be much larger and in the opposite direction to those measured in the simulations in the bulk flow. These differences appear to be associated with the nature of the inter-particle collisions and their influence on segregation trends. Granular mixtures whose dynamics are dominated by near instantaneous binary collisions appear to segregate differently than those whose dynamics are dominated by multiple enduring contacts with their neighbors. On the other hand, this form of kinetic theory are applicable to predict segregation trend of horizontal segregation at the very top of these split-bottom systems where the particles are more sparse, and inter-particle collisions may be more important in the dynamics, though the magnitude of segregation fluxes is over-predicted.

To study these effects more systematically, the effect of gravity-driven segregation needs to be minimized. In next chapter, simulations of the flow of granular mixtures of different-sized particles with varying system solids fraction in a vertical chute will be described.

Chapter 5

Phase transition of shear-induced segregation in vertical chute flow

In this Chapter, segregation associated with a shear rate gradient is investigated as it varies with the average system solids fraction. To do so, a vertical chute is used to isolate and accentuate the effect of a shear rate gradient on segregation. As shown for other shear-induced effects [10][81][82][151][152], this geometry is ideal for studying the effect of shear rate gradients on segregation because of its simple geometry but inhomogeneous flow structure.

5.1 Simulation setup and results

For these simulations the Discrete Element Method (DEM) is used which is outlined in Chapter 3. A mixture of different sized spheres is simulated with interaction coefficients outlined in Table 3.2. As described in Chapter 3 50/50 mixtures (by weight) of spherical particles 2 and 3 mm in diameter with a polydispersity of 10% to impede crystallization are used. System solids fraction $\langle \overline{f} \rangle$ is varied from one simulation to the next: $\langle \overline{f} \rangle =$ 0.21 - 0.60. (The number of particles in each simulation N varies from 2976-8089.) The boundary conditions used are that of a vertical chute of dimensions D =40 mm, W =50 mm and $L =$ 50 mm in the x, y, and z directions, respectively [see Fig. 5.1(a)]. The boundaries are periodic in the z- (vertical) and x- directions. There is one set of vertical side walls (in the y- direction), which are roughened using randomly close

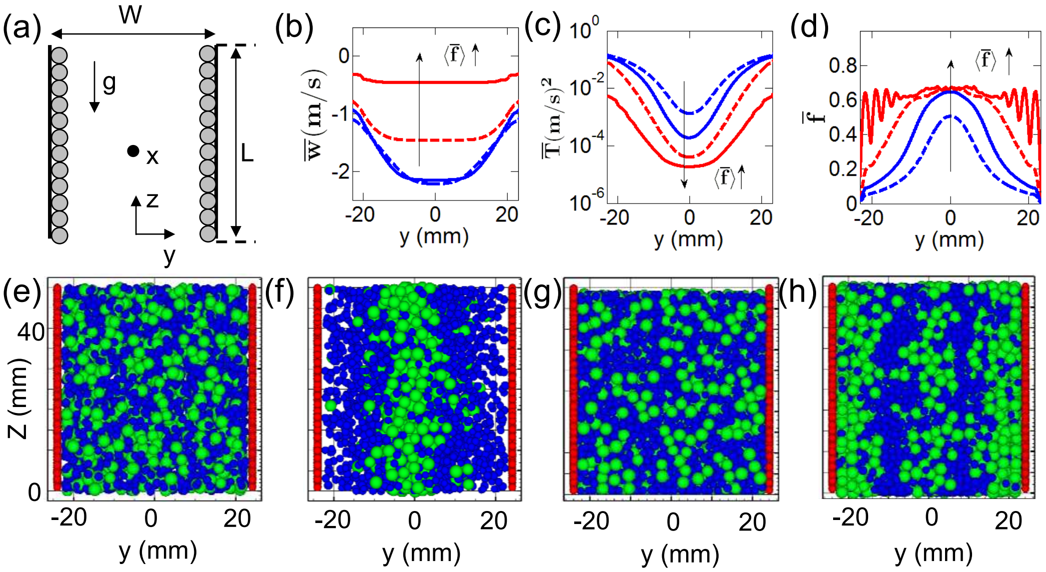

Figure 5.1: (a) Sketch of a vertical chute. (b)-(d) Profiles of kinematic quantities for four mixtures once steady state is reached (t=50s for $\langle \overline{f} \rangle$=0.21 and 0.34 and t=400s for $\langle \overline{f} \rangle$=0.47 and 0.60). (b) Average streamwise velocity $\overline{w}$, (c) Average granular temperature $\overline{T}$ and (d) Average solids fraction of the mixture $\overline{f}$. (e)-(h) Snapshots of two mixtures at t=0s and steady state. (e) $\langle \overline{f} \rangle$=0.21 at t=0s (f) $\langle \overline{f} \rangle$=0.21 at t=50s (g) $\langle \overline{f} \rangle$=0.60 at t=0s and (h) $\langle \overline{f} \rangle$=0.60 at t=400s. 2mm particles: blue (dark); 3mm particles: green (light). Copyright (2011) by the American Physical Society.

packed 2 mm spheres. The velocity components are denoted as $\vec{u}=u\vec{x}+v\vec{y}+w\vec{z}$ according to the directions noted in Fig. 5.1(a).

For each simulation, the flowing particles are arranged randomly in the chute and then released with small random velocities. After their initial release, particles collide with one another and with the vertical walls as they initially accelerate downward. Dissipation of energy through interparticle and wall-particle interactions limits the velocity throughout the cell. Steady-state conditions are reached within 10 seconds [see Fig. 5.2]. The steady-state kinematic profiles of the granular mixtures are similar to those in monosized system measured in the physical and computational experiments (e.g., Refs. [82, 151, 81, 153]). At the highest solids fractions, the vertical velocity profile $\overline{w}$ resembles a plug flow; at the lower solids fractions, the velocity is higher and the profile is roughly parabolic [Fig. 5.1(b)]. In all cases, the granular temperature $\overline{T}$ is highest

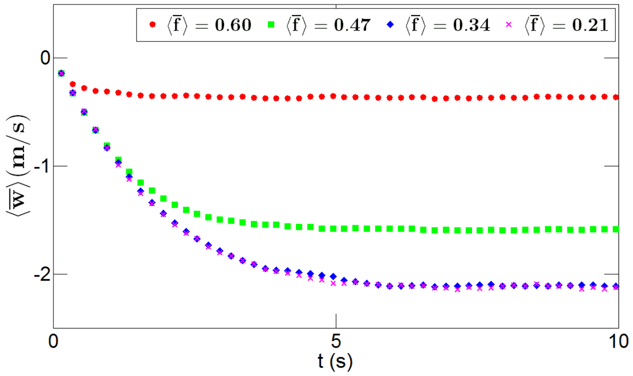

Figure 5.2: Streamwise velocity $\langle \overline{w} \rangle$ averaged in the whole chute cell as a function of time t in the first 10 seconds for four different systems: $\langle \overline{f} \rangle$=0.21,$\langle \overline{f} \rangle$=0.34, $\langle \overline{f} \rangle$=0.47 and $\langle \overline{f} \rangle$=0.60.

near the walls where the shear rate $\dot{\gamma} = d\overline{w}/dy$ is the greatest, and generally higher for lower values of $\langle \overline{f} \rangle$ [Fig. 5.1(c)]. Regions of low $\overline{T}$ and low $\dot{\gamma}$ correspond to regions of high $\overline{f}$ [Fig. 5.1(d)].

It is clear that segregation in the sparsest simulations proceeds similarly to segregation reported under other boundary conditions for sparse systems (e.g. [67, 87]). Specifically, all particles move to regions of low T in the center of chute, though large particles do so more efficiently [See Figs. 5.1 (e)-(f)]. In contrast, in the densest simulations, the larger particles segregate away from the region of highest f to the region of high T and $\dot{\gamma}$ near the walls [See Figs. 5.1 (g)-(h)].

To investigate these trends more quantitatively, the solids fraction profiles and the segregation flux profiles for each component for a few different solids volume fractions are plotted in Fig. 5.3. Row 1 of Figs. 5.3 (a) and (b) show $\overline{f}_i(y)$ of each component i and the mixture $\overline{f}(y)$ for the steady state for $\langle \overline{f} \rangle = 0.21 - 0.60$. These plots indicate there is a gradual change of the segregation pattern from one where large particles gather in low-T and -$\dot{\gamma}$ regions to one where they gather in high-T and $\dot{\gamma}$ regions. As $\langle \overline{f} \rangle$ increases from 0.21 to 0.60 a gradual transition is apparent in what might be seen as an increasing repulsion of the large particles from the central region beginning with solids fractions as low as $\langle \overline{f} \rangle \sim 0.37$. For the systems with $\langle \overline{f} \rangle$=0.55 and 0.60, the segregation in the center is non-zero, but quite slow, apparently due to the creeping

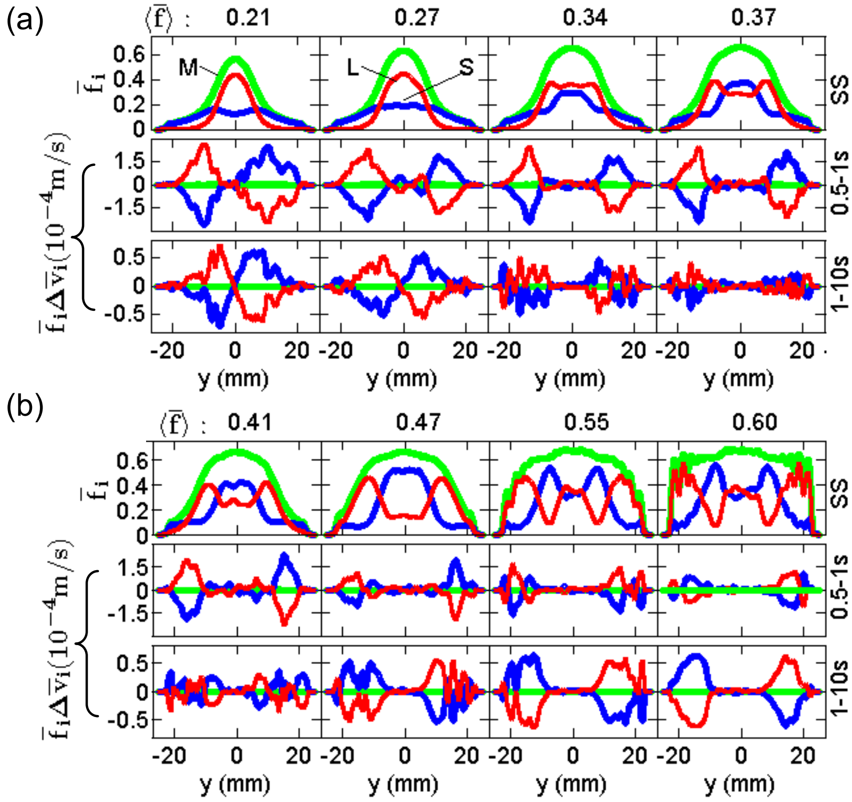

Figure 5.3: Segregation kinematics of eight systems with different $\langle \overline{f} \rangle$'s. (a) $\langle \overline{f} \rangle = 0.21 - 0.37$ and (b) $\langle \overline{f} \rangle = 0.41 - 0.60$. Row 1: $\overline{f}_i(y)$ for the mixture (M) and large (L) and small (S) particles at steady state (SS). Rows 2 and 3: segregation fluxes $\overline{f}_i \Delta \overline{v}_i$ averaged over t= 0.5 - 1 s (row 2) and 1 - 10s (row 3). Mixture (M): green(gray), 3 mm particles (L): red(thin black) and 2 mm particles (S): blue(thick black).

dynamics in the center plug-like region of the flow.

The time dependence of the segregation is more clear using a measure of segregation $\overline{\sigma}$ as a function of time as shown in Fig. 5.4. The standard deviation $\overline{\sigma}$ of mean concentration of each species in segregation direction averaged in certain time interval is calculated by $\overline{\sigma} = \sqrt{\sum_{j=1}^{N_y} (\phi_j - \overline{\phi}_j)^2/(N_y - 1)}$, where $N_y = 2500$ is the number of bins in y direction, ϕ_j is concentration of each species in bin j and $\overline{\phi}_j$ is mean concentration of this species in the system. Figs. 5.4 (a) - (d) show $\overline{\sigma}$ as a function of time t for dilute and dense system respectively in whole course of simulation. The curve is fit

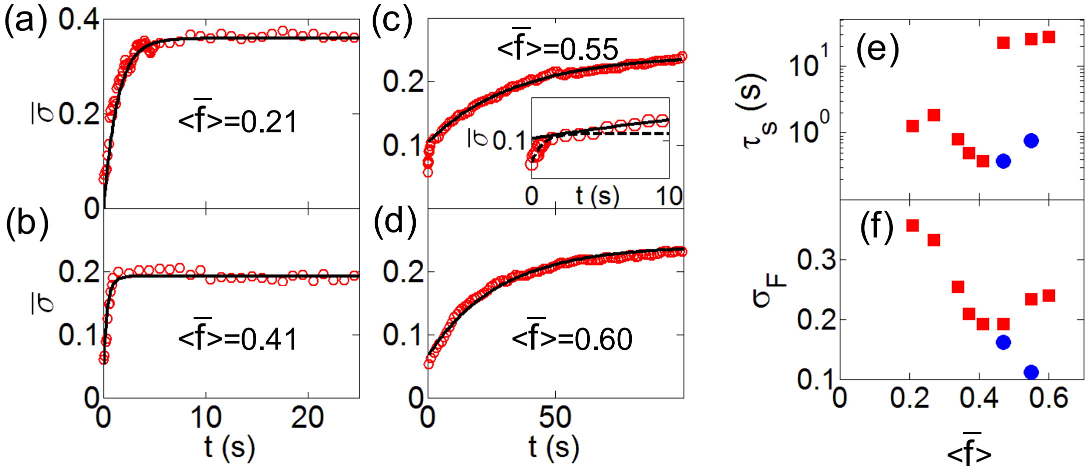

Figure 5.4: (a)-(d) show segregation measure $\overline{\sigma}$ as defined in the text as a function of time for four systems (a) $\langle \overline{f} \rangle = 0.21$ (b) $\langle \overline{f} \rangle = 0.41$ (c) $\langle \overline{f} \rangle = 0.55$ and (d) $\langle \overline{f} \rangle = 0.60$. The solid lines are fitting curves as described in the text. The inset in (c) shows fitting curves of two stages of segregation process: Initial quick segregation (dotted line) and segregation in the entire simulation (solid line). (e) and (f) Show fitting parameters σ_F and τ_s as a function of $\langle \overline{f} \rangle$. Square symbols for entire simulation and circle for initial segregation.

by exponential equation $\overline{\sigma}(t) = \sigma_F - \sigma_\delta \exp(-t/\tau_s)$, where σ_F indicates the degree of segregation at steady state and τ_s indicates the characteristic time scale for segregation. For the intermediate $\langle \overline{f} \rangle$ like 0.47 and 0.55, the data are also fit just after beginning of simulations with same fitting equation to separate the two stages of segregation apparent in these plots [See inset of Fig. 5.4(c)]. All fitting parameters (including both sets of fitting parameters for the intermediate regimes) are plotted in Figs. 5.4(e) and (f). One can see that segregation from dilute to dense system occurs over dramatically different time scales from a few seconds to hundred seconds [See Fig. 5.4(e)].

To investigate the dynamics that give rise to these steady state concentrations, the segregation flux $\overline{f}_i \Delta \overline{v}_i$ is plotted in the 2nd and 3rd rows of Figs. 5.3 (a) and (b). It is shown that immediately following the release of the particles ($t = 0.5 - 1$s) the large particles actively segregate to the center of the cell for all cases except for the highest two solids fractions investigated, $\langle \overline{f} \rangle = 0.55, 0.60$ [Figs. 5.3 (a) and (b), row 2]. However, when these dynamics are viewed over a slightly longer period of time ($t = 1-10$s) [Figs.

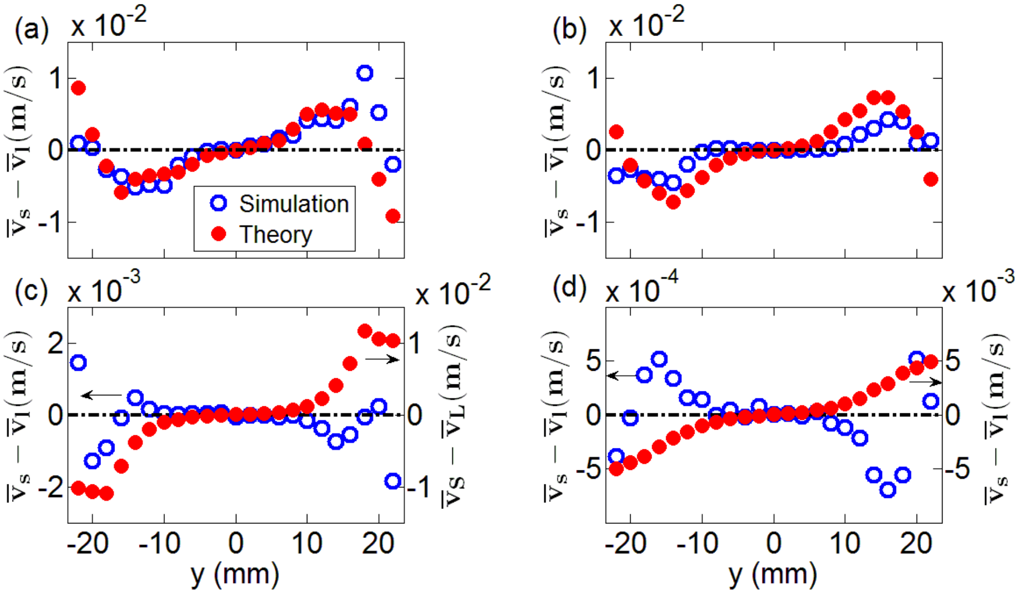

Figure 5.5: Average segregation velocity $\overline{v}_s - \overline{v}_l$ at 0.5-1 s from simulation results and from kinetic theory, derivation summarized in Section 4.3 for: (a) $\langle \overline{f} \rangle = 0.21$; (b) $\langle \overline{f} \rangle = 0.34$; (c) $\langle \overline{f} \rangle = 0.55$; (d) $\langle \overline{f} \rangle = 0.60$. Copyright (2011) by the American Physical Society.

5.3(a) and (b), row 3], the reversal in the segregation fluxes occurs at a lower system solids fraction $\langle \overline{f} \rangle \sim 0.41$. (Fluxes are similar at longer time scales, and diminish as the system approaches steady state.) It is noted that this reversal of segregation direction occurs for higher $\langle \overline{f} \rangle$'s even where the local value of $f(y)$ is relatively low.

The computational data reported here are compared with predictions from current formulations of kinetic theory that include the non-equipartition of granular temperature as Refs. [28][67], summarized in Section 4.3. Specifically, the "diffusion velocity", the difference between the velocities of the two species $\overline{v}_s - \overline{v}_l$ is considered. Figure 5.5 contains predictions of the diffusion velocity from kinetic theory based on local kinematics with velocities measured from the simulations for a few values of $\langle \overline{f} \rangle$ for $t = 0.5 - 1$s [as in Figs. 5.3 (a) and (b), row 2]. The results agree qualitatively and quantitatively for the lowest system solids fractions, e.g., $\langle \overline{f} \rangle = 0.21$ [Fig. 5.5(a)], though this agreement is not as good for higher $\langle \overline{f} \rangle$ as low as 0.34 [Fig. 5.5(b)]. Further, as shown in Figs. 5.5(c) and (d), in the denser systems, $\langle \overline{f} \rangle = 0.55$ and 0.60, the diffusion velocity predicted

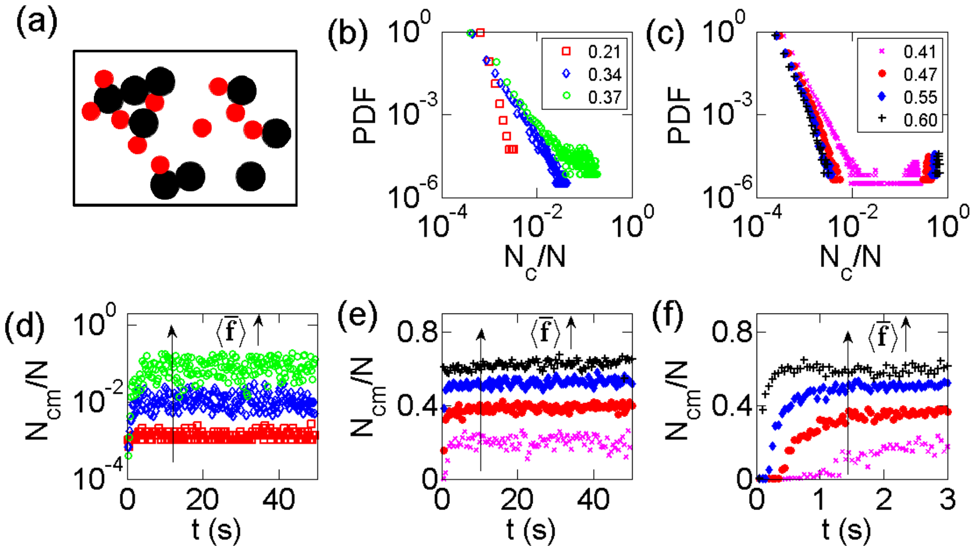

Figure 5.6: (a) Sketch illustrating 4 clusters with 2 singletons. (b)-(c) Probability distribution function (PDF) of N_c/N for (b) $\langle \overline{f} \rangle = 0.21$, 0.34, and 0.37, and (c) $\langle \overline{f} \rangle = 0.41, 0.47, 0.55, 0.60$. (d)-(e) Time dependence of the maximum cluster size N_{cm}/N for (d) $\langle \overline{f} \rangle = 0.21$, 0.34, and 0.37, and (e) $\langle \overline{f} \rangle = 0.41, 0.47, 0.55, 0.60$. (f) N_{cm}/N vs. t for systems in (e) at $t = 0 - 3$ s.

from kinetic theory is in the opposite direction (and significantly greater in magnitude) than that directly measured from the simulations. Similar results are found at later time periods, though the qualitative disagreement between theory and simulation results occurs at lower values of $\langle \overline{f} \rangle$ where the segregation direction reverses [apparent in Figs. 5.3 (a) and (b), row 3].

5.2 Microscopic structures

Since current formulations of kinetic theory require collisions to be relatively uncorrelated, it is hypothesized that the change in segregation direction and the break between results and theory have to do with an underlying change in the structure of the system. To test this hypothesis, a relatively coarse measure of the system structure is considered, the size of particle clusters within each system. Here, the size of each cluster N_c is defined by the number of particles connected via interparticle contacts [Fig. 5.6(a)]. Figures 5.6 (b)-(c) show the probability distribution function (PDF) of the normalized

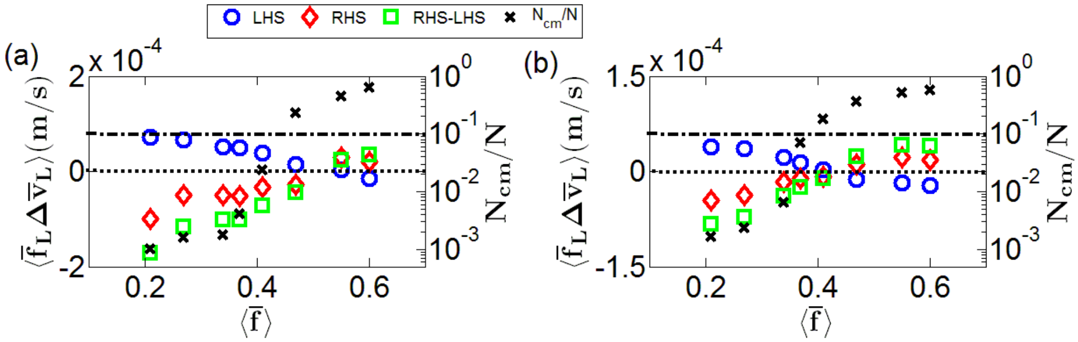

Figure 5.7: $\langle \overline{f}_L \Delta \overline{v}_L \rangle$ and N_{cm}/N vs. $\langle \overline{f} \rangle$. $\langle \overline{f}_L \Delta \overline{v}_L \rangle$ is plotted for three different regions in the chute: for $y < 0$ (LHS) and for $y > 0$ (RHS) in the positive y-direction and for the entire width of the chute outward (OUT). Data are plotted for (a) $t = 0.5 - 1$ s for $\langle \overline{f}_L \Delta \overline{v}_L \rangle$ and $t = 0.75$ s for N_{cm}/N and (b) $t = 1 - 10$ s for $\langle \overline{f}_L \Delta \overline{v}_L \rangle$ and $t = 5$ s for N_{cm}/N. The dotted line indicates $\langle \overline{f}_L \Delta \overline{v}_L \rangle = 0$, and the dash-dot line indicates $N_{cm}/N = 0.1$.

cluster size N_c/N at steady state (using data from 1000's of time steps) for different values of $\langle \overline{f} \rangle$. At lower values of $\langle \overline{f} \rangle$ [e.g., 0.21 and 0.34 in Fig. 5.6(b)] the clusters are very small, and the PDFs exhibit a power law decay. When $\langle \overline{f} \rangle$ increases to 0.37, the slope decreases and the tail of PDF becomes more complicated as several larger clusters continuously form and break apart throughout the simulation. At higher values of $\langle \overline{f} \rangle$ [Figs. 5.6 (c)], the PDF splits into two parts, one representing relatively small clusters that follow a power law, and one representing the size of the largest cluster N_{cm} at each time step. For these systems of higher $\langle \overline{f} \rangle$, N_{cm} varies slightly from one time step to the next, but unlike for $\langle \overline{f} \rangle$= 0.37, once the largest cluster forms, it is essentially permanent. In Figs. 5.6 (d) - (f), the time dependence of N_{cm}/N is plotted. For the lowest values of $\langle \overline{f} \rangle$= 0.21 and 0.34, there is no unique largest cluster; many small clusters continuously form and break apart as mentioned. At $\langle \overline{f} \rangle = 0.37$, the largest cluster can reach 20%, though it is not stable and N_{cm}/N can vary from $\sim 0.01 - 0.2$. For intermediate values of $\langle \overline{f} \rangle$=0.41, 0.47, the growth of the largest cluster is initially slow [Fig. 5.6 (f))]. However, for all systems of $\langle \overline{f} \rangle \geq 0.41$ there is a unique largest cluster that stabilizes relatively quickly and contains a significant fraction of the particles [Figs. 5.6 (e)-(f)].

Now the correspondence between the growth of N_{cm}/N and the change in segregation trend with increasing $\langle \overline{f} \rangle$ is investigated. To do so, it is noted that high-T, high-$\dot{\gamma}$ regions are always near the outer walls of the chute. Thus the average flux of each component toward the walls is computed to calculate the reversal of the segregation of component i toward high-T, high-$\dot{\gamma}$ regions. That is, for $y < 0$ $\langle \overline{f}_i \Delta \overline{v}_i \rangle_{LHS}$ is computed, and for $y > 0$ $\langle \overline{f}_i \Delta \overline{v}_i \rangle_{RHS}$ is computed and then the difference is taken: $\langle \overline{f}_i \Delta \overline{v}_i \rangle_{out} = \langle \overline{f}_i \Delta \overline{v}_i \rangle_{RHS} - \langle \overline{f}_i \Delta \overline{v}_i \rangle_{LHS}$. Positive values of $\langle \overline{f}_i \Delta \overline{v}_i \rangle_{out}$ indicates component i is segregating toward high-T, high-$\dot{\gamma}$ regions. N_{cm}/N and $\langle \overline{f}_L \Delta \overline{v}_L \rangle$ vs. $\langle \overline{f} \rangle$ is plotted in Fig. 5.7. The results for $\langle \overline{f}_L \Delta \overline{v}_L \rangle$ show the segregation flux transitions gradually from one where the large particles segregate toward low-T, low-$\dot{\gamma}$ regions to the reverse, and that the transition point corresponds at early times to $\langle \overline{f} \rangle \sim 0.5$, and at later times to $\langle \overline{f} \rangle \sim 0.42$, as also suggested by Fig. 5.3. Further, it appears the reversal in segregation trends at early and late times coincides with a maximum cluster size somewhat greater than $\sim 10\%$ of the total number of particles and shifts to the left for slightly later times as N_{cm} grows.

5.3 Summary

To summarize, while the local solids fraction f and other kinematics are non-uniform [e.g., Figs. 5.1(b)-(d)], the global solids fraction $\langle \overline{f} \rangle$ controls the segregation behavior. For systems of low system-averaged solids fraction $\langle \overline{f} \rangle$, large particles accumulate within low-$\dot{\gamma}$, low-T, high-f regions, in quantitative agreement with predictions using kinetic theory. However, for systems of high $\langle \overline{f} \rangle$, the opposite occurs and the attempt to match kinetic theory with these results reported here fails dramatically. It is also shown that the direction of segregation of large particles relative to small particles transitions at a moderate value of $\langle \overline{f} \rangle$, and the transition is likely governed by the global structure of the system: As $\langle \overline{f} \rangle$ increases, the system structure changes from one dominated by binary collisions to one dominated by one cluster that can involve $> 60\%$ of the particles and span the system.

The global solids fraction $\langle \overline{f} \rangle$ at which the transition occurs does not appear to be unique. Indeed in the results reported in this chapter, the point of transition changes as the system evolves to steady state. Further, it is expected to depend on details such as particle size distribution [37] as the maximum packing fraction changes. It is also expected to change with the coefficient of restitution and other details involving interparticle contacts. Investigations for influence of these factors on shear-induced segregation and associated microscopic structures are needed in the future work.

This Chapter is concluded by considering current models for segregation of dense granular materials in the context of the results reported here. Gray and colleagues successfully reproduce segregation of different sized particles by gravity in denser sheared systems through a continuum model that explicitly partitions pressure gradients between the different species [92, 93]. In the chute flow, the total pressure gradient is zero in the horizontal direction, so the model is not directly applicable. However, a comparable model that partitions some subset of horizontal stresses may be successful. Alternatively, a new model for segregation recently proposed by Sarkar and Khakhar shows promise as an alternate model for segregation arising from shear gradients in dense granular flows [154]. Unfortunately, the current form of this model is strictly for particles differing only in density, as segregation is driven by buoyancy forces, but it includes the consideration of an effective temperature derived from the fluctuation-dissipation relations that may reflect the effect of shear gradients on segregation in denser systems. Finally, while current models that apply kinetic theory to granular mixtures do not reproduce segregation trends for denser system, efforts are being made to extend these models to denser flows by incorporating the effect of particle clusters on the frequency of interparticle collisions (e.g., Ref. [29]). This framework appears to have the capability of capturing the system-level control of segregation observed in this research.

In the next Chapter, a new model for shear-induced size segregation in dense flow will be presented, similar to the continuum model developed by [92, 93] for gravity-driven segregation in dense systems. The proposed theoretical framework will also be validated with the simulation results in the vertical chute flow presented in this Chapter.

Chapter 6

Theory for shear-induced segregation of dense granular mixtures

In this chapter, a model for shear-induced segregation in dense flow is developed. To do so, a few important details for the highest solids fraction system in a vertical chute in Chapter 5 is first summarized. Recall that in a vertical chute, the shear rate and granular temperature are highest adjacent to vertical walls [Fig. 6.1] which enables a systematic study of the variation of shear-induced segregation with solids fraction in a vertical chute. For relatively sparse flows the large particles segregated to the low temperature low shear rate region of the chute away from the walls. However, the trend reversed for higher solids fractions and, similar to the results from Refs. [85, 96, 110, 155], the large particles segregated to the regions of high shear rate and temperature and of low solids fraction [Fig. 6.2]. The results further indicate that the transition in segregation trends coincides with the formation of a large-scale cluster of particles connected via interparticle contacts.

Based on these observations, it is hypothesized that the existence of this structure in dense systems is responsible for the reversal in segregation trends at high solids fractions reported in Refs. [85, 96, 110, 155]. It is conjectured that in all these systems dominated by shear gradients, the dynamics associated with the shear gradients pushes all particles

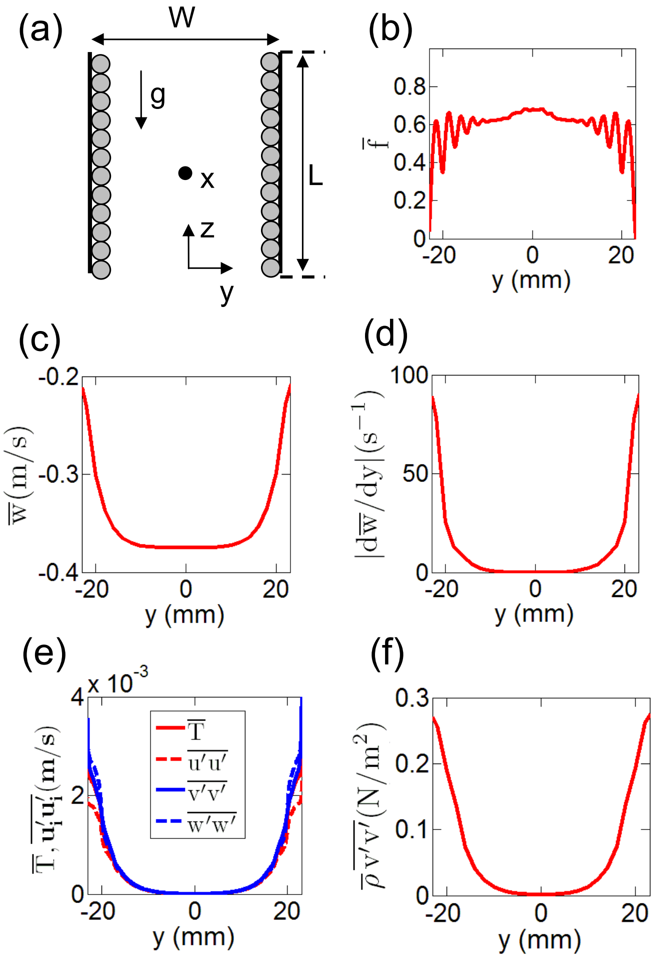

Figure 6.1: (a) Sketch of a vertical chute. (b)-(f) Profiles of kinematic quantities in y direction for mixtures averaged at t =950-1000 s for system solids fraction $\langle\overline{f}\rangle$=0.6 (b) Average solids fraction of the mixture $\overline{f}$, (c) Average streamwise velocity $\overline{w}$, (d) Absolute value of shear rate $|d\overline{w}/dy|$, (e) Average granular temperature $\overline{T} = (\overline{u'u'} + \overline{v'v'} + \overline{w'w'})/3$ and three components $\overline{u'u'}, \overline{v'v'}, \overline{w'w'}$,(f) Averaged kinetic normal stress $\rho\overline{v'v'}$.

toward regions of low shear rate and temperature in a similar way that gravity (or associated pressure gradients) pushes all particles downward. Then, the structure that forms gives rise to the dynamics associated with the kinetic sieving mechanism. While in its original form, the kinetic sieving mechanism segregates particles along pressure

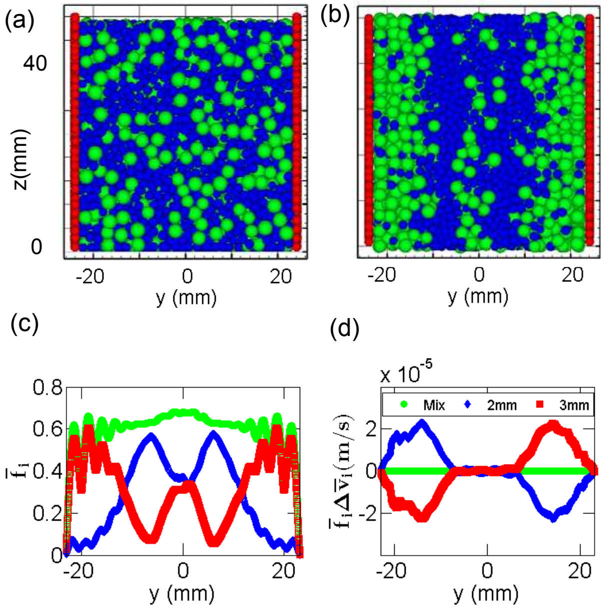

Figure 6.2: (a)-(b) Snapshots of a mixture of 2 mm (blue) and 3mm (green) glass particles at $t = 0$ s and at $t = 1000$ s for $\langle \overline{f} \rangle = 0.60$ respectively. (c) and (d) Profiles of segregation kinematics in y direction. (c) the solids fraction $\overline{f}_i$ for species i at $t = 950 - 1000$ s; (d) the horizontal segregation fluxes $\overline{f}_i \Delta \overline{v}_i$ for species i averaged at $t = 0 - 50$ s.

gradients associated with gravity, in dense systems without gravity, the kinetic sieving mechanism segregates particles along pressure (stress) gradients associated with other mechanisms.

In this Chapter, these results and the hypotheses in the context of a model for gravity-driven segregation of binary mixtures presented by Gray and colleagues [92, 93] described in Chapter 1 are presented. However, in lieu of gravity and the associated hydrostatic pressure in the model by Gray and colleagues, the effects of stresses arising from the shear rate gradients are considered. Section 6.1 presents theoretically how the separate consideration of what have been called contact and kinetic stresses may explain the mechanism behind shear-induced segregation. Sections 6.2 and 6.3 present simulation results supporting the model.

6.1 Theory

A binary mixture of different sized spherical particles with same material density ρ_m is considered. The local volume fraction filled with particles of species i is denoted by f^i; therefore, the local bulk mass density of species i, $\rho^i = \rho_m f^i$. The concentration of species i is calculated by $\phi^i \equiv f^i / \sum f^i$ which satisfies $\phi^l + \phi^s = 1$. The bulk Eulerian properties of the mixture of both species together are denoted as variables without subscripts concern, so, for example, the local average density $\rho = \sum \rho^i$ and the average local velocity $\vec{u} = \sum \vec{u}^i \phi^i$.

The conservation of mass and momentum for the mixture is first considered:

$$\frac{\partial \rho}{\partial t} + \nabla \rho \vec{u} = 0 \tag{6.1}$$

$$\frac{\partial}{\partial t}(\rho \vec{u}) + \nabla \cdot (\rho \vec{u} \otimes \vec{u}) = \nabla \cdot \vec{\sigma} + \vec{F} \tag{6.2}$$

The stress tensor is denoted as $\vec{\sigma}$, using the relatively standard sign convention for stresses as, for example, noted in Ref. [156], and body forces are denoted as $\vec{F}$. For this research the cases where the gravitational force is negligible are considered, so that $\vec{F} = 0$. The mixture velocities and densities of systems are considered to reach steady state long before segregation, and the segregation is associated with steady state dynamics. With this in mind, the temporal derivatives $\partial \rho / \partial t$ and $\partial (\rho \vec{u}) / \partial t$ are zero.

The instantaneous value of each variable q at position $\vec{r}$ is expressed as a sum of the local temporal average $\overline{q}(\vec{r})$ and the difference between its instantaneous value and the average $q'(\vec{r}, t) = q(\vec{r}, t) - \overline{q}(\vec{r})$. Incorporating this, typically called "Reynolds decomposition," [157] into Equation (6.2), the jth component of the momentum Equation (6.2) is rewritten as

$$\sum\nolimits_k \frac{\partial}{\partial x_k}[(\overline{\rho} + \rho')(\overline{u}_j + u'_j)(\overline{u}_k + u'_k)] = \sum\nolimits_k \frac{\partial}{\partial x_k}(\overline{\sigma}_{jk} + \sigma'_{jk}) \tag{6.3}$$

Next, both sides of Equation (6.3) are averaged, using basic identities such as $\overline{\overline{q}} = \overline{q}$, $\overline{q'} = 0$, $\overline{\overline{p} q'} = 0$ and $\overline{p + q} = \overline{p} + \overline{q}$. It is assumed temporal correlations between velocity fluctuations and densities are negligible – i.e., $\frac{\partial}{\partial x_k}(\overline{u}_j \overline{\rho' u'_k})$, $\frac{\partial}{\partial x_k}(\overline{u}_k \overline{\rho' u'_j})$, and $\frac{\partial}{\partial x_k}(\overline{\rho' u'_k u'_j})$

≈ 0. Then the following equation is obtained:

$$\sum\nolimits_k \frac{\partial}{\partial x_k}(\overline{\rho}\ \overline{u}_k\overline{u}_j) + \sum\nolimits_k \frac{\partial}{\partial x_k}(\overline{\rho}\ \overline{u'_k u'_j}) = \sum\nolimits_k \frac{\partial \overline{\sigma^c}_{kj}}{\partial x_k} \tag{6.4}$$

The assumption that temporal correlations between velocity fluctuations and densities are negligible is tested in Section 6.2.

Now, the steady state conservation of momentum equation is applied to pseudo-2d systems such as the vertical chute flow shown in Fig. 6.1, where segregation occurs in one direction normal to the average flow (e.g., the $y-$ direction), and uniform conditions are assumed in the other two directions (e.g., the $x-$ and $z-$ directions). Then Equation (6.4) in the $y-$ direction may be simply expressed by:

$$\frac{\partial \rho\overline{v'v'}}{\partial y} = \frac{\partial \overline{\sigma}_{yy}}{\partial y} \tag{6.5}$$

In this equation, $-\rho\overline{v'v'}$ is often referred to as a Reynolds stress component (e.g., Ref. [47],[157]) and $\rho\overline{v'v'}$ is sometimes referred to as a streaming stress component (e.g., Ref. [47]), or a kinetic stress (e.g., Ref. [138]). $\overline{\sigma}^k_{yy} = \rho\overline{v'v'}$ is denoted as a kinetic stress following Ref. [138] in this research. It is also noted that for dry macroscopic particles, the normal contact stress will be solely compressive, whereas in the standard sign convention for $\vec{\sigma}$ (e.g., Ref. [156]) positive normal stresses such as $\overline{\sigma}_{yy}$ are positive only for tensile, negative for compressive stresses. Therefore a contact stress tensor $\vec{\sigma}^c = -\vec{\sigma}$ is defined so that terms such as $\overline{\sigma}^c_{yy}$ are positive for the problem reported here. Then Equation (6.5) is rewritten as:

$$\frac{\partial \overline{\sigma}^c_{yy}}{\partial y} + \frac{\partial \overline{\sigma}^k_{yy}}{\partial y} = 0 \tag{6.6}$$

Next, the conservation laws for two species are investigated:

$$\frac{\partial \rho^i}{\partial t} + \nabla\cdot(\rho^i \vec{u}^i) = 0 \tag{6.7}$$

$$\frac{\partial(\rho^i \vec{u}^i)}{\partial t} + \nabla\cdot(\rho^i \vec{u}^i \otimes \vec{u}^i) = \nabla\cdot\vec{\sigma}^i + \vec{F}^i + \vec{\beta}^i \tag{6.8}$$

Here, each of the terms used for species i are identical to those used for the mixture in Equation (6.2), with the exception of the new term $\vec{\beta}^i$ which represents the interaction force exerted on species i by the other component. Note $\vec{\sigma}^{c,i}$ is the local stress born by species i, and that the total stress $\vec{\sigma}^c = \sum \vec{\sigma}^{c,i}$. By performing Reynolds decomposition and then averaging both sides of Equation (6.8), similar arguments are used to those employed for the mixture and a somewhat simplified form of the conservation equation for each species in y direction is obtained:

$$\frac{\partial}{\partial t}\left(\overline{\rho^i}\ \overline{v^i}\right) + \frac{\partial}{\partial t}\left(\overline{\rho^{i'} v^{i'}}\right) + \frac{\partial}{\partial y}\left(\overline{\rho^i}\ \overline{v^i}^2\right) + \frac{\partial}{\partial y}\left(\overline{\rho}^i \overline{v'^i v'^i}\right) = \frac{\partial \overline{\sigma^i}_{yy}}{\partial y} + \overline{\beta^i_y} \tag{6.9}$$

Again, it is assumed terms involving correlations between velocity and density fluctuations such as $\frac{\partial}{\partial x^i_k}(\overline{u}^i_j \overline{\rho'^i u'^i_k})$, $\frac{\partial}{\partial x_k}(\overline{u}^i_k \overline{\rho'^i u'^i_j})$, and $\frac{\partial}{\partial x_k}(\overline{\rho'^i u'^i_k u'^i_j})$ are negligible, which are checked for a vertical chute flow in Section 6.2. The first three terms in Equation (6.9) are not so easily discounted for the individual components as analogous for the mixed case, as $\overline{v^i}$ is expected to be nonzero and changing while the component is segregating and the spatial derivative of ρ^i is nonzero after segregation. However, in dense sheared flows v^i has been shown to be typically quite small except when ρ is uniform (e.g., Refs. [155] and [158]) and as may be seen in Fig. 6.2(d) $\partial \overline{v^i}/\partial y$ is still quite small even during segregation. Therefore these acceleration term are neglected as well, and the assumption that they are negligible is tested in Section 6.2. With these assumptions Equation (6.9) can be rewritten as

$$-\frac{\partial \overline{\sigma^{c,i}}_{yy}}{\partial y} - \frac{\partial \overline{\sigma^{k,i}}_{yy}}{\partial y} + \overline{\beta^i_y} = 0 \tag{6.10}$$

Note that all terms in Equations (6.6) and (6.10) are averaged and the overbar is dropped from this point in this thesis on, so that unless noted q refers to the average $\overline{q}$.

The discussion above reflects much of the notation from mixture theory (e.g., Refs. [159, 160, 161]). However, there are a few notable exceptions in the assumptions, which is noted here. In mixture theory the velocities of the constituents are assumed equal to the bulk velocity ($\vec{u}^i = \vec{u}$), though this cannot be the case for segregating mixtures, and $\vec{u} = \sum \vec{u}^i \phi^i$ as previously noted. Along these lines, as demonstrated in Ref. [84], this is not true of the velocity fluctuation correlations that comprise the kinetic stress terms where typically $\overline{u'^s_k u'^s_j} > \overline{u'^l_k u'^l_j}$. Additionally, while mixture theory assumes that other fields are related by linear volume fraction scalings (e.g., $\vec{\sigma}^i = \phi^i \vec{\sigma}$), Gray and Thornton

[92] proposed that for mixtures of different size particles the pressure for small and large constituents will not partition with linear volume fraction scalings.

Considering these previous studies, and following the lead of Gray and Thornton [92] as it applies to the contact and kinetic stresses, the following relations are suggested:

$$\sigma_{yy}^{c,i} = \psi^{c,i}\sigma_{yy}^{c}, \sigma_{yy}^{k,i} = \psi^{k,i}\sigma_{yy}^{k}, \tag{6.11}$$

where $\psi^{c,i}$ and $\psi^{k,i}$ determine the proportion of normal contact and kinetic stresses carried by large and small particles and are not necessarily equal to ϕ^i. They must follow two constraints, (1) that $\psi^l + \psi^s = 1$, and (2) if only one species is present then it must support the entire local stress, so that when $\phi^i = 1$, $\psi^j = \delta_{ij}$, where δ_{ij} is the Kroenicker Delta function.

Considering Equation (6.11), Equation (6.10) is rewritten as

$$0 = -\frac{\partial}{\partial y}(\psi^{c,i}\sigma_{yy}^{c}) - \frac{\partial}{\partial y}(\psi^{k,i}\sigma_{yy}^{k}) + \beta_y^i \tag{6.12}$$

For the interaction term β_y^i, the following equation is used:

$$\beta_y^i = \sigma_{yy}^{c}\partial\psi^{c,i}/\partial y + \sigma_{yy}^{k}\partial\psi^{k,i}\partial y - \rho^i c_D(v^i - v) - \rho d\partial\phi^i/\partial y \tag{6.13}$$

following the form first suggested by Gray and Thornton in Ref. [92]. The first two terms on the right hand side of the equation ensure that, as in Darcy's law, the percolation process (in this case, the kinetic sieving process) is driven by intrinsic rather than partial pressure gradients. The third term is a linear drag law similar to that provided by Morland [161] for the percolation of fluids – c_D is the linear drag coefficient. The fourth term acts as a "remixing force" (e.g., [93] and [161]) that drives grains of constituent i towards areas of lower concentration similar to diffusion.

When Equation (6.13) is substituted into Equation (6.12), the following equation is obtained:

$$0 = -\psi^{c,i}\frac{\partial\sigma_{yy}^{c}}{\partial y} - \psi^{k,i}\frac{\partial\sigma_{yy}^{k}}{\partial y} - \rho^i c_D(v^i - v) - \rho d\frac{\partial\phi^i}{\partial y} \tag{6.14}$$

Combining this equation with Equation (6.6), one can express a segregation flux of species i as:

$$\phi^i(v^i - v) = \frac{\psi^{c,i} - \psi^{k,i}}{c_D}\frac{1}{\rho}\frac{\partial \sigma^k_{yy}}{\partial y} - \frac{d}{c_D}\frac{\partial \phi^i}{\partial y} \tag{6.15}$$

To facilitate a physical interpretation of Equation (6.15), new variables $R^{c,i} = \psi^{c,i}/\phi^i$ and $R^{k,i} = \psi^{k,i}/\phi^i$ are introduced to represent the ratio between fraction of the local stress (both contact and kinetic) carried each species and its local concentration in the mixture. Then Equation (6.15) can be rewritten as

$$\phi^i(v^i - v) = \frac{(R^{c,i} - R^{k,i})\phi^i}{c_D}\frac{1}{\rho}\frac{\partial \sigma^k_{yy}}{\partial y} - \frac{d}{c_D}\frac{\partial \phi^i}{\partial y} \tag{6.16}$$

From this equation, one can see that if $R^{c,i}, R^{k,i} = 1$, that is, the local stress of both types born by each species is equal to its local concentration, Equation (6.16) indicates there should be no segregation. If this is not true of both contact and kinetic stress, but $R^{c,i} = R^{k,i}$, still Equation (6.16) indicates there should be no segregation. However, if $R^{c,i} \neq R^{k,i}$, Equation (6.16) indicates that, in the context of a stress gradient ($\partial \sigma^k_{yy}/\partial y \neq 0$), segregation should occur. Further, the direction of segregation is indicated by the sign of $(R^{c,i} - R^{k,i})\partial \sigma^k_{yy}/\partial y$.

Now the results reported here are compared with those from the related theory for segregation associated with gravity developed by Gray and colleagues [92] [93]. In Gray and Thornton model, they considered shallow flows driven by gravity, down an inclined plane whose angle of inclination with the horizontal is ζ. In the case, $\tilde{z}$ is denoted as the direction perpendicular to the free surface, comparable to the $y-$direction in the discussion reported here, as the granular mixture is sheared and segregates in this $\tilde{z}$-direction, while the flow is assumed uniform in all other directions. They assumed that the acceleration terms on the left hand side of Equations (6.2) and (6.8) are negligible and that $\vec{F}$ is the weight of the material, so that Equation (6.2) in the $\tilde{z}$ direction may be:

$$\rho g \cos \zeta = -\frac{\partial p}{\partial \tilde{z}} \tag{6.17}$$

comparable to Equation (6.5) in this thesis, where p is analogous to $-\sigma_{\tilde{z}\tilde{z}}$. As mentioned, Gray et al. [92, 93] suggested that p is partitioned between the species as

$$p^i = \psi^{p,i} p, \tag{6.18}$$

where $\psi^{p,i}$ determine the proportion of pressure carried by species i and is not necessarily equal to ϕ^i. They showed that based on this, conservation of momentum in the $\tilde{z}$-direction for mixture component i (compared with Equation (6.12)) could be written

$$0 = -\frac{\partial}{\partial \tilde{z}}\psi^{p,i}p - \rho^i g\mathrm{cos}\zeta + \beta^{\mathrm{i}}_{\tilde{\mathrm{z}}} \tag{6.19}$$

where

$$\beta^i_{\tilde{z}} = p\frac{\partial \psi^{p,i}}{\partial \tilde{z}} - \rho^i c_D(w^i - w) - \rho d\frac{\partial \phi^i}{\partial \tilde{z}} \tag{6.20}$$

Here, w^i and w are the velocities in the $\tilde{z}$-direction of species i and the mixture, respectively. p can be found by integrating Equation (6.17); for example, assuming $\tilde{z} = h$ where $p = 0$, $p = (h - \tilde{z})\rho g\mathrm{cos}\zeta$.

Combining Equations (6.17), (6.18), (6.19), (6.20), the segregation flux for species i in the $\tilde{z}$-direction could be written

$$\phi^i(w^i - w) = (\psi^{p,i} - \phi^i)(g/c_D)\cos\zeta - (d/c_D)(\partial\phi^i/\partial\tilde{z}) \tag{6.21}$$

Finally, a partitioning variable $R^{p,i} \equiv \psi^{p,i}/\phi^i$ is incorporated and Equation (6.21) is rearranged for a comparable form to Equation (6.16):

$$\phi^i(w^i - w) = \frac{(R^{p,i} - 1)\phi^i}{c_D}g\cos\zeta - \frac{d}{c_D}\frac{\partial\phi^i}{\partial\tilde{z}} \tag{6.22}$$

Now the model for segregation associated with gravity evidenced in Equation (6.22) and segregation associated with a shear rate gradient and associated contact and kinetic stress gradient as evidenced in Equation (6.16) can be compared.

In both cases, there is an apparent physical force that drives all particles in one direction. In the case of gravity alone (disregarding any shear rate gradients and associated kinetics), gravity pulls all particles downward, away from the free surface and in the absence of resistive forces they simply fall. In the case of a shear rate gradient alone, an associate gradient in kinetic stresses drives all particles along the kinetic stress gradient to lower stresses. In both cases when the particles encounter one another one species is driven more effectively along the relevant gradient than the other. The process by which this occurs may be seen as a kinetic sieving process allowing some particles (the smaller particles) to pass more freely through the matrix created by a dense arrangement of particles. In the case of segregation associated with gravity alone, Equation

(6.22) suggests that whichever species support a greater fraction of the pressure than their representative concentration ϕ^i – $R^{p,i} > 1$– will segregate upwards. In the case associated with a shear rate gradient alone, Equation (6.16) suggests that whichever species supports more of the contact stress than sustains the kinetic stress – $R^{c,i} > R^{k,i}$ – will segregate in the direction of increasing kinetic stress.

Since large particles rise toward the free surface in gravity-driven flows, Equation (6.22) suggests that $R^{p,l} > 1$, and $R^{p,s} < 1$, that is, that $\psi^{p,l} > \phi^l$ and $\psi^{p,s} < \phi^s$, as detailed first in Ref. [92]. In dense sheared systems where gravity can be neglected, larger particles segregate to high T regions, Equation (6.16) suggests that $R^{c,l} > R^{k,l}$, and $R^{c,s} < R^{k,s}$.

These predictions from Equation (6.16) as well as the assumptions used to derive Equation (6.16) using a vertical chute flow are tested as detailed in the next section.

6.2 Simulations

To investigate the assumptions and predictions associated with the theory in Section 6.1, simulations using the Discrete Element Method (DEM) [140] with Hertz and Mindlin theory [162][163][164] as described in Chapter 3 are performed. As described in Chapter 5, a 50/50 mixture by weight of 2 mm and 3mm spheres with a 10% poydispersity to impede crystallization is simulated. Interaction coefficients may be found in Table 3.2. These parameters are based partly on the materials properties of glass, though to reduce computational time the stiffness and density are reduced as described in the section 3.3.2.

The boundary conditions for these simulations reported here are those of a vertical chute of dimensions D =40 mm, W =50 mm and L = 50 mm in the x, y, and z directions, respectively [see Fig. 6.1(a)]. The chute cell has one set of vertical side walls (in the y- direction), that are roughened using 2 mm spheres in a random close-packed arrangement. The boundaries are periodic in the z- (vertical) and x- directions. Though simulations are performed for several different solids fractions, for the results described here simulations for a system solids fraction $\langle\overline{f}\rangle$=0.6 are focused, with a total of $\approx$ 8000 particles in the simulation. The velocity components are denoted as $\vec{u}$=$u\vec{x}$+$v\vec{y}$+$w\vec{z}$ according to the directions noted in Fig. 6.1(a).

For each simulation, the particles are initially arranged randomly in the chute and then released with small random velocities. After their initial release, particles collide with one another and with the vertical walls as they initially accelerate downward. Dissipation of energy through interparticle and wall-particle interactions limits the velocity throughout the cell. Steady-state conditions are reached within approximately 10 seconds [See Fig. 5.2]. The steady-state kinematic profiles of the granular mixtures are similar to those in monosized system measured in the physical and computational experiments (e.g., Refs. [81], [82], [151], [153]). The solids fractions of mixtures $\overline{f}$ is roughly uniform though near the walls there is some variation, most noticeably in the form of a periodic oscillation. The variation is primarily associated with some ordering of particles adjacent to the walls giving rise to oscillations in $\overline{f}$, though $\overline{f}$ decreases slightly near the wall as well [Fig. 6.1(b)]. The vertical velocity profile $\overline{w}$ resembles that of a plug flow, and the shear rate $\dot{\gamma} = d\overline{w}/dy$ is largest near the sidewalls [Fig. 6.1(c) and (d)]. Both the granular temperature $\overline{T}$ [Fig. 6.1(e)] and the kinetic stress $\sigma^k_{yy} = \overline{\rho}\overline{v'v'}$ [Fig. 6.1(f)] are highest where $\dot{\gamma}$ is the greatest adjacent to the walls [compare Figs. 6.1(d),(e), and (f)].

Figures 6.2(a) and (b) show snapshots of the simulation at $t = 0$ s and $t = 1000$ s. While the particles start out initially well-mixed, they exhibit a clear segregation pattern within minutes. For these high solids fraction conditions, the large particles accumulate close to the side walls where the shear rate and granular temperature are highest, and small particles segregate toward the center of chute, the region of lower shear rate and granular temperature. The particles in the center of the chute remains somewhat mixed over the period of time examined; the progress of segregation in this region is likely hindered due to the slow creep-like behavior of particles relative to their neighbors at the low shear rates in the center.

Quantitative measures of this segregation are plotted in Figs. 6.2(c) and (d). Figure 6.2(c) contains the profiles of species solids fraction $\overline{f}_i$. Here, the segregation is apparent in the high concentration of large particles close to side walls and of small particles near the center of the chute. Figure 6.2(d) contains the profiles of the horizontal segregation fluxes that give rise to this segregation pattern. Large particles exhibit a negative flux in left half of cell and a positive flux in right half of the cell that indicate the movement of the large particles away from the center. Small particles exhibit fluxes that indicate

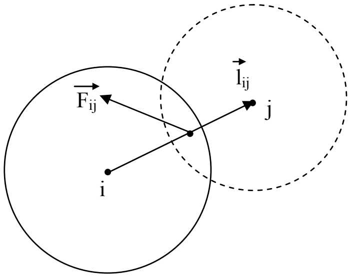

Figure 6.3: A sketch illustrating parameters needed to calculate contact stresses associated with contact between particles i and j. $\vec{l}_{ij}$ is the vector running from the center of particle i to the center of particle j. $\vec{F}_{ij}$ is the force exerted on particle i by particle j.

a movement of particles toward the center. In other words, the segregation patterns apparent in Figs. 6.2(b) and (c) are directly associated with these horizontal segregation fluxes rather than in other cases where there is advection rotates the segregation pattern relative to the direction of the segregation flux (e.g., Ref. [126]).

To compute the local contact stress at each position y, each interparticle contact K in a bin of width δy centered at y is considered. Then, the stresses associated with each interparticle contact in each region are summed, as in Refs. [47, 165]. Specifically, at each time step the local contact stress is calculated as:

$$\vec{\sigma}^c(y) = \frac{\sum_{K=1}^{N_c(y)} \vec{F}_{ij_K} \otimes \vec{l}_{ij_K}}{V_{bin}} \tag{6.23}$$

In Equation (6.23), $\vec{F}_{ij_K}$ is the force of particle j on particle i associated with the Kth contact in the bin of width δy centered at y; $\vec{l}_{ij_K}$ is the vector from the center of particle i to the center of particle j [Fig. 6.3]. $V_{bin} = \delta yLD$ is the volume of the region over which the calculation was performed.

The component of interest of the contact stress tensor is calculated according to $\sigma^c_{yy} = \Sigma_{K=1}^{N_c(y)} F_{ij_K,y} \otimes l_{ij_K,y}/V_{bin}$. The component of interest of the kinetic stress tensor is calculated according to $\sigma^k_{yy} = \rho\overline{v'v'}$ (Equation (3.18b)). When σ^c_{yy} and σ^k_{yy} are compared to the other potential contributors to the stress tensor $\frac{\partial}{\partial x^i_k}(\overline{u}^i_j\overline{\rho'^i u'^i_k})$, $\frac{\partial}{\partial x_k}(\overline{u}^i_k\overline{\rho'^i u'^i_j})$, and $\frac{\partial}{\partial x_k}(\overline{\rho'^i u'^i_k u'^i_j})$ in Fig. 6.4, it is clear that the neglected components are several orders of magnitude below σ^c_{yy} and σ^k_{yy}. Therefore, it is considered to be reasonable that related

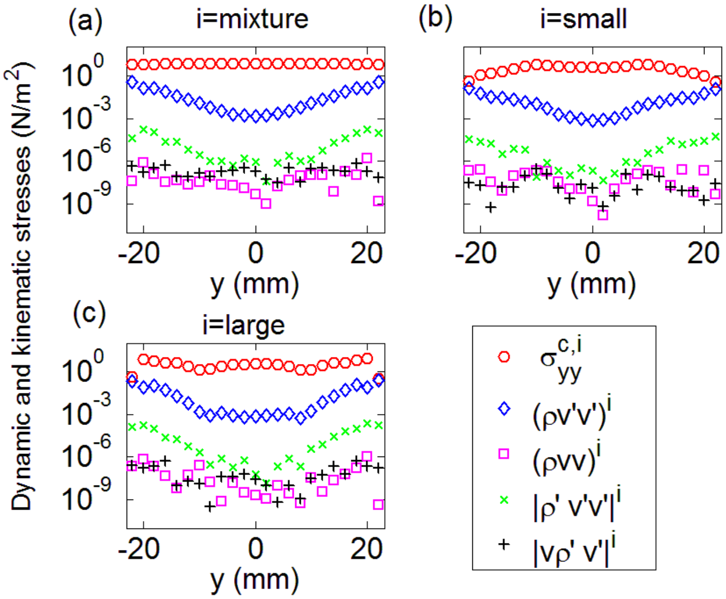

Figure 6.4: Profiles of five different dynamic and kinematic stresses in the Reynolds average equation of momentum in y direction for (a) mixtures, (b) 2mm particles, (c) 3mm particles.

terms for the theory developed in Section 6.1 are neglected.

In Figs. 6.5 (a) and (b), the profiles of $\sigma_{yy}^k(y)$ and $\sigma_{yy}^c(y)$ averaged over the second 50 s interval in the simulation are plotted after the mixture kinematics are essentially at steady state, but the segregation dynamics are still active..

The profile of $\sigma_{yy}^k(y)$ peaks near the rough walls and dips in the middle. As shown, it is well-fit by an exponential function $\sigma_{yy}^k(y) = A\exp(B|y|)$ whose fitting parameters A and B are given in the caption of Fig. 6.5. As one would expect from Equation (6.6), $\sigma_{yy}^c(y)$ follows the opposite trend: it is highest in the middle and dips near the walls, though it is significantly noisier than $\sigma_{yy}^c(y)$. It is believed that the noise is associated with the layering of the particles near the sidewalls. The plot of $\sigma_{yy}^c(y)$ is superposed with a line representing $C - (A\exp(B|y|))$ where C is the value of $\sigma_{yy}^c(y)$ in the center of the cell and A and B are the fitting parameters for $\sigma_{yy}^k(y) = A\exp(B|y|)$ given in the caption of Fig. 6.5. Considering the noise in this plot, reasonable agreement is reached. Currently a method to relate the variations in f with those in $\sigma_{yy}^c(y)$ is investigated as

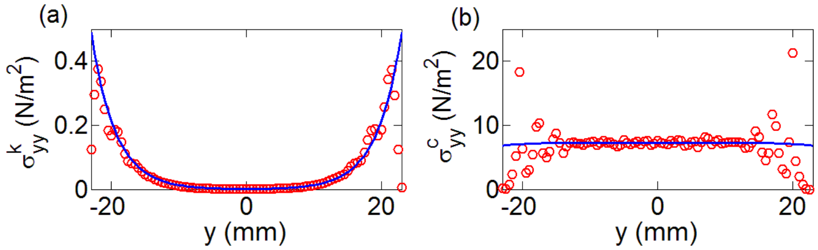

Figure 6.5: (a) Kinetic stress profile and (b) Contact stress profile for $\langle f \rangle = 0.60$ for $t = 50 - 100$ s. The circles denote data from the simulations with spatial intervals 0.5 mm in y direction. The lines denote fits based on the kinetic stress profile. For (a), the line denotes $\sigma^k_{yy}(y) = A\exp(|By|)$ based on a linearized least squares fit, where $A = 8.21 \times 10^{-4}$ N/m^2 and $B = 0.28$ mm^{-1}. For (b), the line denotes $\sigma^c_{yy}(y)_{exp} = C - A\exp(|By|)$ based on the fit for (a) and the average of the contact stress in the central region of the system, where $C = 7.29$ N/m^2.

will be discussed in Section 6.3. Nevertheless, for the theory developed in this thesis it is considered to be evidence that the data supports the theoretical prediction from Equation (6.6).

The calculation of partial kinetic stresses is pretty straightforward. Since the kinetic stresses in each bin is a linear summation of kinetic energy of velocity fluctuations of each particle, Equation (3.18) can be used directly by considering each species separately. However, it is more complicated to calculate partial contact stresses for each species, since a contact may involve two particles with different species. Therefore, three types of contacts separately in calculating the species contact stresses are considered. (1) Contacts between two small particles only contribute to the contact stress of the small particles, and the Kth such contact is denoted as $\vec{\sigma}^{c,ss}_K$. (2) Contacts between two large particles only contribute to the contact stresses of the large particles, and the Kth such contact is denoted as $\vec{\sigma}^{c,ll}_K$. (3) Contacts between one small particle and one large particles contribute to the contact stress of each type of particle; the Kth such contact is denoted as $\vec{\sigma}^{c,sl}_K$. While there are many ways one could divide each instance of $\vec{\sigma}^{c,sl}_K$ between the particles in question, it is divided equally between the two in this research because both the magnitude of the interparticle forces acting on each of the two particles in contact and the contact area between the two particles are equal.

Upon that, the partial contact stresses for small and large particles are calculated

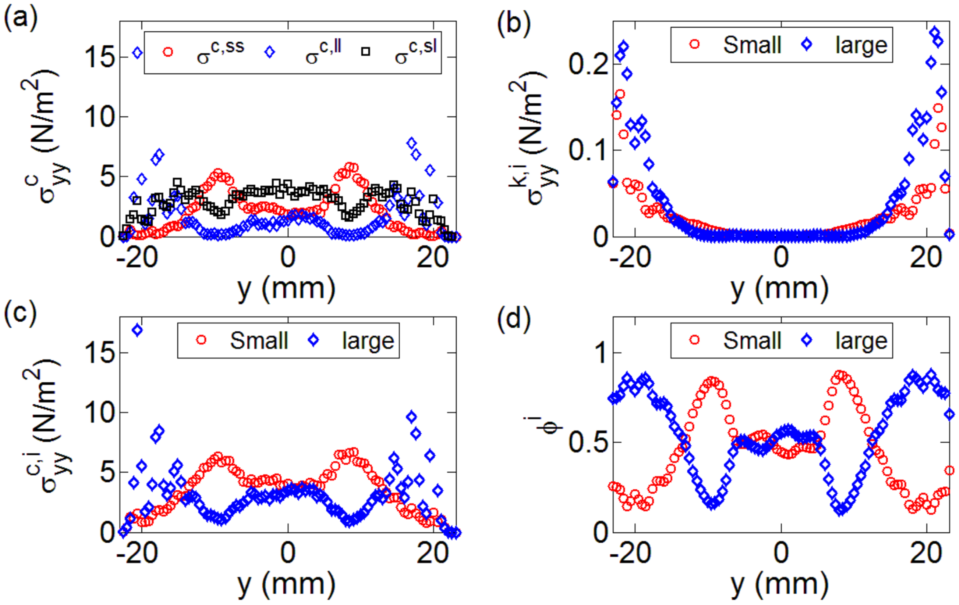

Figure 6.6: (a) Profiles of components of normal contact stresses in y direction between small-small $\sigma^{c,ss}$, small-large $\sigma^{c,sl}$ and large-large $\sigma^{c,ll}$ particles (b) Profiles of kinetic stresses $\sigma^{k,i}_{yy}$ for small and large particles in y direction. (c) Profiles of contact stresses $\sigma^{c,i}_{yy}$ for small and large particles in y direction. (d) Profiles of concentration ϕ^i for small and large particles in y direction. All data is averaged at $t = 50 - 100$s with spatial intervals of 0.5 mm.

as:

$$\vec{\sigma}^{c,s}(y) = \sum\nolimits_{K=1}^{N_c(y)} \vec{\sigma}_K^{c,ss} + \vec{\sigma}_K^{c,sl}/2 \tag{6.24}$$

and

$$\vec{\sigma}^{c,l}(y) = \sum\nolimits_{K=1}^{N_c(y)} \vec{\sigma}_K^{c,ll} + \vec{\sigma}_K^{c,sl}/2 \tag{6.25}$$

respectively, where $\sigma_K^{c,ij}$ is the Kth contact between particles of type i and j in the vertical bin centered at y.

In Fig. 6.6, the partial stresses at same time interval are plotted as those in Fig. 6.5. Fig. 6.6 (a) shows profiles of three types of contact stresses in y direction, which will be used to calculate partial contact stresses. Figs. 6.6 (b) and (c) show the partial kinetic and contact normal stresses in y direction. When comparing these two profiles with the

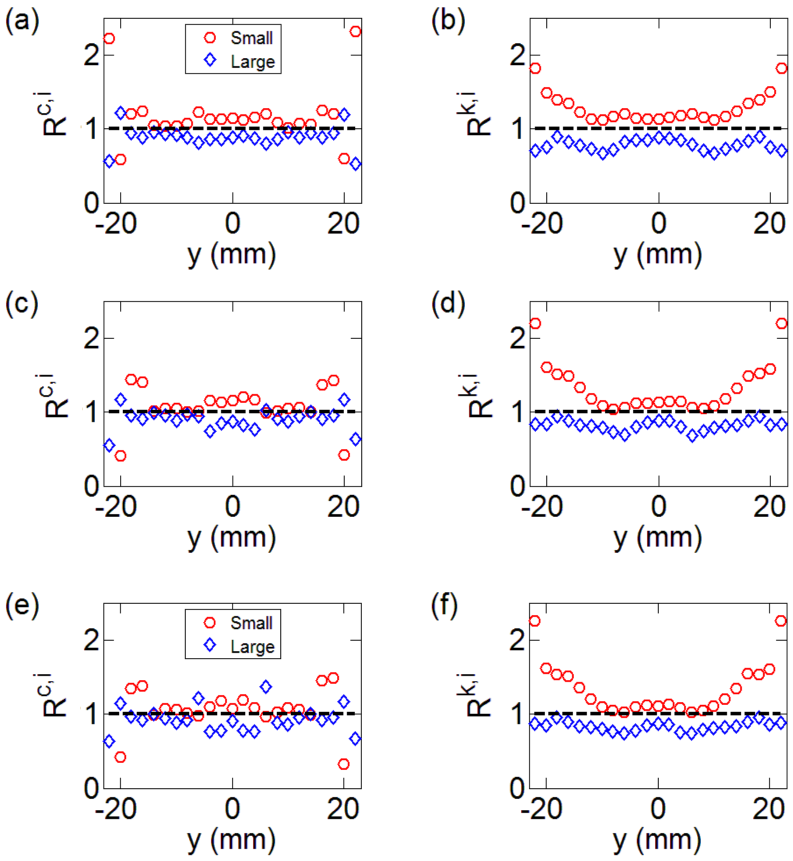

Figure 6.7: Profiles of coefficients $R^{c,i}$ and $R^{k,i}$ in y direction for 2 and 3 mm particles averaged at three different time intervals (a) and (b) t = 0-50 s; (c) and (d) t = 450-500 s; (e) and (f) t = 950-1000 s.

profiles of species' concentration in Figs. 6.6 (d), it is apparent that the normal contact stresses are strongly dependent on the local species concentrations.

Now, based on the partial normal kinetic and contact stresses, how the contact and kinetic stresses partition for different sized particles is investigated, that is the $R^{c,i}$ and $R^{k,i}$ defined as $\sigma^{c,i}_{yy}/(\phi^i\sigma^c_{yy})$ and $\sigma^{k,i}_{yy}/(\phi^i\sigma^k_{yy})$. The results are plotted in Fig. 6.7. $R^{c,i}$ and $R^{k,i}$ calculated from three different time intervals indicate that for both kinetic and contact normal stresses, the small particles always carry more normal stresses than large particles except for contact normal stresses close to boundaries where there may be significant error associated with the oscillations in f near the boundary as discussed above. It is expected that small particles will carry more kinetic normal stresses, since as shown in Hill and Zhang [84], in dense regime small particles always have larger granular temperature than large particles, which in turn means small particles will carry more kinetic stress by the definition. However, it is noted that the partition of contact stress is contradictory to the assumption in [92, 93]. In these references, Gray and colleagues assume ψ^i/ϕ^i is greater than 1 for large particles and smaller than 1 for small particles. This means for unit volume the large particles support more pressure or normal stresses than small particles do. It is this difference of pressure supported by two species that subsequently drives large particles to segregate to free surface and small particles to sink to the bed [92, 93]. However, in the shear-induced system without gravity effect, the situations seem totally different. This discrepancy may be due to different nature of shear-induced and gravity-induced segregation, an issue which could be studied in the future work.

To validate the theory in section 6.1, whether the theoretical prediction Equation (6.16) can predict the correct segregation trends compared to simulation results needs to be investigated. In Figs. 6.8(a) and (b), the profiles of $R^{c,s} - R^{k,s}$ and $R^{c,l} - R^{k,l}$ in y direction at different simulation time are shown respectively. It is clear that $R^{c,s} - R^{k,s}$ is always negative and $R^{c,l} - R^{k,l}$ is always positive except for the creeping region in the middle and regions close to the boundaries. Near the boundary there may be significant error associated with the oscillations in $\overline{f}$ as discussed above and in the creeping region $R^{c,l} - R^{k,l}$ and $R^{c,s} - R^{k,s} \approx 0$. Therefore, combining the fact that the gradients of kinetic normal stress shown in Fig. 6.5 (a) is negative in the left half the cell and positive in the right half of the cell, one can obtain the following segregation trends based on the prediction of Equation (6.16): Large particles have a negative segregation fluxes in the left half of the cell and positive segregation fluxes in the right half of the cell, while the small particles have an opposite trends. These indicate that large particles will segregate to the side walls and small particles will segregate toward the middle of the cell, which match the observations (See Fig. 6.2) in the simulations very well.

These results provide a positive first-order indication that the physical mechanisms that emerge from the theoretical development are reasonable. However, to obtain a quantitative prediction of the segregation process, a few additional details are required. One is a manner in which the difference between the stress partition coefficients $\psi^{c,i} - \psi^{k,i}$

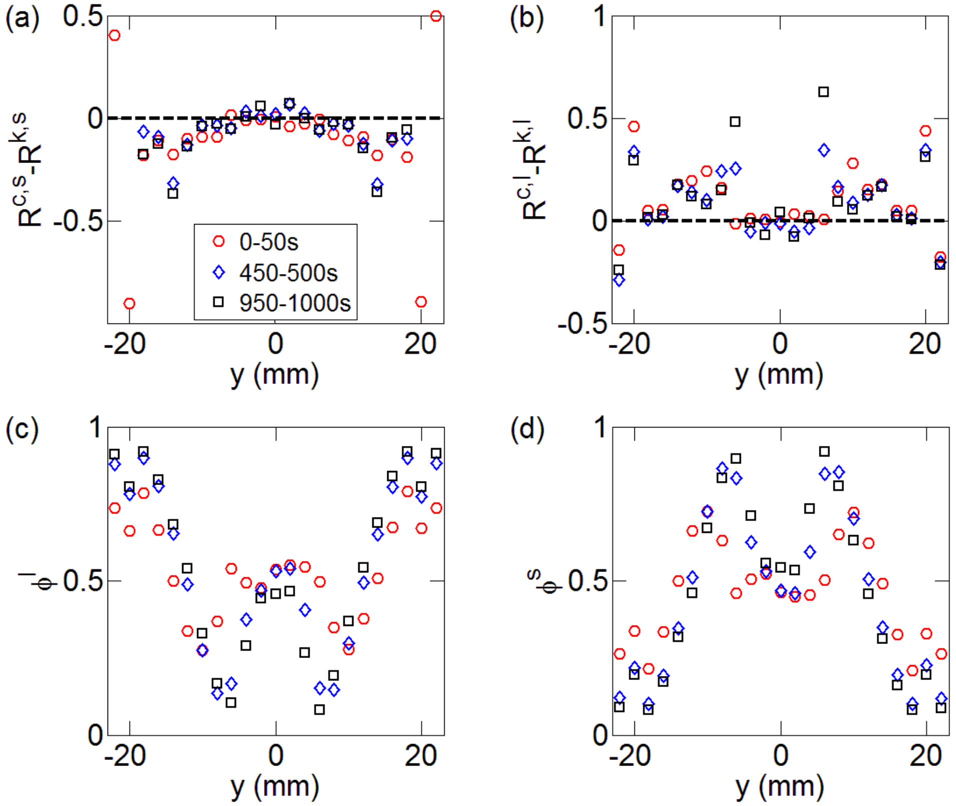

Figure 6.8: (a) $R^{c,s} - R^{k,s}$ vs. y and (b) $R^{c,l} - R^{k,l}$ vs. y at three different time intervals indicated in the figure. (c) and (d) the profiles of concentration of large and small particles in y direction respectively at the three different time intervals.

is related to certain flow properties such as species concentration or velocity gradients. Another is to determine a physical basis for the drag and diffusion coefficients c_D and d.

For their model, Gray and Thornton [92] proposed the following relationship for their analogous $\psi^{p,i} - \phi^i$ that fulfilled minimal requirements of mass and stress conservation: $\psi^{p,l} - \phi^l = \phi^l \phi^s$, and $\psi^{p,s} - \phi^s = -\phi^l \phi^s$. Then, in collaboration with Ancey [166] they determined empirical values for c_D and d based on experimental data. A similar relationship for $R^{c,i} - R^{k,i}$ is tentatively proposed to explore the predictive capabilities of this structure in the future plan section of the final chapter.

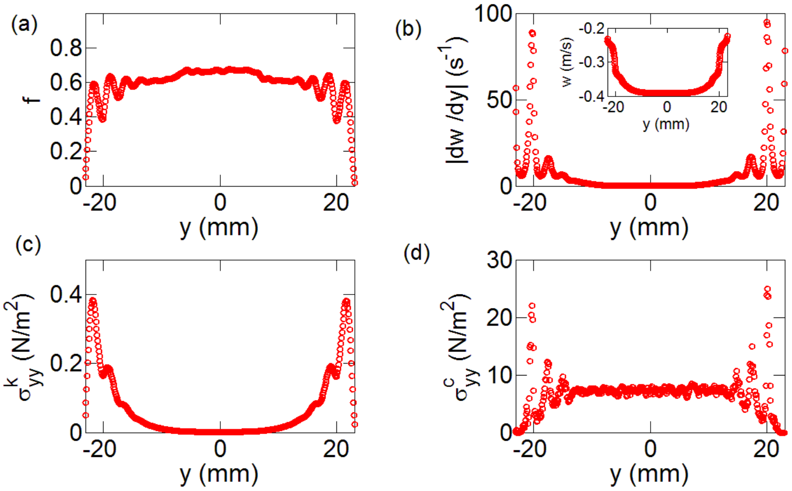

Figure 6.9: Profiles of kinetic and dynamic quantities in y direction for mixtures averaged at t =50-100 s for system solids fraction $\langle f \rangle$=0.6 with spatial intervals of 0.1 mm (a) Average solids fraction of the mixture f, (b) Absolute value of shear rate $|dw/dy|$, inset: Average streamwise velocity w , (c) kinetic normal stress of the mixture in y direction and (d) contact normal stresses of the mixture in y direction.

6.3 Effects of Granularity

Now the effects of the granularity of the system are briefly considered, particularly the layering that occurs next the walls.

To investigate this, first some of the profiles of the kinematics and the stresses are plotted in Fig. 6.9. These are comparable to some of the plots in Fig. 6.1 and 6.5, though calculated at a much higher resolution (i.e., smaller bin size Δy). There is significant evidence for the existence of layered structures adjacent to the wall, where from the plots, one almost imagines vertically aligned columns of beads sliding relative to one another. Similar phenomena has been previously reported for free surface sheared flows in drums (e.g., [126]) and is evidently significant for $f(y)$, dw/dy as well as the contact and kinetic stresses. The wavelength of the fluctuations is approximately 3 mm, the average diameter of the large particles. Since the manner in which the contact stress is calculated focuses the computed stress associated with each interparticle contact entirely at the point of contact, when particles are densely arranged in chains such as is indicated

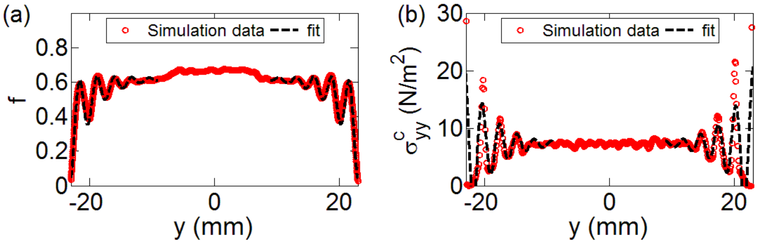

Figure 6.10: Data and fits for (a) $f(y)$ and (b) $\sigma^c_{yy}(y)$ illustrating the apparent anti-correlation between the oscillations of solids fraction and oscillations of contact normal stresses in the regions adjacent to the walls. The dotted lines are fitting curves capturing the average trends and oscillations for $f(y)$ and $\sigma^c_{yy}(y)$ as described in the text. (a) The dotted line represents $f(y) = f_{exp}+f_{osc}$. $f_{exp} = f_{max}+f_o\exp(-\tilde{y}/y_e)$ captures the apparent exponential decay in $f(y)$ adjacent to the wall; $f_{osc} = A\exp(-\tilde{y}/y_o)\sin(2\pi\tilde{y}/\lambda+\varphi)$ captures the oscillations in f whose amplitude decays exponentially away from the wall. (f_{max}, f_o, y_e) = (0.62, -0.31, 3.2 mm). $(A, y_o, \lambda, \varphi)$ = (0.27, 4 mm, 2.8 mm, -1.6). (b) The dotted line represents $\sigma^c_{yy}(y) = \sigma^c_{yy,exp} + \sigma^c_{yy,osc}$. As in Fig. 6.5, $\sigma^c_{yy,exp} = \sigma^c_{yy,max} - \sigma_{yy,o}\exp(|y/y_\sigma|)$, capturing the exponential decay in $\sigma^c_{yy}(y)$ adjacent to the walls. The details of the fitting parameters $(\sigma^c_{yy,max}, \sigma_{yy,o}, y_\sigma)$ are given in the caption of Fig. 6.5. $\sigma^c_{yy,osc} = -5f_{osc}$. $\tilde{y}$ =23 mm-$|y|$.

in Fig. 6.9(a), σ^c will be high where f is low, and low where f is high.

To obtain a measure of the fluctuations in f for comparison with fluctuations in σ^c, two sets of fits for $f(y)$ are performed. The first represents the overall apparent exponential decay in $f(y)$ adjacent to the wall $f_{exp} = f_{max} - f_o\exp(-\tilde{y}/y_e)$; the second represents the oscillations in f whose amplitude decays exponentially away from the wall $f_{osc} = A\exp(-\tilde{\mathrm{y}}/\mathrm{y_o})\sin(2\pi\tilde{\mathrm{y}}/\lambda+\varphi)$. The parameters are given in the caption of Fig. 6.10. In Fig. 6.10(a) the result from the fit ($f_{exp} + f_{osc}$ vs. y) is plotted on top of the simulation data showing the form of the fit represents the data fairly well. Then the form of the fit from the kinetic stress that is used for the contact stress in Fig. 6.5: $\sigma^c_{yy}(y)_{exp} = 7.29-(8.21\times10^{-4}\exp(|0.28y|)$ is considered. The oscillations are somewhat larger in $\sigma^c_{yy}(y)$ than for f - by trial and error it is found the oscillations in $\sigma^c_{yy}(y)$ to be approximately five times that in f. To compare the understanding that oscillations in f correspond to oscillations in $\sigma^c_{yy}(y)$, in Fig. 6.10(b) $\sigma^c_{yy}(y)_{exp} + 5f_{osc}$ is plotted on top of the simulation data for $\sigma^c_{yy}(y)$ and once again reasonable agreement is found.

To conclude, the oscillations in σ^c_{yy} is associated with oscillations in $f(y)$. This is an effect not captured in the continuum approach and its role in segregation is yet to be determined.

Chapter 7

Conclusion and future work

In this thesis, the effects of a gradient of shear rate and its associated granular temperature or solids fraction gradients on segregation of dense granular mixtures have been studied experimentally, computationally and theoretically. In Section 7.1, the major conclusions of this thesis are summarized. In Section 7.2, some possible future research directions based on current research will be proposed.

7.1 Conclusion

Experiments in a split-bottom cell isolated possible segregation driving factors, such as gravity, gradients of shear rate, and gradients of porosity, for segregation in dense flow. From these, the following results are obtained:

(1) For dense granular mixtures of particles differing only in *size*, the effect of gravity on segregation is strong near the boundaries, where a vertical gradient of shear rate or a gradient of solids fraction exists. The gravity-driven segregation in the split-bottom cell has similar trends to those in the flow of a rotating drum [84][95][100] or down an inclined plane [91][92]. Large particles segregate to free surface and small particles sink to the bottom. However, the gravity-driven segregation is limited to the boundaries, and is not observed in the bulk flow, where the solids fraction is very high and a vertical gradient of shear rate is lacking. This means without a gradient of shear rate and/or enough porosity, the effect of gravity on segregation in dense flow is greatly limited.

(2) In contrast, in the bulk, a slow developing horizontal size segregation pattern is

observed, coinciding with the horizontal gradients of shear rate. In this case, the small particles segregate to the regions of smaller radii and large particles segregate to the regions of larger radii in the shear zone and the boundary of these two regions is located in the center of shear zone, where the shear rate and granular temperature are highest.

(3) For dense granular mixtures of particles differing *material density* only, gravity drives vertical segregation throughout the shear zone in the bulk, suppressing any possible horizontal segregation related to horizontal gradients of shear rate. The trends of gravity-driven density segregation are also same as those in other geometries [84][94]: The denser particles sink to the bottom and the less dense particles rise to the surface.

(4) When horizontal shear rate gradients at the free surface are isolated from other effects, in this sparse and energetic regime, the large particles segregate to the regions of lower shear rate. Analogous experiments are performed for mixtures differing in material density only, and the less dense particles segregate to the regions of lower shear rate.

To understand the correlation between the horizontal segregation pattern and gradients of shear rate in the bulk of the split-bottom cell for particles differing only in size, DEM simulations are used to investigate the segregation evolution and measure segregation kinematics in the bulk. Two different types of split-bottom cells, a circular split-bottom cell and a parallel split-bottom cell, are simulated to identify curvature effects. The following results are obtained from the computational simulations:

(1) In the circular split-bottom cell, similar segregation patterns are observed to those in the experiments: Close to the bottom and the free surface, vertical segregation occurs, where large particles rise to the free surface and small particles sink to the bottom. In the bulk, a horizonal segregation pattern is observed: The small particles accumulate to the regions of smaller radii and the large particles accumulate to the region of large radii in the shear zone. The boundary between these two regions is located at the center of shear zone, which is also the region of maximum shear rate. However, rather than horizontal segregation fluxes, a persistent toroidal convection roll with the vertical gravity-driven segregation flux together is found to cause the horizontal segregation.

(2) In the parallel split-bottom cell, vertical segregation patterns occur that are similar to those in the circular cell: The large particles segregate to the free surface and

small particles sink to the bottom in both cells. In the bulk, horizontal segregation patterns are observed, but, different from that in circular cell, the large particles segregate to the center of shear zone, the region of the higher shear rate and small particles segregate out of shear zone, the region of lower shear rate. There is no persistent convection roll existing. Instead, a subtle horizontal segregation flux is observed in the bulk, which drives large particles to the center of shear zone and small particles to the edges of shear zone.

(3) Kinetic theory is employed to predict segregation velocity between the two segregating species in the horizontal direction of the parallel split-bottom cell. Kinetic theory actually predicts opposite segregation trends and overestimates segregation fluxes compared with simulation results in the bulk.

DEM simulations are also performed in a vertical chute cell to study dynamics of shear-induced size segregation in the macro- and micro- scales. The system solids fractions are also varied to investigate transitions of shear-induced segregation from sparse flow to dense flow. The results are summarized as the following:

(1) While the local solids fraction and other kinematics are non-uniform, the global solids fraction controls the segregation behavior in the vertical chute cell. For systems of low system-averaged solids fraction, large particles accumulate the regions of low shear rate, low granular temperature and high local solids fraction, in quantitative agreement with predictions using kinetic theory. However, for systems of high system solids fraction, the opposite occurs and the attempt to match kinetic theory with the simulation results fails dramatically.

(2) The direction of the segregation of large particles relative to small particles transitions at a moderate value of system-averaged solids fraction, and the transition is likely governed by the global structure of the system: As system-averaged solids fraction increases, the system structure changes from one dominated by binary collisions to one dominated by one cluster that can involve $> 60\%$ of the particles and span the system.

(3) The global solids fraction at which the transition occurs does not appear to be unique. The point of transition changes as the system evolves to steady state. It is expect to depend on details such as particle size distribution [37] as the maximum packing fraction changes. It is also expect to change with the coefficient of restitution and other details involving interparticle contacts.

A theoretical framework was developed to model the shear-induced size segregation. In this model, Reynolds averaging of the conservation of momentum equations produces two stresses: (1) contact stresses associated with contact forces between particles and (2) kinetic stresses due to velocity fluctuations of particles. Two assumptions are used in this model. The first assumption is that two different types of stresses partition differently between different species in the mixtures of particles differing in size only. The second assumption is that the inter-species' forces by using a similar formulation to that of the percolation of fluids through porous solids. By considering the conservation equations of momentum, a formulation for segregation fluxes of each species may be developed and the model may be validated using simulation results from the vertical chute cell. The following results are obtained:

(1) The equation developed for segregation fluxes for each species shows that the shear-induced segregation is driven by a gradient in kinetic stresses and the segregation trends are determined by the difference of partitioning coefficient between contact normal stresses and kinetic normal stresses of each species.

(2) The simulation results from the vertical chute cell validate the theoretical prediction for shear-induced segregation in dense flow: The large particles segregate to a region of higher granular temperature and shear rate and small particles segregate to the region of lower granular temperature and shear rate.

7.2 Future work

In the computational study of the vertical chute flow, it is identified that the gradient of shear rate and its associated gradients in granular temperature can induce size segregation of dense granular mixtures and also found the transition of shear-induced segregation from the sparse flow to the dense flow could be governed by the global structure of the system. However, the following aspects need to be pursued:

(1) As mentioned in Chapter 5, the solids fraction for this transition is likely not unique, but instead may depend on particle size distribution, the system sizes, or some details involving interparticle contacts such as restitution coefficients, particle stiffness. Therefore, a systematic study of these effects on the transition points is needed.

(2) In the split-bottom cell, the gravity-driven density segregation is very strong

so that any possible shear-induced density segregation is suppressed. However, in the vertical chute cell, as the gravity effect on the segregation is minimized, the shear effect on the density segregation could be investigated.

(3) While the computational results are satisfying, physical experiments should be performed to investigate the applicability of these results for physical system.

A theoretical framework has also been developed to model the shear-induced segregation of particles differing only in size. The future research directions based on current work could be the following:

(1) The model in this thesis for shear-induced segregation could be combined with the models for gravity-driven segregation in Refs. [92, 93]. In this way, a more complete model can be developed for predicting segregation with considering all different driving mechanisms in dense flow.

(2) The kinetic and contact stresses profiles cannot be obtained from the first principles at this time. A constitutive law for granular mixtures is needed, a goal being pursued by some research groups such as those described in [37].

(3) A physical basis is needed for the form of the partition coefficients from the model as they relate to flow properties such as species concentration or velocity gradients. This would allow for the governing equations to be solved numerically to obtain the segregation evolution.

To illustrate how this might be done, a linear relation that $(R^{c,i} - R^{k,i}) = B\phi^j$ is tentatively proposed based on Fig. 7.1, where B is a constant (B=0 at the creeping region). Then, combining Equation (6.16) and Equation (6.7) in the y direction results in the following equation:

$$\frac{\partial \phi^i}{\partial t} + q\frac{\partial}{\partial y}[\phi^i(1-\phi^i)\frac{1}{\rho}\frac{\partial \sigma^k_{yy}}{\partial y}] - D\frac{\partial^2 \phi^i}{\partial y^2} = 0 \tag{7.1}$$

Here $q = \frac{B}{c_D}$ and $D = \frac{d}{c_D}$. The tempo-spatial profiles of concentration of species i could be obtained by solving Equation (7.1) if given the local bulk density ρ [see Fig. 6.1(b)], and the local gradients of kinetic normal stresses $\frac{\partial \sigma^k_{yy}}{\partial y}$ [see Fig. 6.5 (a)], with proper boundary and initial conditions:

$$\phi^s = \phi^l = 0.5 \quad \text{at } t\text{=0 for all values of } y \tag{7.2}$$

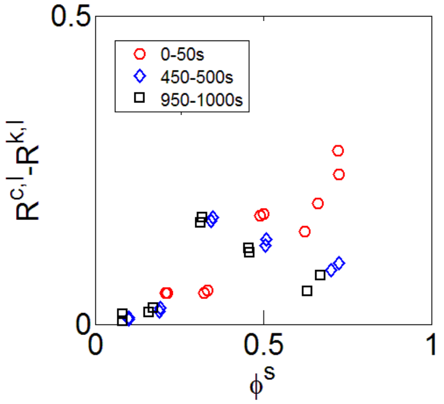

Figure 7.1: $R^{c,l} - R^{k,l}$ vs. ϕ_s respectively, excluding data in the middle region (8 mm$\geq y \geq$ -8 mm) and regions close to boundaries ($y \leq$ -20 mm and $y \geq$ 20 mm).

$$q(1-\phi^l)\phi^l \frac{\partial \sigma^k_{yy}}{\rho \partial y} = D\frac{\partial \phi^l}{\partial y} \quad \text{at two side walls} \tag{7.3}$$

Equation (7.2) is the homogenous initial condition. Equation (7.3) implies a no-flux boundary condition. Central difference scheme is used for spatial derivatives and the fourth order Runge-Kutta method is used for time integration to numerically solve Equation (7.1).

Figures. 7.2(a) and (b) show tempo-spatial profiles of concentration of large particles from simulation data and theoretical predictions up to 1000 s respectively. Based on trial and error $q = 2.5 \times 10^{-3}$ s and $D = 0.05$ mm^2/s are chosen. Qualitatively, a number of details are reproduced. In both the simulation results and theoretical predictions, the large particles segregate to the side walls, while small particles segregate toward the center. In the middle slow creeping region, where the gradients of normal kinetic stresses is very small, the segregation process is much slower than other regions. All of these indicate a good qualitative agreement between theoretical predictions and simulation results, though they do not reach a perfect quantitative agreement.

The reason that a good agreement between theoretical prediction and simulations quantitatively is not reached may be due to the following aspects, which need to be considered further in this model:

(4) There are several fitting parameters such as diffusivity D and drag coefficient c_D

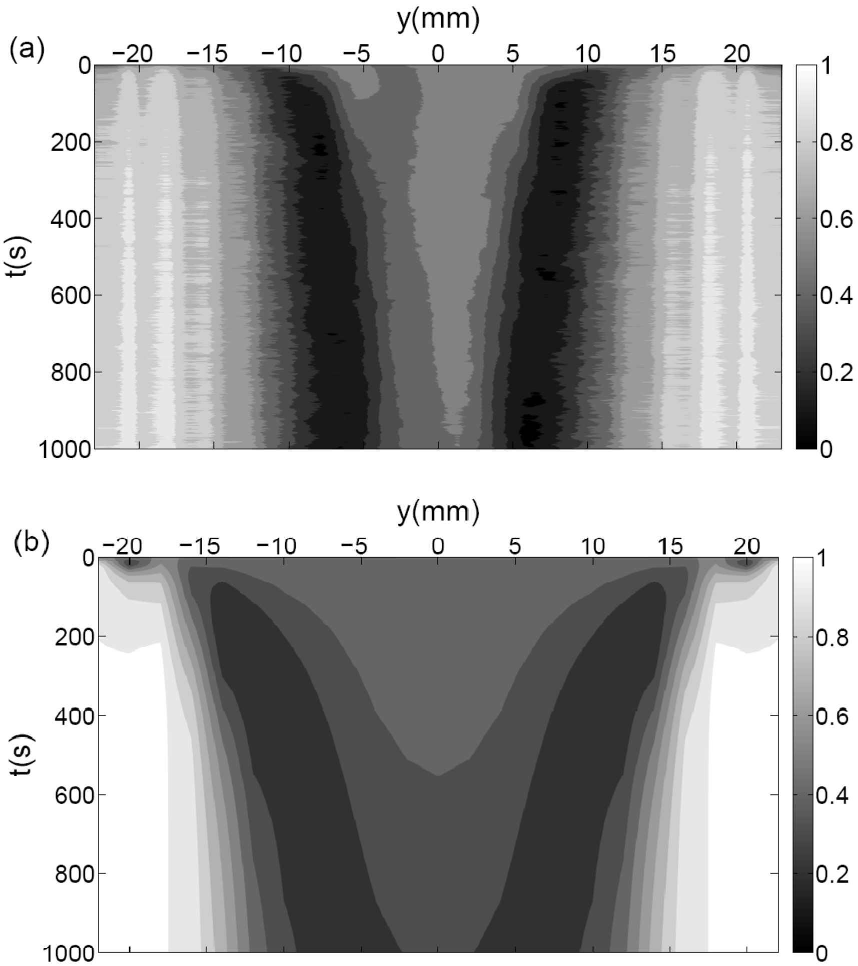

Figure 7.2: tempo-spatial profiles of concentration of large particles (a) simulation results; (b) theoretical predictions. The legend indicates the shade of gray that corresponds to particular fraction of large particles. For example, $\phi^l = 1$ for white pixels and $\phi^l = 0$ for black pixels.

in the model. Several works have shown these coefficients may depend on the local shear rate [167][166]. Theoretical or at least the empirical formulations need to be developed.

To conclude, despite the importance of the segregation of granular materials in the nature and industries, the understanding and modeling of the segregation is still far from perfect, especially for the densely sheared granular mixtures. In this thesis, experiments, simulations, and theory are used to develop a better understanding of certain segregation mechanisms in dense sheared flow. The gradient of shear rate and its associated gradient in granular temperature have been identified as drivers for the segregation in the densely sheared flow with substantial evidence in this thesis. The results have important implications for the development of segregation in dense sheared systems, and, because the rheology of sheared granular mixtures depends on the local particle size distribution, the results bear on rheological models of mixtures.

Current physical or mathematical models to describe the segregation of the densely shear flow such as Refs. [91][92] [93], do not consider the shear effects on the segregation trends in dense flow. Based on the computational investigation and theoretical modeling of the shear-induced segregation in this thesis with those models for gravity-driven segregation in [91][92][93], a more rigorous and comprehensive model can be developed with considering all these driving mechanisms. The better model can be used to predict the segregation behaviors in nature or industry and, further, may even be used to limit the segregation by manipulating flow kinematics.

References

[1] P. G. de Gennes. Granular matter: a tentative view. *Rev. Mod. Phys.*, 71:S374–382, 1999.

[2] B. J. Ennis, J. Green, and R. Davies. The legacy of neglect in the us. *Chem. Eng. Prog.*, 90:32–43, 1994.

[3] T. M. Knowlton, G. E. Klinzing, W.-C. Yang, and J. W. Carson. The importance of storage, transfer, and collection. *Chem. Eng. Prog.*, 90:44–54, 1994.

[4] H. M. Jaeger, S. R. Nagel, and R. P. Behringer. Granular solids, liquids, and gases. *Rev. Mod. Phys.*, 68:1259–1273, 1996.

[5] R. M. Nedderman. *Statics and kinematics of granular materials.* Cambridge University Press, Cambridge, 1992.

[6] A. Schofield and P. Wroth. *Critical state soil mechanics.* McGraw-Hill, London, 1968.

[7] J.-N. Roux and G. Combe. Quasistatic rheology and the origins of strain. *C. R. Physique*, 3:131–140, 2002.

[8] G.W. Baxter, R.P. Behringer, T. Fagert, and G. A. Johnson. Pattern formation in flowing sand. *Phys. Rev. Lett.*, 62:2825–2828, 1989.

[9] Peng. G. and H. J. Herrmann. Density waves of granular flow in a pipe using lattice-gas automata. *Phys. Rev. E*, 49:R1796–1799, 1994.

[10] E. D. Liss, S. L. Conway, and B. J. Glasser. Density waves in gravity-driven granular flow through a channel. *Phys. Fluids*, 14:3309–3326, 2002.

[11] I. Goldhirsch and G. Zanetti. Clustering instability in dissipative gases. *Phys. Rev. Lett.*, 70:1619–1622, 1993.

[12] R. A. Bagnold. Experiments on a gravity-free dispersion of large solid particles in a newtonian fluid under shear. *Proc. R. Soc. London Ser. A*, 225:49–63, 1954.

[13] S. B. Savage and D. J. Jeffrey. The stress tensor in a granular flow at high shear rates. *J. Fluid Mech.*, 110:255–272, 1981.

[14] N. L. Ackermann and H. Shen. Stresses in rapidly sheared fluid-solid mixtures. *J. Eng. Mech. Diu. ASCE*, 108:95–113, 1982.

[15] J. T. Jenkins and S. B. Savage. A theory for the rapid flow of identical, smooth, nearly elastic particles. *J. Fluid Mech.*, 130:187–202, 1983.

[16] C. K. K. Lun, S. B . Savage, D. J. Jeffrey, and N. Chepurniy. Kinetic theories for granular flow: inelastic particles in couette flow and slightly inelastic particles in a general flowfie1d. *J. Fluid Mech.*, 140:223–256, 1984.

[17] C. S. Campbell. Rapid granular flows. *Annu. Rev. Fluid Mech.*, 22:57–92, 1990.

[18] J. T. Jenkins and F. Mancini. Balance laws and constitutive relations for plane flows of a dense, binary mixture of smooth, nearly elastic, circular disks. *J. Appl. Mech.*, 54:27–34, 1987.

[19] J. T. Jenkins and F. Mancini. Kinetic theory for binary mixtures of smooth, nearly elastic spheres. *Phys. Fluids A*, 1:2050–2057, 1989.

[20] P. Jop, Y. Forterre, and O. Pouliquen. A constitutive law for dense granular flows. *Nature*, 441:727–730, 2006.

[21] L. S. Mohan, K. K. Rao, and P. R. Nott. A frictional cosserat model for the slow shearing of granular materials. *J. Fluid Mech.*, 457:377–409, 2002.

[22] K. Kamrin and M. Z. Bazant. Stochastic flow rule for granular materials. *Phys. Rev. E*, 75:041301,1–28, 2007.

[23] I. S. Aranson and L. S. Tsimring. Continuum theory of partially fluidized granular flows. *Phys. Rev. E*, 65:061303,1–20, 2002.

[24] M. Y. Louge. Model for dense granular flows down bumpy inclines. *Phys. Rev. E*, 67:061303 ,1–11, 2003.

[25] L. Bocquet, W. Losert, D. Schalk, T.C. Lubensky, and J. P. Gollub. Granular shear flow dynamics and forces: Experiment and continuum theory. *Phys. Rev. E*, 65:011307 ,1–19, 2001.

[26] S. B. Savage. Analyses of slow high-concentration flows of granular materials. *J. Fluid Mech.*, 377:1–26, 1998.

[27] D. Ertas and T. C. Halsey. Granular gravitational collapse and chute flow. *Eurphys. Lett.*, 60:931–937, 2002.

[28] J. T. Jenkins. Dense shearing flows of inelastic disks. *Phys. Fluids*, 18:103307, 1–9, 2006.

[29] J. T. Jenkins and D. Berzi. Dense inclined flows of inelastic spheres: tests of an extension of kinetic theory. *Granular Matt.*, 12:151–158, 2010.

[30] F. da Cruz, S. Emam, M. Prochnow, J. N. Roux, and F. Chevoir. Rheophysics of dense granular materials: discrete simulation of plane shear flows. *Phys. Rev. E*, 72:021309, 1–17, 2005.

[31] S. B. Savage and K. Hutter. The motion of a finite mass of granular material down a rough incline. *J. Fluid Mech.*, 199:177–215, 1989.

[32] C. Ancey, P. Coussot, and P. Evesque. A theoretical framework for granular suspensions in a steady simple shear flow. *J. Rheol.*, 43:1673–1699, 1999.

[33] T. Hatano. Power-law friction in closely packed granular materials. *Phys. Rev. E*, 75:R060301, 1–4, 2007.

[34] P. Jop, Y. Forterre, and O. Pouliquen. Crucial role of sidewalls in granular surface flows: consequences for the rheology. *J. Fluid Mech.*, 541:167–192, 2005.

[35] O. Pouliquen, C. Cassar, P. Jop, Y. Forterre, and M. Nicolas. Flow of dense granular material: towards simple constitutive laws. *J. Stat. Mech.*, 2006:P07020,1–14, 2006.

[36] P.G. Rognon, J. N. Roux, M. Naaim, and F. Chevoir. Dense flows of bidisperse assemblies of disks down an inclined plane. *Phys. Fluid*, 19:058101, 1– 4, 2005.

[37] B. Yohannes and K. M. Hill. Rheology of dense granular mixtures: Particle-size distributions, boundary conditions, and collisional time scales. *Phys. Rev. E.*, 82:061301,1–9, 2010.

[38] B. Yohannes and K. M. Hill. Preliminary investigations on the rheology and boundary stresses associated with granular mixtures. In J. Goddard, J. T. Jenkins, and P. Giovine, editors, *IUTAM-ISIMM Symposium on Mathematical Modeling and Physical Instances of Granular Flows*, volume 1227, pages 379–387. 2010.

[39] P. Jop. Hydrodynamic modeling of granular flows in a modified couette cell. *Phys. Rev. E*, 77:032301,1–4, 2008.

[40] Y. Forterre and O. Pouliquen. Flows of dense granular media. *Annu. Rev. Fluid Mech.*, 40:1–24, 2008.

[41] A. Daerr and S. Douady. Sensitivity of granular surface flows to preparation. *Europhys. Lett.*, 47:324–330, 1999.

[42] L. Quartier, B. Andreotti, S. Douady, and A. Daerr. Dynamics of a grains on a sandpile model. *Phys. Rev. E*, 62:8299–8307, 2000.

[43] O. Pouliquen and Y. Forterre. Friction law for dense granular flows: application to the motion of a mass down a rough inclined plane. *J. Fluid Mech.*, 453:133–151, 2002.

[44] F. da Cruz, F. Chevoir, J. N. Roux, and I. Iordanoff. Macroscopic friction of dry granular materials. *Tribol. Ser.*, 43:53–61, 2003.

[45] G. Lois, A. Lemaitre, and J. M. Carlson. Emergence of multi-contact interactions in contact dynamics simulations of granular shear flows. *Europhys. Lett.*, 76:318–324, 2006.

[46] M. Babic, H. H. Shen, and H. T. Shen. The stress tensor in granular shear flows of uniform, deformable disks at high solids concentrations. *J. Fluid Mech.*, 219:81–118, 1990.

[47] C. S. Campbell. Granular shear flows at the elastic limit. *J. Fluid Mech.*, 465:261–291, 2002.

[48] S. Ji and H. H. Shen. Internal parameters and regime map for soft polydispersed granular materials. *J. Rheol.*, 52:87–103, 2008.

[49] J. M. N. T. Gray and B. P. Kokelaar. Large particle segregation, transport and accumulation in granular free-surface flows. *J. Fluid Mech.*, 652:105–137, 2010.

[50] J. D. Stock and W. E. Dietrich. Erosion of steepland valleys by debris flows. *Geol. Soc. Am. Bull.*, 118:1125–1148, 2006.

[51] L. Hsu, W. E. Dietrich, and L. S. Sklar. Experimental study of bedrock erosion by granular flows. *J. Geophysical Research*, 113:F02001, 2008.

[52] T. Shinbrot and F. Muzzio. Nonequilibrium patterns in granular mixing and segregation. *Physics Today*, 53:25–30, 2000.

[53] A. Rosato, K. J. Strandburg, F. Prinz, and R. H. Swendsen. Why the brazil nuts are on top: Size segregation of particulate matter by shaking. *Phys. Rev. Lett.*, 58:1038–1040, 1987.

[54] L. Vanel, A. D. Rosato, and R. N. Dave. Rise-time regimes of a large sphere in vibrated bulk solids. *Phys. Rev. Lett.*, 78:1255–1258, 1997.

[55] A. Kudrolli. Size separation in vibrated granular matter. *Rep. Prog. Phys.*, 67:209–247, 2004.

[56] M. Faraday. On a peculiar class of acoustical figures; and on certain forms assumed by groups of particles upon vibrating elastic surfaces. *Phil. Trans. R. Soc. Lond.*, 121:299–340, 1831.

[57] J. B. Knight, H. M. Jaeger, and S. R. Nagel. Vibration-induced size separation in granular media: The convection connection. *Phys. Rev. Lett.*, 70:3728–3731, 1993.

[58] A. D. Rosato, D. L. Blackmore, N. Zhang, and Y. Lan. A perspective on vibration-induced size segregation of granular materials. *Chemical Engineering Science*, 57:265–275, 2002.

[59] T. Shinbrot and F. J. Muzzio. Reverse buoyancy in shaken granular beds. *Phys. Rev. Lett.*, 81:4365–4368, 1998.

[60] Y. N. Molinari, G. C. Chay, and J. C. R. Suarez. Inertia in the brazil nut problem. *Phys. Rev. E*, 68:041301, 1–6, 2003.

[61] D. C. Hong, P. V. Quinn, and S. Luding. Reverse brazil nut problem: Competition between percolation and condensation. *Phys. Rev. Lett.*, 86:3423–3426, 2001.

[62] L. Huilin, D. Gidaspow, and E. Manger. Kinetic theory of fluidized binary granular mixtures. *Phys. Rev. E*, 64:061301,1–8, 2001.

[63] M. F. Rahaman, J. Naser, and P. J. Witt. An unequal temperature kinetic theory: description of granular flow with multiple particle classes. *Powder Tech.*, 138:82–92, 2003.

[64] B. O. Arnarson and J. T. Willits. Thermal diffusion in binary mixtures of smooth, nearly elastic spheres with and without gravity. *Phys. Fluids*, 10:1324–1328, 1998.

[65] J. T. Willits and B. O. Arnarson. Kinetic theory of a binary mixture of nearly elastic disks. *Phys. Fluids*, 11:3116–3122, 1999.

[66] S. S. Hsiau and M. L. Hunt. Granular thermal diffusion in flows of binary-sized mixtures. *Acta Mechanica*, 114:121–137, 1996.

[67] J. E. Galvin, S. R. Dahl, and C. M. Hrenya. On the role of nonequipartition in the dynamics of rapidly flowing, granular mixtures. *J. Fluid Mech.*, 528:207–232, 2005.

[68] D. V. Khakhar, J. J. McCarthy, and J. M. Ottino. Mixing and segregation of granular materials in chute flows. *Chaos*, 9:594–610, 1999.

[69] J. J. Brey, M. J. R. Montero, and F. Moreno. Energy partition and segregation for an intruder in a vibrated granular system under gravity. *Phys. Rev. Lett.*, 95:098001,1–4, 2005.

[70] D. Serero, I. Goldhirsch, S. H. Noskowicz, and M. L. Tan. Hydrodynamics of granular gases and granular gas mixtures. *J. Fluid Mech.*, 554:237–258, 2006.

[71] M. P. Ciamarra, M. D. De Vizia, A. Fierro, M. Tarzia, A. Coniglio, and M. Nicodemi. Granular species segregation under vertical tapping: Effects of size, density, friction, and shaking amplitude. *Phys. Rev. Lett.*, 96:058001,1–4, 2006.

[72] S. Ulrich, M. Schröter, and H. L. Swinney. Influence of friction on granular segregation. *Phys. Rev. E*, 76:058001,1–3, 2007.

[73] M. E. Möbius, B. E. Lauderdale, S. R. Nagel, and H. M. Jaeger. Size separation of granular particles. *Nature*, 414:270, 2001.

[74] X. Yan, Q. Shi, M. Hou, K. Lu, and C. K. Chan. Effects of air on the segregation of particles in a shaken granular bed. *Phys. Rev. Lett.*, 91:014302,1–4, 2003.

[75] M. E. Möbius, X. Cheng, G. S. Karczmar, S. R. Nagel, and H. M. Jaeger. Intruders in the dust: Air-driven granular size separation. *Phys. Rev. Lett.*, 93:198001,1–4, 2004.

[76] N. Burtally, P. J. King, and M. R. Swift. Spontaneous air-driven separation in vertically vibrated fine granular mixtures. *Science*, 295:1877–1879, 2002.

[77] M. P. Ciamarra, A. Coniglio, and M. Nicodemi. Shear-induced segregation of a granular mixture under horizontal oscillation. *J. Phys.: Condens. Matter*, 17:S2549–S2556, 2005.

[78] M. P. Ciamarra, A. Coniglio, and M. Nicodemi. Dynamically induced effective interaction in periodically driven granular mixtures. *Phys. Rev. Lett.*, 97:038001,1–4, 2006.

[79] J. T. Jenkins and D. K. Yoon. Segregation in binary mixtures under gravity. *Phys. Rev. Lett.*, 88:194301,1–4, 2002.

[80] L. Trujillo, M. Alam, and H. J. Herrmann. Segregation in a fluidized binary granular mixture: Competition between buoyancy and geometric forces. *Europhys. Lett.*, 64:190–196, 2003.

[81] K. S. Ananda, S. Moka, and P. R. Nott. Kinematics and statistics of dense, slow granular flow through vertical channels. *J. Fluid Mech.*, 610:69–97, 2008.

[82] V. Chikkadi and M. Alam. Slip velocity and stresses in granular poiseuille flow via event-driven simulation. *Phys. Rev. E.*, 80:021303, 1– 16, 2009.

[83] K. M. Hill, A. Caprihan, and J. Kakalios. Bulk segregation in rotated granular material measured by magnetic resonance imaging. *Phys. Rev. Lett.*, 78:50–53, 1997.

[84] K. M. Hill and J. Zhang. Kinematics of densely flowing granular mixtures. *Phys. Rev. E*, 77:061303,1–7, 2008.

[85] D. J. Stephens and J. Bridgwater. The mixing and segregation of cohesionless particulate materials, part ii. microscopic mechanisms for particles differing in size. *Powder Technol.*, 21:29–44, 1978.

[86] L. B. H. May, L. A. Golick, K. C. Phillips, M. Shearer, and K. E. Daniels. Shear-driven size segregation of granular materials: Modeling and experiment. *Phys. Rev. E*, 81:051301,1–8, 2010.

[87] S. L. Conway, X. Liu, and B. J. Glasser. Instability-induced clustering and segregation in high-shear couette flows of model granular materials. *Chemical Engineering Science*, 61:6404–6423, 2006.

[88] J. Liu and A. D. Rosato. General features of granular couette flow and intruder dynamics. *J. Phys.: Condens. Matter*, 17:S2609–S2622, 2005.

[89] H. Xu, M. Louge, and A. Reeves. Solutions of the kinetic theory for bounded collisional granular flows. *Continuum Mech. Thermodyn.*, 15:321–349, 2003.

[90] J. M. Montanero, V. Garzo, M. Alam, and S. Luding. Rheology of two- and three-dimensional granular mixtures under uniform shear flow: Enskog kinetic theory versus molecular dynamics simulations. *Granular Matt.*, 8:103–115, 2006.

[91] S. B. Savage and C. K. K. Lun. Particle size segregation in inclined chute flow of dry cohesionless granular solids. *J. Fluid Mech.*, 189:311–335, 1988.

[92] J. M. N. T. Gray and A. R. Thornton. A theory for particle size segregation in shallow granular free-surface flows. *Proc. R. Soc. A*, 461:1447–1473, 2005.

[93] J. M. N. T. Gray and V. A. Chugunov. Particle-size segregation and diffusive remixing in shallow granular avalanches. *J. Fluid Mech.*, 569:365–398, 2006.

[94] D. V. Khakhar, J. J. McCarthy, and J. M. Ottino. Radial segregation of granular mixtures in rotating cylinders. *Phys. Fluids*, 9:3600–3614, 1997.

[95] J.M. Ottino and D.V. Khakhar. Mixing and segregation of granular materials. *Annu. Rev. Fluid Mech.*, 32:55–91, 2000.

[96] J. Bidgwater, M. H. Cooke, and A. M. Scott. Interparticle percolation: equipment development and mean percolation velocities. *Trans. Inst. Chem. Engrs.*, 56:157–167, 1978.

[97] J. A. Drahun and J. Bridgwater. The mechanisms of free surface segregation. *Powder Technol.*, 36:39–53, 1983.

[98] M. Alonso, M. Satoh, and K. Miyanami. Optimum combination of size ratio, density ratio and concentration to minimize free surface segregation. *Powder Technol.*, 68:145–152, 1991.

[99] G. Metcalfe and M. Shattuck. Pattern formation during mixing and segregation of flowing granular materials. *Physica A*, 233:709–717, 1996.

[100] N. Jain, J. M. Ottino, and R. M. Lueptow. Combined size and density segregation and mixing in noncircular tumbler. *Phys. Rev. E*, 71:051301, 1–10, 2005.

[101] N. Jain, J. M. Ottino, and R. M. Lueptow. Regimes of segregation and mixing in combined size and density granular system: an experimental study. *Granular Matt.*, 7:69–81, 2005.

[102] J. Zhang. *Kinematics and kinetics of granular mixture: Experimental and numerical studies.* PhD thesis, University of Illinois at Urbana-Champaign, 2009.

[103] K. M. Hill, Y. Fan, J. Zhang, C. Van Niekerk, E. Zastrow, S. C. Hagness, and J. T. Bernhard. Granular segregation studies for the development of a radar-based three-dimensional sensing system. *Granular Matt.*, 12:201–207, 2010.

[104] J. R. Abbott, N. Tetlow, A. L. Graham, S. A. Altobelli, E. Fukushima, L. A. Mondy, and T. S. Stephens. Experimental observations of particle migration in concentrated suspensions: Couette flow. *J. Rheol.*, 35:773–795, 1991.

[105] D. Leighton and A. Acrivos. Measurement of shear-induced self-diffusion in concentrated suspensions of spheres. *J. Fluid Mech.*, 177:109–131, 1987.

[106] D. Leighton and A. Acrivos. shear-induced migration of particles in concentrated suspensions. *J. Fluid Mech.*, 181:415–439, 1987.

[107] G. P. Krishnan, S. Beimfohr, and D. T. Leighton. Shear-induced radial segregation in bidisperse suspensions. *J. Fluid Mech.*, 321:371–393, 1996.

[108] A. Shauly, A. Wachs, and A. Nir. Shear-induced particle migration in a polydisperse concentrated suspension. *J. Rheol.*, 42:1329–1348, 1998.

[109] C. Barentin, E. Azanza, and B. Pouligny. Flow and segregation in sheared granular slurries. *Europhys. Lett.*, 66:139–145, 2004.

[110] W. S. Foo and J. Bridgwater. Particle migration. *Powder Technol.*, 36:271–273, 1983.

[111] F. Rietz and R. Stannarius. On the brink of jamming: Granular convection in densely filled containers. *Phys. Rev. Lett.*, 100:078002,1–4, 2008.

[112] I. Zuriguel, J. F. Boudet, and Y. Amarouchene. Role of fluctuation-induced interactions in the axial segregation of granular materials. *Phys. Rev. Lett.*, 95:258002,1–4, 2005.

[113] E. Fukushima. Nuclear magnetic resonance as a tool to study flow. *Annu. Rev. Fluid Mech.*, 31:95–123, 1999.

[114] M. Nakagawa, S. A. Altobelli, A. Caprihan, E. Fukushima, and E. K. Jeong. Noninvasive measurements of granular flows by magnetic resonance imaging. *Exp. Fluids*, 16:54–60, 1993.

[115] X. Cheng, J. B. Lechman, A. Fernandez-Barbero, G. S. Grest, H. M. Jaeger, G. S. Karczmar, M. E. Möbius, and S. R. Nagel. Three-dimensional shear in granular flow. *Phys. Rev. Lett.*, 96(3):038001,1–4, 2006.

[116] K. Sakaie, D. Fenistein, T. J. Carroll, M. van Hecke, and P. Umbanhowar. Mr imaging of reynolds dilatancy in the bulk of smooth granular flows. *Europhys. Lett.*, 84:38001,1–5, 2008.

[117] K. M. Hill, A. Caprihan, and J. Kakalios. Bulk segregation of granular media segregated in a rotating drum measured by magnetic resonance imaging. *Phys. Rev. Lett.*, 78:50–53, 1997.

[118] E. E. Ehrichs, H. M. Jaeger, G. S. Karczmar, James B. Knight, V. Yu, and S. R. Nagel. Granular convection observed by magnetic resonance imaging. *Science*, 267:1632–1634, 1995.

[119] C. J. Broadbent, J. Bridgwater, D. J. Parker, S. T. Keningley, and P. Knight. A phenomenological study of a batch mixer using a positron camera. *Powder Technol.*, 76:317–329, 1993.

[120] D.J. Parker, A. E. Dijkstra, T. W. Martin, and J. P. K. Seville. Positron emission particle tracking studies of spherical particle motion in rotating drums. *Chemical Engineering Science*, 52:2011–2022, 1997.

[121] D. M. Mueth, G. F. Debregeas, G. S. Karczmar, P. J. Eng, S. R. Nagel, and H. M. Jaeger. Signatures of granular microstructure in dense shear flows. *Nature*, 406:385–389, 2000.

[122] S. A. McDonald, L. C. R. Schneider, A. C. F. Cocks, and P. J. Withers. Particle movement during the deep penetration of a granular material studied by x-ray microtomography. *Scripta Materialia*, 54:191–196, 2006.

[123] M. Toiya, J. Hettinga, and W. Losert. 3d imaging of particle motion during penetrometer testing. *Granular Matt.*, 9:323–329, 2007.

[124] N. Jain, J. M. Ottino, and R. M. Lueptow. An experimental study of the flowing granular layer in a rotating tumbler. *Phys. Fluids*, 14:572–582, 2002.

[125] D. Bonamy, F. Daviaud, and L. Laurent. Experimental study of granular surface flows via a fast camera: A continuous description. *Phys. Fluids*, 15:1666–1674, 2002.

[126] K. M. Hill, G. Gioia, and V. V. Tota. Structure and kinematics in dense free-surface granular flow. *Phys. Rev. Lett.*, 91:064302,1–4, 2003.

[127] J. E. Maneval, K. M. Hill, B. E. Smith, A. Caprihan, and E. Fukushima. Effects of end wall friction in rotating cylinder granular flow experiments. *Granular Matt.*, 7:199–202, 2005.

[128] N. Taberlet, P. Richard, A. Valance, R. Delannay, W. Losert, J. M. Pasini, J. T. Jenkins, and R. Delannay. Super stable granular heap in thin channel. *Phys. Rev. Lett.*, 91:264301,1–4, 2003.

[129] D. Fenistein and M. van Hecke. Kinematics: Wide shear zones in granular bulk flow. *Nature (London)*, 425:256, 2003.

[130] D. Fenistein, J. W. van de Meent, and M. van Hecke. Universal and wide shear zone in granular bulk flow. *Phys. Rev. Lett.*, 92:094301,1–4, 2004.

[131] D. Fenistein, J. W. van de Meent, and M. van Hecke. Core precession and global modes in granular bulk flow. *Phys. Rev. Lett.*, 96:118001,1–4, 2006.

[132] T. Unger, J. Torok, J. Kertesz, and D. E. Wolf. Shear band formation in granular media as a variational problem. *Phys. Rev. Lett.*, 92:214301,1–4, 2004.

[133] T. Poschel and T. Schwager. *Computational granular dynamics: Models and algorithms.* Springer, Berlin, 2005.

[134] T. A. J. Duke, G. C. Barker, and A. Mehta. A monte carlo study of granular relaxation. *Europhys. Lett.*, 12:19–24, 1990.

[135] M. A. Hopkins and H. H. Shen. A monte carlo solution for rapidly shearing granular flows based on the kinetic theory of dense gases. *J . Fluid Mech.*, 244:477–491, 1992.

[136] S. Luding, H. J. Herrmann, and A. Blumen. Simulations of two-dimensional arrays of beads under external vibrations: Scaling behavior. *Phys. Rev. E.*, 50:3100–3108, 1994.

[137] M. Alam and S. Luding. Rheology of bidisperse granular mixtures via event-driven simulations. *J. Fluid Mech.*, 476:69–103, 2003.

[138] K. C. Vijayakumar and M. Alam. Velocity distribution and the effect of wall roughness in granular poiseuille flow. *Phys. Rev. E.*, 75:051306, 1– 5, 2007.

[139] J. Schafer, S. Dippel, and D. E. Wolf. Force schemes in simulations of granular materials. *J. Phys. I France*, 6:5–20, 1996.

[140] P. A. Cundall and O. D. L. Strack. A discrete numerical model for granular assemblies. *Geotechnique*, 29:47–65, 1979.

[141] O. R. Walton and R. L. Braun. Viscosity, granular-temperature, and stress calculations for shearing assemblies of inelastic, frictional disks. *J. Rheol.*, 30:949–980, 1986.

[142] J. A. C. Gallas, H. J. Herrmann, and S. Sokolowski. Convetion cell in vibrating granular media. *Phys. Rev. Lett.*, 69:1371–1374, 1992.

[143] Y. Tsuji, T. Tanaka, and T. Ishida. Lagrangian numerical simulation of plug flow of cohesionless particles in a horizontal pipe. *Powder Technol.*, 71:239 – 250, 1992.

[144] E. Falcon, C. Laroche, S. Fauve, and C. Coste. Behavior of one inelastic ball bouncing repeatedly off the ground. *Eur. Phys. J. B*, 3:45–57, 1998.

[145] S. Ji and H. H. Shen. Effect of contact force models on granular flow dynamics. *Journal of Engineering Mechanics*, 132:1252–1259, 2006.

[146] M. Weber. *Simulation of cohesive particle flows in granular and gas-solid systems.* PhD thesis, University of Colorado, 2004.

[147] M. Majid and P. Walzel. Convection and segregation in vertically vibrated granular beds. *Powder Technol.*, 192:311–317, 2009.

[148] A. Ries, D. E. Wolf, and T. Unger. Shear zones in granular media: Three-dimensional contact dynamics simulation. *Phys. Rev. E*, 76:051301,1–5, 2007.

[149] R. D. Wildman and D. J. Parker. Coexistence of two granular temperatures in binary vibrofluidized beds. *Phys. Rev. Lett.*, 88:064301,1–4, 2002.

[150] K. Feitosa and N. Menon. Breakdown of energy equipartition in a 2d binary vibrated granular gas. *Phys. Rev. Lett.*, 88:198301,1–4, 2002.

[151] O. Pouliquen and N. Renaut. Onset of granular flows on an inclined rough surface: dilatancy effects. *J. Phys. II*, 6:923–935, 1996.

[152] C. Denniston and H. Li. Dynamics and stress in gravity-driven granular flow. *Phys. Rev. E*, 59:3289–3292, 1999.

[153] GDR MiDi. On dense granular flows. *Eur. Phys. J. E*, 14:341–365, 2004.

[154] S. Sarkar and D. V. Khakhar. Experimental evidence for a description of granular segregation in terms of the effective temperature. *Europhys. Lett.*, 83:54004,1–6, 2008.

[155] Y. Fan and K. M. Hill. Shear-driven segregation of dense granular mixtures in a split-bottom cell. *Phys. Rev. E*, 81:041303,1–12, 2010.

[156] G. K. Batchelor. *An Introduction to Fluid Dynamics*. Cambridge University Press, Cambridge, UK, 2000.

[157] H. Schlichting. *Boundary-Layer Theory*. McGraw-Hill, New York, 1979.

[158] J. Zhang and K. M. Hill. *Under reivew*, 2011.

[159] L. W. Morland. A simple constitutive theory for a fluid-saturated porous solid. *J. Geophysical Research*, 77:890–900, 1972.

[160] L. W. Morland. A theory of slow fluid flow through a porous thermoelastic matrix. *Geophys. J. R. Astron. Soc.*, 55:393–410, 1978.

[161] L. W. Morland. Flow of viscous fluids through a porous deformable matrix. *Surv. Geophys.*, 13:209–268, 1992.

[162] R. D. Mindlin and H. Deresiewicz. Elastic spheres in contact under varying oblique forces . *J. Appl. Mech. Trans. ASME*, 20:327–344, 1953.

[163] H. Hertz. Süber die berührung fester elastischer körper (on the contact of rigid elastic solids). In Jones and Schott, editors, *Miscellaneous Papers*, page 156. Macmillan, London, 1896.

[164] H. Hertz. Ueber die berührung fester elastischer körper (on contact between elastic bodies). In *Gesammelte Werke (Collected Works)*, volume 1. Leipzig, Germany, 1895.

[165] E. Kuhl, G. A. D'Addetta, H. J. Herrmann, and E. Ramm. A comparison of discrete granular material models with continuous microplane formulations. *Granular Matt.*, 2:113–121, 2000.

[166] S. Wiederseiner, N. Andreini, G. Epely-Chauvin, G. Moser, M. Monnereau, J. M. N. T. Gray, and C. Ancey. Experimental investigation into segregating granular flows down chutes. *Phys. Fluids*, 23:013301, 1–10, 2011.

[167] V. V. R. Natarajan, M. L. Hunt, and E. D. Taylor. Local measurements of velocity fluctuations and diffusion coefficients for a granular material flow. *J . Fluid Mech.*, 304:1–25, 1995.